Fundamental Studies of Positron Scattering from Atoms and Molecules

Roisín Alindia Boadle

July 2018

A thesis submitted for the degree of Doctor of Philosophy of
The Australian National University

Australian
National
University

To my parents, Vicki and Mike, who showed me the value of learning and to all my teachers, who helped me along this path.

Declaration

This thesis is an account of research undertaken at The Research School of Physics and Engineering, The Australian National University, Canberra, Australia.

Except where acknowledged in the customary manner, the material presented in this thesis is, to the best of my knowledge, original and has not been submitted in whole or part for a degree in any university.

Roisín Alindia Boadle

July 19th, 2018

Acknowledgments

This thesis would not have been possible without the support of many people, I would like to sincerely thank each of them for their contributions.

First, I would like to thank my supervisor, James Sullivan, for not only his academic guidance and the time dedicated to providing feedback on my thesis, but also for his patience throughout the process from start to finish. I would like to thank Stephen Buckman for always having words of encouragement and Bob McEachran for all his theoretical calculations and willingness to share his extensive knowledge. I would like to acknowledge Dennis Mueller for giving me the chance to work on the reaction microscope and for helping me to puzzle out the analysis.

I have worked with many wonderful people in the lab and I thank everyone for their support, teaching and friendship. I'd especially like to thank Emma Anderson for being my lab buddy at the beginning, Joshua Machacek for showing me the ropes on the beamline and Tamara Babij who helped me collect data and made the lab a fun place to be. I'd like to acknowledge Simon Armitage who guided me through the establishment of the reaction microscope and always gave me the chance to try out ideas, without his mentoring I would not have been able to complete this part of my research. In addition, I would like to thank Steve Battisson and Ross Tranter, who were always on hand for technical support and taught me lots of useful things.

Furthermore, I'd like to thank all the friends who made my PhD time enjoyable, who listened to my woes and supported me along the way, and who helped make Canberra a home. In particular, I'd like to thank Jenny, Kate and Romana for always being available for a cup of tea and a chat, and Jo, who has heard almost all the ups and downs of this PhD.

Finally, I'd like to thank my family for all their support throughout my education and for never complaining that I moved to the other side of the world to do this PhD.

Abstract

This thesis presents measurements of low-energy positron scattering from Argon and C_{60}. Absolute elastic differential cross sections are presented for positron scattering from Argon in the energy range 2 to 50 eV, as well as absolute total elastic and inelastic cross sections up to 20 eV. These results are compared with theoretical calculations using the convergent close-coupling (CCC) and relativistic optical potential (ROP) methods and it was found that generally the measurements were in closer agreement with the CCC method than the ROP method across the energy range, although the ROP method was an excellent description of the total inelastic cross section in this energy range.

Argon was also the focus of the first results from the newly developed positron reaction microscope. Experimental techniques were developed to produce measurements of the kinematics of positron-induced single ionisation of Argon. Single ionisation events were detected in coincidence and their momenta reconstructed using data analysis methods detailed in this thesis. Although further work is required to provide total differential cross sections, the initial data presented in this thesis is in alignment with expectations based upon available theory and experiment and provides a promising starting point for future studies using the positron reaction microscope.

Finally, a search was conducted for resonant features in the total scattering and Positronium formation cross sections of C_{60}. Motivated by the predictions of Gianturco and Lucchese (1999), which indicated experimentally-accessible resonances, the present data does not show any features. However, the current results in this thesis represent the first preliminary measurements of the total scattering and Positronium formation cross sections for C_{60} and follow the expected trend for positron-molecule scattering. Additional data to be collected in the future, would allow for confirmation of the presence, or lack thereof, of resonant features with a higher statistical confidence.

Contents

List of Figures

List of Tables

Chapter 1

Introduction

The existence of the positron was first proposed by Paul Dirac in a series of papers between 1928 and 1931, whilst developing a quantum theory of the electron. His equations resulted in two possible solutions: a positive energy solution which was easily attributed to the electron, and a negative energy solution which he proposed could indicate a particle with a positive charge (Dirac, 1928). Later, despite its mass being significantly higher than the electron, he suggested this particle was the proton, but corrected himself in 1931, postulating the existence of an unobserved particle, the anti-electron, or as it is referred to today, the positron (Dirac, 1931). His new particle was quickly confirmed experimentally by Carl Anderson through cosmic radiation studies in a cloud chamber (Anderson, 1933). Particle tracks with the same mass-to-charge ratio as the electron were captured, but they moved in the opposite direction, indicating a positively charged particle (see figure 1.0.1). This was the first experimental evidence of antimatter, however not the first time positrons had been observed. Although they had been unable to explain their results, working independently, both Dmitri Skobeltsyn, in Russia, and Chung-Yao Chao, at California Institute of Technology, had detected them (Mehra and Rechenberg, 2001). In the same year that Anderson published his work, the positron was captured in photographs by Blackett and Occhialini (Blackett and Occhialini, 1933). Nobel prizes in physics were awarded to Dirac in 1933 for the theoretical work and to Anderson in 1936 for the experimental confirmation.

The positron, in accordance with the CPT theorem, is a fermion with the same mass as the electron but with an equal and opposite charge (Charlton and Humberston, 2000, p.4). In a vacuum, the positron is a stable particle with

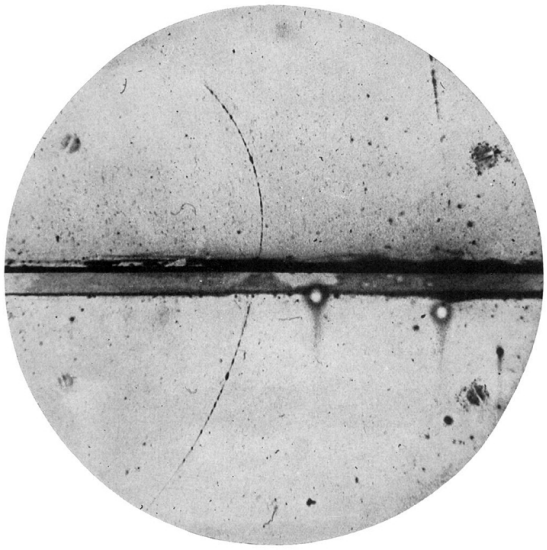

Figure 1.0.1: Image taken by Anderson (1933) showing the first known positron track. The cloud chamber, which sits in a magnetic field of 15 kG, is split in two by a 6 mm lead plate. The visible track shows a particle with the same mass-to-charge ratio as an electron, but with a positive charge, passing from bottom to top.

a lifetime $\geq 4.3 \times 10^{23}$ years, the experimental limit on the electron's lifetime (Aharonov et al., 1995). However, when a positron and electron collide they annihilate, converting their mass into energy.

Dirac's quantum theory implies that for every matter particle there is an antiparticle, many of which have been confirmed experimentally. One of the great unsolved mysteries surrounding antimatter is its apparent rarity in the observable Universe. During the Big Bang, matter and antimatter should have been created in equal amounts. The matter-antimatter asymmetry observed in the Universe implies that antimatter can be converted into matter, a mechanism known as baryogenesis which is not yet fully understood (for a review see Dine and Kusenko (2004)). In 2011, the first atoms of antihydrogen, where the proton is replaced with an antiproton and the electron with a positron, were produced and stored for more than 1000s at CERN (Andresen et al., 2011). According to the CPT theorem, the spectra of hydrogen and antihydrogen should be identical. This idea was tested for the first time in 2017 when laser-spectroscopic measurements of the 1S-2S transition were made for magnetically trapped antihydrogen particles. The frequency of the transition was found to be consistent with hydrogen atoms

in the same environment (Ahmadi et al., 2017). These results suggest that the behaviour of matter and antimatter are consistent with the CPT theorem.

Positrons have been exploited for various applications, for example, in medical imaging through Positron Emission Tomography (PET) and in materials science. In the latter case, there are a number of techniques that have been developed, which make use of positron-electron annihilation. When a positron annihilates with an electron the most likely outcome is two 511 keV gamma rays emitted 180° apart, with respect to the frame of reference of the positron-electron system to conserve momentum (see section 2.2.2). However, in the laboratory frame of reference, there can be a small deviation from 511 keV and 180° which can typically be ascribed to the momentum of the electron as the positron is considered to reach thermal temperatures prior to annihilation. These deviations were first observed by DeBenedetti et al. (1949), resulting in the development of Positron Annihilation Spectroscopy (PAS) techniques. Angular Correlation of Annihilation Radiation (ACAR) was an early technique that made use of these angular deviations. It was first applied in studies on the Fermi surfaces of metals, initially by Lang and Hien (1958) for single crystal cadmium, and then by Berko and Plaskett (1958) for single crystal aluminium and copper. However, with some exceptions (Manuel et al., 1995), the advent of improved detector technologies that allow measurement of gamma ray energies have made ACAR less popular. Doppler Broadening Spectroscopy (DBS), which measures the energy spectrum of annihilation gamma rays, makes use of the slight Doppler shift in the 511 keV energy and was first made experimentally accessible in work by Lynn et al. (1977). There are also techniques which investigate the ratio between 3-γ and 2-γ annihilation (3-γ annihilation spectroscopy, see Petkov et al. (2001)) and those that measure positronium time of flight (Ps-TOF, see Mondal et al. (1999)). Age-Momentum Correlation (AMOC) combines DBS with measurements of the positron lifetime in a material, whereas Positron Annihilation Lifetime Spectroscopy (PALS) uses just the lifetime of a positron in a material to investigate its structure. The variation in positron lifetimes within amorphous materials was first observed by Bell and Graham (1953), followed by an application of PALS techniques to lead and tin at superconducting temperatures by Stump and Talley (1954).

However, whilst the techniques above make use of the fundamental interactions between positrons, atoms and molecules, many of these interactions are still

not fully understood. Comprehending these interactions is a topic which continues to test theoretical modelling and can be probed through scattering studies, measuring cross sections which represent the probability of specific processes. A more complete model of positron-matter interactions may result not only in a deeper understanding of quantum mechanics, but also improvements in applications of positrons.

High-energy positrons are produced naturally in β^+ radioactive decays and through pair production from a photon with an energy of at least 1.022 MeV i.e. twice the electron/positron rest energy. Atomic and molecular physics experiments require low-energy (a few hundred eV) beams with well-defined energy spreads, and radioactive sources, such as Sodium-22, are arguably the most convenient option for this work. However, the positrons produced through radioactive decay have a very large energy spread, of the order MeV, rendering them unusable in their natural state.

A key development in the quest to develop more suitable positron beams was the discovery that fast positrons could be converted to slow positrons through moderation. Moderation was first observed by Cherry (1958) who found that positrons with an energy of less than 10 eV were produced after transmission through mica which had been coated in a thin conducting layer of chromium. However, the efficiency of the moderator (the conversion rate of fast to slow positrons) was low at around 10^{-8}. Building on this initial work, the first confirmed positron beam was produced by Costello et al. (1972b). Positrons were produced through pair production in an electron linear accelerator (LINAC) and several different moderators (aluminium, mica, CsBr), each with a 150-200 Å thick coating of gold, were trialled. These moderators produced slow positrons with energies of a few eV, which they proposed was due to a 'negative' work function. The first low-energy positron scattering measurements followed soon after, conducted by Canter et al. (1972), who used a gold surface coated in Magnesium Oxide as a moderator. Although the moderator efficiency was only 3×10^{-5}, it lead to further intense work on positron moderation resulting in the solid neon moderator with efficiencies around 10^{-2} (Mills and Gullikson, 1986), significantly higher than the observations of Cherry (1958). Thus, high intensity positron beams with well-defined energies were produced, opening up the field of experimental low-energy positron scattering research.

The first positron total scattering cross sections were measured in the seventies (Canter et al., 1972; Costello et al., 1972a). These early measurements tended to focus on the noble gases which are simpler targets for theory to model and easy to use in experiments, making them obvious initial targets. Following these early experiments, many more positron beamlines began to be built around the world. In the 1970s, these beamlines often used time-of-flight measurements to determine cross sections (for example, at University College London (Canter et al., 1972)) and in the eighties, the first fully electrostatic beamline was developed at Brandeis University (Canter et al., 1987). Some of these experiments were limited to the measurement of total scattering cross sections, but further development also led to the first measurements of elastic differential cross sections by Coleman and McNutt (1979) at The University of Texas at Arlington, USA and followed by Hyder et al. (1986) at Detroit University, USA. Ionisation cross sections were first measured by Fromme et al. (1986) at Bielefeld University, Germany. Studies of electronic excitation and positron-specific processes such as positronium formation (a e^+e^- temporary bound state) and annihilation as a function of energy followed. The introduction of the buffer gas trap (Murphy and Surko, 1992) greatly improved positron count rates and is currently in use on several experiments including those at the University of California, San Diego, where the technique was developed, and at the Australian National University. Buffer gas traps have also been used extensively in the antihydrogen experiments at CERN (Andresen et al., 2011).

These technological developments mean that more recent measurements of the scattering cross sections of simple targets such as hydrogen, with improved energy resolutions and statistical accuracy, provide a more rigorous test of theory. All of these experiments rely upon a gaseous target, limiting targets to those which are gases at room temperature (or liquids with a high vapour pressure at room temperature). However, the introduction of target ovens, where a solid target is heated to provide a sufficient vapour pressure, has opened doors for the study of biomolecules such as uracil (Surdutovich et al., 2008; Anderson et al., 2014) and metals (e.g. sodium and potassium in Kwan et al. (1991)). In the future, this could also include studying positron-atom (or positron-molecule) bound states, the majority of which are predicted for targets which are solid at room temperature (Mitroy et al., 2002).

Another step in improving our understanding of positron interactions with matter is the measurement of kinematically complete triply differential cross sections (TDCS). This entails the measurement, in coincidence, of the vector momenta of all particles after a collision and provides detailed information for the stringent testing of theoretical models. The following historical discussion focuses on electron impact ionisation of atoms, but it is worth noting that there has been much additional work done using similar techniques, including photon and ion projectiles and processes such as molecular fragmentation (for a full review see Ullrich et al. (2003)).

In order to illustrate the difficulty of the theoretical modelling of electron impact ionisation, it is interesting to note that it was only at the turn of this century that Rescigno et al. (1999) and Kadyrov and Bray (2002) managed to fully solve the most basic system (ionisation of atomic hydrogen). Many other systems have been modelled incompletely over the years, including atoms and complex molecules. It is therefore important that there is high quality experimental data to test these models and this has been provided in recent years through the development of the reaction microscope.

The study of electron impact ionisation in these kinematically complete studies has its roots in the early (e, 2e) experiments, first performed in the late sixties (Ehrhardt et al., 1969). These experiments detected the scattered and emitted electrons from a single ionisation event in coincidence and helped to illuminate the dynamics of the three body Coulomb problem. However, they were significantly limited due to the number of single-channel detectors they had and low count rates, meaning they could not be extended to study double ionisation or any more complicated interactions.

The current reaction microscopes, which grew out of Recoil Ion Momentum Spectroscopy (RIMS) and Cold Target Recoil Ion Momentum Spectroscopy (COLTRIMS), were developed by Moshammer et al. (1996). These experiments are designed to have up to 4π acceptance and a high momentum resolution. Coupled with their ability to detect all final particles (for example, electrons and recoil-ion for ionisation studies) in coincidence and their multi-hit detectors, this makes them a powerful tool for atomic and molecular physics. The first measurements of electron impact ionisation of helium using a reaction microscope were performed by Dorn et al. (1999).

The application of the reaction microscope to the study of positron scattering is still in its infancy. These experiments combine the difficulties of producing a high intensity, high resolution positron beam and the complications of the reaction microscope coincidence measurements, resulting in only one active experiment which is based at the Australian National University.

Present Goals

In the following thesis, two pieces of experimental apparatus are discussed: the single scattering experiment and the positron reaction microscope. These apparatus are applied to the study of positron scattering from argon and C_{60}.

One of the goals of this thesis was to further develop the experimental basis for elastic and inelastic scattering of positrons from noble gases, in this case argon. Measurements of absolute elastic differential cross sections (DCS) provide more stringent tests of theoretical calculations than total scattering cross sections and, prior to this thesis, there were very few absolute experimental measurements of argon DCS. The data presented in this thesis fills in some of these gaps.

Argon was also the first target gas used in the newly-developed positron reaction microscope. A significant part of this thesis is concerned with the development of operational and data analysis techniques to allow for the study of positron-induced single ionisation of argon. Preliminary results are presented here, providing encouragement for future data collection and improvement.

The third goal, inspired by predictions from Gianturco and Lucchese (1999), was a search for resonances in the total scattering and positronium formation cross sections of C_{60}. Resonant features can appear in cross section measurements as indicators of temporary positron binding to atoms or molecules. The results of this investigation are presented in this thesis, including the first measurements of positron-C_{60} total scattering and positronium formation cross sections.

Chapter 2

Background

In the following chapter, the scattering cross section is defined and possible outcomes of positron collisions with atoms and molecules are outlined. The theoretical background used to calculate cross sections is summarised and two specific methods with particular relevance to this thesis, the relativistic optical potential (ROP) and convergent close-coupling (CCC) methods, are discussed.

2.1 Scattering Cross Sections

In general, the outcomes of a scattering event between two particles, A and B, can be separated into three types: elastic, inelastic and reaction collisions. If there is no change in the internal structure of particles A and B after scattering, the collision is elastic and can be represented as

$$A + B \longrightarrow A + B \tag{2.1.1}$$

Inelastic collisions, on the other hand, are scattering events where A, B or both, undergo a change in quantum state. For example, electronic excitation of particle B by particle A is an inelastic collision. Reaction collisions, where either or both particles form one or more new particles, are often included within the inelastic collision category. For example, direct ionisation is a reaction collision resulting in an ion and one or more ejected electrons. These collisions can be generally written as

$$\left.\begin{aligned} A + B &\longrightarrow A^* + B \\ A + B &\longrightarrow A + B^* \\ A + B &\longrightarrow A^* + B^* \end{aligned}\right\} \text{inelastic} \qquad \left.\begin{aligned} A + B &\longrightarrow C + D \\ A + B &\longrightarrow C + D + E + ... \end{aligned}\right\} \text{reaction}$$

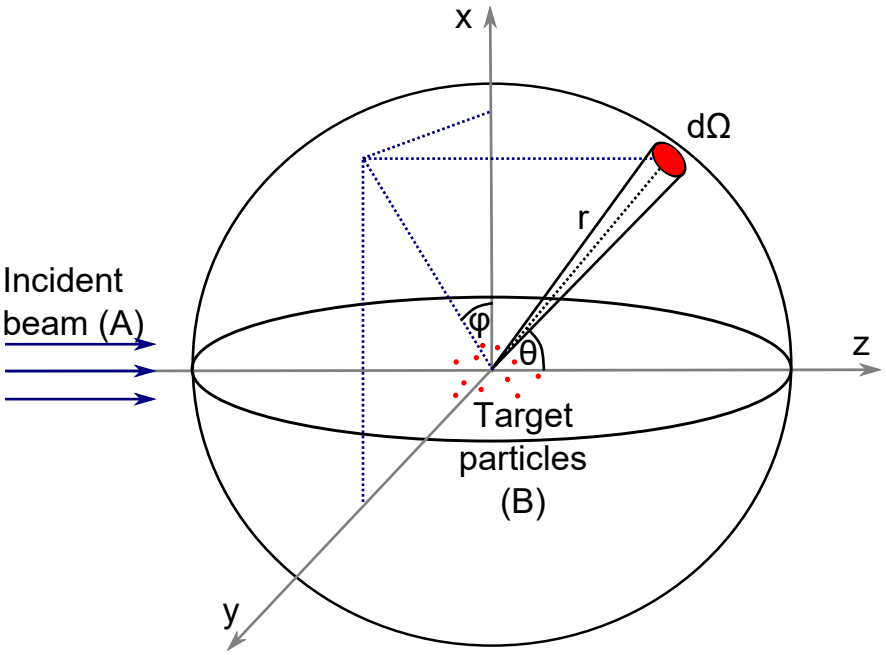

Figure 2.1.1: Schematic of a typical differential scattering geometry showing the scattering angles θ and ϕ.

The outcome of a scattering collision between particles A and B is usually described in terms of a cross section, which is defined as the ratio of the number of the specific outcome 'events' per unit time, per unit scatterer, to the relative flux of the incident particles with respect to the target. Figure 2.1.1 represents the scattering of a well collimated, monochromatic beam of identical particles (A) from a target gas (B). The incident flux, I_0, is the number of particles A per unit time which cross a unit surface area perpendicular to the direction of propagation and at rest with respect to the target. The number of particles which are then scattered elastically per unit time, per unit scatterer into a cone subtending a solid angle $d\Omega$ at the origin, (defined by the angles (θ, ϕ)) is dN_{el}. The differential elastic cross section (DCS) $\sigma_{el}(\theta, \phi)$ is defined as

$$\sigma_{el}(\theta, \phi) \equiv \frac{d\sigma_{el}(\theta, \phi)}{d\Omega} = I_0 \frac{dN_{el}}{d\Omega} \tag{2.1.2}$$

where $dN_{el}/d\Omega$ is the number of particles scattered elastically per unit time, per unit scatterer and per unit solid angle, also known as the elastically scattered flux.

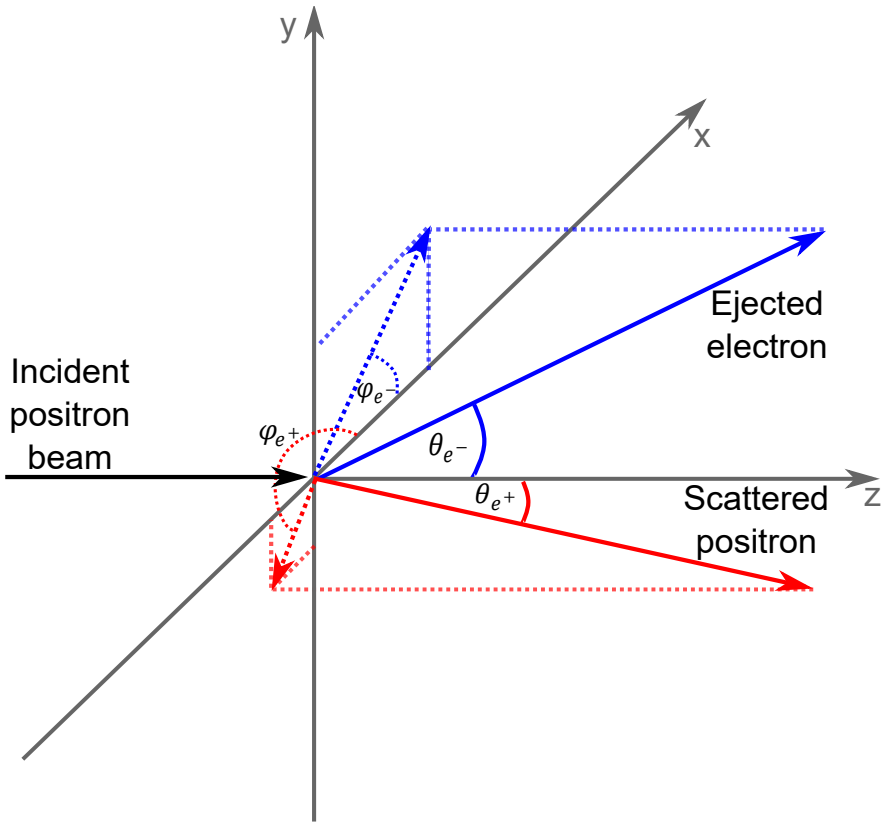

Figure 2.1.2: Geometry of a singly ionising collision for positron scattering showing the relevant scattering angles.

The total elastic cross section can be calculated by integrating equation 2.1.2 over all (θ, ϕ),

$$\sigma_{T,el} = \int \frac{d\sigma_{el}(\theta, \phi)}{d\Omega} d\Omega \tag{2.1.3}$$

The cross sections for all other processes can be calculated in a similar manner and the total cross section, σ_T is the sum of all contributing cross sections. For targets in a gaseous state, where the target density is low, the cross section is dependent only upon the properties of the incident particle beam and the target. However, the effects of close neighbouring atoms must be incorporated in order to describe scattering in, for instance, a liquid or solid.

Kinematically complete measurements require a knowledge of the momentum of all particles after the collision. For particles of known mass, their momentum is defined by three parameters: the particle's energy and the angles θ and ϕ describing the solid angle $\Omega(\theta, \phi)$ into which it is scattered. These parameters are

defined in figure 2.1.2, which represents the geometry for positron impact single ionisation of a target (the system of interest in this thesis). In general terms, for electron or positron scattering, there are N fragments following the collision. Assuming the target is initially at rest, only $3N - 3$ momentum components need be measured (Ullrich et al., 2003) in order to reconstruct the full scattering event, due to conservation of momentum. For a given scattered positron solid angle, (Ω_e^+), ejected electron solid angle (Ω_e^-) and ejected electron energy (E_{e^-}), the specific event rate $R\left(E_{e^-}, \Omega_{e^+}, \Omega_{e^-}\right)$ (the number of events per unit time) is given by,

$$R\left(E_{e^-}, \Omega_{e^+}, \Omega_{e^-}\right) = \frac{\partial^3 \sigma}{\partial E_{e^-} \partial \Omega_{e^+} \partial \Omega_{e^-}} \cdot n \cdot l \cdot \Delta E_{e^-} \cdot \Delta \Omega_{e^+} \cdot \Delta \Omega_{e^-} \tag{2.1.4}$$

where ΔE_{e^-} and $\Delta \Omega_{e^\pm}$ are the energy and solid angle intervals over which the events are detected, n is the target density and l is the length of the interaction region.

2.2 Low Energy Positron Scattering

2.2.1 Overview of Interactions

The study of positrons is interesting in its own right, but through comparison with other projectiles such as electrons, protons or antiprotons helps to illuminate the effect of different masses and charges on the scattering process. As its matter equivalent, the most frequent comparison is made between electrons and positrons and the relevant features of their interaction is summarised in table 2.1 and elaborated on below.

At low energies, less than a few hundred electron volts, the elastic scattering of a positron from a target atom or molecule could be determined by, for example, considering the interaction between the core and each individual electron with the positron or by defining an interaction potential consisting of static and polarisation potentials. In the following discussion, the focus will be on the latter method. Both the static and polarisation potentials are due to the Coulomb interaction between the positron and target. The static potential is short range

	Electron	**Positron**
Static interaction	attractive	repulsive
Polarisation interaction	attractive	repulsive
Exhange interaction	yes	no
Positronium formation	no	yes
Electron-positron annihilation	no	yes

Table 2.1: Comparison of the key features of the interactions of positrons and electrons with atoms. Reproduced from Charlton and Humberston (2000, p. 35).

and decays exponentially with distance from the target. In contrast to electron scattering, this potential is repulsive for the positron scattering meaning that the positron does not typically penetrate deeply into the atom or molecule's charge cloud.

The polarisation potential arises as the charged projectile approaches the target, causing a distortion of the target's charge cloud thereby inducing a dipole (or multipole) moment which, in turn, interacts with the incident particle. This is described by a long range and attractive potential for both positron and electron scattering. The magnitude of the polarisation potential varies from target to target depending upon the polarisability of the target's electron cloud.

In the case of positron scattering from polar molecules, there is also a permanent dipole moment which is an attractive, long range interaction and its strength is dependent upon the degree of polarity of the target. While there may be variations in oriented molecules, this description is true on average for unoriented molecules.

The exchange interaction is an important interaction for low energy electron scattering, where it manifests as a non-local potential. During exchange, the projectile electron replaces one of the target's electrons, and can result in the excitation of all electronic states, assuming the projectile has sufficient energy. This means the spin angular momentum of the target may change after scattering. However, there is no exchange interaction for positron scattering as the positron is distinctly different from the target electrons. In positron scattering only transitions where the total spin state of the target remains unchanged are accessible. For example, an electron scattering from ground state helium can excite the 2^3S state with an energy of 19.8 eV, but the first state positrons can excite is the 2^1S state at 20.58 eV (NIST, 2018).

The result of these differences in the sign of the static potential and the lack of the exchange interaction for positrons mean that at low energies (tens of eV) the total scattering cross section for positrons is often significantly smaller than for electrons.

2.2.2 Positron Scattering Outcomes

Positron scattering can have a number of different outcomes, dependent upon the energy of the positron and the properties of the target. Table 2.2 lists some of the most common collision processes.

Scattering Channel		**Threshold Energy**
Elastic Scattering	$e^+ + A \longrightarrow e^+ + A$	0 eV
Electronic Excitation	$e^+ + A \longrightarrow e^+ + A^*$	several eV
Ionisation	$e^+ + A \longrightarrow e^+ + A^{n+} + ne^-$	several eV (E_{ion})
Positronium formation	$e^+ + A \longrightarrow A^+ + Ps$	$E_{ion} - 6.8$ eV
Annihilation	$e^+ + A \longrightarrow e^+ + A^+ + n\gamma$	0 eV

Table 2.2: A list of the main scattering processes available for positron-atom collisions, where A is an atomic target and E_{ion} is the ionisation threshold for A

Elastic scattering generally refers to scattering where the energy of the projectile positron is unchanged by the scattering event, whereas following an inelastic interaction the positron loses energy to the target atom or molecule. At low energies, typically from a few hundred meV to a few eV, positron scattering from molecules can also result in vibrational or rotational excitations of the target.

Positronium (Ps) is a hydrogen-like, neutral bound state of a positron and an electron. It can be formed in two different spin states: the singlet, para-positronium (para-Ps), with S=0, and the triplet, ortho-positronium (ortho-Ps), with S=1. In scattering, these are produced with a ratio of ortho-Ps to para-Ps of approximately 3:1. As Ps consists of an electron and a positron it eventually decays, usually through self-annihilation, with the lifetime depending upon its spin state- 125 ps for para-Ps, and 142 ns for ortho-Ps. The combination of charge conjugation invariance means that Ps must decay into n_γ gamma-rays, determined by

$$(-1)^{n_\gamma} = (-1)^{L+S} \tag{2.2.1}$$

where S is the spin and L is the orbital angular momentum (Yang, 1950; Wolfenstein and Ravenhall, 1952). Ground state Ps, where $L = 0$, must produce either even numbers of gamma-rays (para-Ps) or odd numbers (ortho-Ps). Experimentally, only decay into 2 (para) or 3 (ortho) gamma-rays has been observed, although there are claims of observation of zero and one gamma-ray photon decay (Shimizu et al., 1968).

The threshold for Ps formation is given by

$$E_{ion} - \frac{6.8}{n_{Ps}^2} eV \tag{2.2.2}$$

where E_{ion} is the ionisation threshold of the target and n_{Ps} is the principal quantum number of the Ps atom. Therefore, for ground state Ps, the threshold is simply 6.8 eV below the first ionisation threshold of the target. For most atoms and molecules, this Ps threshold is at a positive energy although for the alkali atoms, where the ionisation threshold is $< 6.8\ eV$, ground state Ps can be formed even at zero incident energy. The Bohr energy levels for Ps are approximately the same as those for an infinite mass hydrogen atom, but are reduced by 1/2 as the reduced mass of Ps is $m_e/2$ or about half that of hydrogen.

As discussed above, the lack of exchange interaction in positron scattering limits the electronic excitations that are possible to those where the total spin state of the target remains the same after scattering. This means that the first open electronic excitation can be at a higher energy than for electrons. The energy gap between the Ps formation threshold and this first available electronic excitation channel is known as the Ore gap (Charlton and Humberston, 2000, p. 38).

Direct ionisation, where the target loses one or more electrons after the collision, is a process which can be difficult to distinguish from Ps formation as both scattering processes result in a positively charged ion. Near the ionisation threshold, the cross sections for ionisation and Ps formation can be comparable in magnitude and it can be difficult to distinguish between the formation of Ps into very highly excited, or continuum states (which result in a weakly bound or unbound positron) and direct ionisation. This produces significant difficulties for theoretical treatments of near threshold direct ionisation. However, as the incident positron energy is increased to around 200 eV the Ps formation cross section becomes negligible and ionisation dominates. If the kinetic energy of the recoil

ion after ionisation is negligible, then it is reasonable to assume that system's residual energy (after allowing for the loss of energy required to ionise the target) is split between the positron and ejected electron.

Direct annihilation, in contrast to annihilation following Ps formation, may proceed through a range of paths including radiationless, 1γ, 2γ and higher numbers of gamma-rays. The most probable annihilation path results in two gamma-rays emitted back to back, each with an energy of 511 keV. Radiationless and 1γ annihilations are very improbable as they must involve the target nucleus or inner shell electrons in order to conserve energy and momentum. 3γ annihilation has a probability of approximately $\frac{1}{370}$ th of 2γ annihilation, and as the number of emitted gamma-rays increases this probability reduces further. Direct annihilation for positron scattering in low density gases is very unlikely, with a cross section of around 10^{-5} less than the other scattering processes. However, at very low impact energies (a few tens of meV) this annihilation cross section is enhanced by positron binding and vibrational Feshbach resonances present in certain molecules (Natisin et al., 2017).

There are various additional processes that can occur when a positron scatters from a target atom or molecule. For example, an electron can bind to a positronium atom (if both electrons are in a singlet spin state) to a form a positronium negative ion, Ps^- and was first observed by Mills (1981). In addition, there are states where a positron temporarily binds to an atom or molecule (Mitroy et al., 2002; Barnes et al., 2003).

2.3 Scattering Theory

The discussion of scattering theory in this section applies to elastic scattering of a positron from an atom or molecule, therefore the exchange interaction is excluded.

The simplest scattering system consists of two particles, A and B with masses m_A and m_B at coordinates $\boldsymbol{r}_A$ and $\boldsymbol{r}_B$ in relation to a fixed origin, which interact through an interaction potential $V(\boldsymbol{r}_A - \boldsymbol{r}_B)$. In this formalism, the motion of the particles is a many-body problem which is difficult to solve. This can be rewritten in the centre-of-mass system as the scattering of a particle of mass $m = m_A m_B/(m_A+m_B)$ (the reduced mass) at the relative coordinate $\boldsymbol{r} = \boldsymbol{r}_A - \boldsymbol{r}_B$

in the same potential $V(\boldsymbol{r})$. The calculation of theoretical cross sections, in this form, requires the solution of the time-independent Schrödinger equation,

$$H\psi(\boldsymbol{r}) = E\psi(\boldsymbol{r}) \tag{2.3.1}$$

where $\psi(\boldsymbol{r})$ is the wavefunction of the system and E is the energy of the incident particle. H is the Hamiltonian which takes the general form

$$H = -\frac{\hbar^2}{2m}\nabla^2 + V(\boldsymbol{r}) \tag{2.3.2}$$

where $V(\boldsymbol{r})$ in this case is a central potential, assumed to be spherically symmetric about angles θ and ϕ, dependent only on r, and ∇^2 is the Laplacian operator. This is true for atomic charge clouds, however this is not the case for scattering from molecules or in the modelling of positronium formation.

In the case of a potential, where $V(\boldsymbol{r}) \to 0$ faster than r^{-1} as $r \to \infty$, the solution of 2.3.1 satisfies the asymptotic condition,

$$\psi(\boldsymbol{k}, \boldsymbol{r}) \underset{r\to\infty}{\longrightarrow} A(k)\left[\exp^{i\boldsymbol{k}\cdot\boldsymbol{r}} + f(\theta,\phi)\frac{\exp^{ikr}}{r}\right] \tag{2.3.3}$$

where $\boldsymbol{k}$ is the wave vector of the incident particle (and $|\boldsymbol{k}| = k$, the wavenumber) and $A(k)$ is a normalisation constant. Equation 2.3.3 shows that when r is large, the wavefunction is described by the superposition of an incident plane wave and an outgoing spherical wave modulated by the scattering amplitude $f(\theta, \phi)$. These scattering amplitudes are used to calculate the elastic differential and total cross sections.

2.3.1 The Method of Partial Waves

If a system has a central potential, where V is dependent only upon the scalar r as in 2.3.2, it is possible to find the scattering amplitude using the method of partial waves. In spherical polar coordinates, the Laplacian operator in 2.3.2 is

$$\nabla^2 = \frac{1}{r^2}\frac{\partial}{\partial r}\left(r^2\frac{\partial}{\partial r}\right) + \frac{1}{r^2\sin\theta}\frac{\partial}{\partial\theta}\left(\sin\theta\frac{\partial}{\partial\theta}\right) + \frac{1}{r^2\sin^2\theta}\frac{\partial^2}{\partial\phi^2} \tag{2.3.4}$$

Also in spherical polar coordinates, the square of the total orbital angular momentum operator is

$$ {l_{op}}^2 = \boldsymbol{l}_{op} \cdot \boldsymbol{l}_{op} = -\hbar^2 \left[\frac{1}{\sin\theta} \frac{\partial}{\partial\theta} \left(\sin\theta \frac{\partial}{\partial\theta} \right) + \frac{1}{\sin^2\theta} \frac{\partial^2}{\partial\phi^2} \right] \tag{2.3.5} $$

The total orbital angular momentum operator's projection along the z axis is

$$ l_z = -i\hbar \frac{\partial}{\partial\phi} \tag{2.3.6} $$

Since ${l_{op}}^2$ and l_z commute with the Hamiltonian, H ($\left[{l_{op}}^2, H\right] = [l_z, H] = 0$), and given that the wavefunction is symmetric about the z axis, it is possible to expand $\psi(\boldsymbol{k}, \boldsymbol{r})$ as a sum of partial waves

$$ \psi(\boldsymbol{k}, \boldsymbol{r}) = \sum_{l=0}^{\infty} a_l(k) \frac{u_l(r)}{r} P_l(cos\theta) \tag{2.3.7} $$

where $a_l(k)$ are coefficients to be determined, $P_l(cos\theta)$ are the Legendre polynomials of degree l and $u_l(r)$ are the radial part of the scattering wavefunction and are solutions of the differential equation

$$ \left[\frac{d^2}{dr^2} - \frac{l(l+1)}{r^2} - U(r) + k^2 \right] u_l(r) = 0 \tag{2.3.8} $$

where $U(r) = 2mV(r)/\hbar^2$, which is the so-called reduced potential and where m is the reduced mass, equal to the positron mass in this case. Asymptotically, where $V(r) = 0$, the solution to 2.3.8 can be expressed in terms of the Riccati-Bessel ($\hat{\jmath}_l(kr)$) and Riccati-Neumann ($\hat{n}_l(kr)$) functions, which asymptotically are

$$ \hat{\jmath}_l(kr) \sim \sin\left(kr - \frac{l\pi}{2} \right) \qquad kr >> l \tag{2.3.9} $$

and

$$ \hat{n}_l(kr) \sim -\cos\left(kr - \frac{l\pi}{2} \right) \qquad kr >> l \tag{2.3.10} $$

respectively. If $U(r) \to 0$ faster than r^{-1} as $r \to \infty$, then 2.3.9 and 2.3.10 can be used to write $u_l(r)$ asymptotically as

$$ u_l(r) \underset{r\to\infty}{\longrightarrow} A_l(k) \sin\left(kr - \frac{l\pi}{2} \right) + B_l(k) \cos\left(kr - \frac{l\pi}{2} \right) \tag{2.3.11} $$

where $A_l(k)$ and $B_l(k)$ are coefficients. (2.3.11) can also be written as

$$u_l(r) \underset{r\to\infty}{\longrightarrow} C_l(k)\sin\left(kr - \frac{l\pi}{2} + \delta_l(k)\right) \tag{2.3.12}$$

where $\delta_l(k)$ is the phase shift and

$$C_l(k) = \mathrm{sgn}(A_l(k))\left[A_l^2(k) + B_l^2(k)\right]^{\frac{1}{2}} \tag{2.3.13}$$

where $\mathrm{sgn}(A_l(k))$ represents the sign of $A_l(k)$. The phase shifts in (2.3.12) correspond to different angular momentum values and are commonly referred to as s-wave ($l = 0$), p-wave ($l = 1$), d-wave ($l = 2$) etc phase shifts.

In all real atomic systems, the form of $U(r)$ means that (2.3.8) must be solved numerically as analytical solutions do not exist. It is possible to rewrite (2.3.3) using the Rayleigh formula for the expansion of a plane wave, $\exp^{ikz}$ and setting the normalisation constant $A(k) = 1$, as

$$\psi(\boldsymbol{k}_i, \boldsymbol{r}) \underset{r\to\infty}{\longrightarrow} \sum_l (2l+1)\frac{1}{2ikr}\left[\exp ikr - (-1)^l \exp -ikr\right] P_l(\cos\theta) + f(\theta,\phi)\frac{\exp ikr}{r} \tag{2.3.14}$$

Upon substitution of 2.3.12 into 2.3.7 and setting this equal to 2.3.14, the scattering amplitude is

$$f(\theta,\phi) = f(\theta) = \sum_{l=0}^{\infty}(2l+1)c_l(k)P_l(cos\theta) \tag{2.3.15}$$

where it is assumed that there is axial symmetry about the z axis and hence the scattering amplitude is independent of ϕ. The coefficients $c_l(k)$, the partial wave amplitudes, are

$$c_l(k) = \frac{1}{k}\exp i\delta_l(k) sin(\delta_l(k)) \tag{2.3.16}$$

The cross sections can be directly calculated from the scattering amplitude. The elastic differential cross section is simply

$$\begin{aligned}\sigma_{el}(\theta) &= |f(\theta)|^2 \\ &= \left|\frac{1}{k^2}\sum_{l=0}^{\infty}(2l+1)^2 \exp 2i\delta_l(k) sin^2(\delta_l(k))(k)P_l^2(cos\theta)\right|\end{aligned} \tag{2.3.17}$$

The total elastic cross section is then obtained from (2.3.18) by integrating over the angles θ and ϕ

$$\begin{aligned}\sigma^{el}_{total}(k^2) &= 2\pi \int_0^{\pi} \sin\theta \, |f(\theta)|^2 \, d\theta \\ &= \frac{4\pi}{k^2} \sum_{l=0}^{\infty} (2l+1) \sin^2(\delta_l(k))\end{aligned} \tag{2.3.18}$$

Elastic scattering from spherically symmetric targets can be represented using real phase shifts (s, p, d, f etc) calculated from the equations given above. The phase shifts at the scattering energy are used to calculate the total and differential elastic cross sections, where the relative strength of the phase shifts gives the angular dependence. Although the p-wave ($l = 1$) and higher partial waves will not have a smaller effect on the total cross sections compared to the s-wave, these phase shifts can affect the shape of the DCS especially at small and large angles and models usually use hundreds of phase shifts. For example, the s-wave generally produces an isotropic DCS (i.e. where the cross section is independent of the angle θ), if the p-wave shift is appreciably different from zero, the p-wave contribution will increase the scattering at 0° and 180° with respect to the incident beam. If the s-wave is zero at some low scattering energy, targets such as neon (Jones et al., 2011) exhibit a Ramsauer-Townsend minimum, a decrease in the total cross section which is especially deep if the p-wave also tends to zero at a comparable energy (Ramsauer, 1921; Townsend and Bailey, 1921). Additionally, 'cusps', small features in the total or elastic scattering cross sections can arise due to the opening of a new, strong scattering channel (Wigner, 1948). These have been observed experimentally in the total elastic cross sections for positron scattering from noble gases at the positronium (Ps) formation threshold (Jones et al., 2010).

2.3.2 Theoretical Models

The solution to the scattering problem, as discussed above, can be difficult and a range of approaches have been developed to solve it for different targets. One complication for these models is that inelastic scattering channels such as ionisation or positronium formation must be included as they can have a significant

effect on the total cross section above their respective thresholds. In addition, the description of the target can be complicated, especially if it is a molecule rather than atom as additional degrees of freedom need to be included in the target description and it will break the conditions described previously which are valid for a spherically symmetric potential. Many theoretical methods have been developed to solve the scattering problem, including the Kohn-variational method (e.g. Humberston (1973) applied to positron-helium scattering), the modified effective range theory (MERT) (e.g. Idziaszek and Karwasz (2006) applied to positron-argon and positron-nitrogen scattering), the Convergent Close Coupling (CCC) method (e.g. Kernoghan et al. (1996); Kadyrov and Bray (2002) applied to positron-hydrogen scattering) and the relativistic optical potential (ROP) method (e.g. Bartschat et al. (1988); Chen et al. (2008)). These methods have been used for a range of electron and positron scattering systems, in some cases for several decades, however, for positron scattering most models are applied only to total cross sections and simple targets such as noble gases. Their agreement with each other, and with experiment, can be variable depending upon the target in question and the incident positron energy.

In the section below, two methods only are outlined: the ROP method and the CCC method, as these are the theories used for comparison with the single scattering data presented in chapter 6. Chapter 6 presents work on postron-argon scattering, covering differential elastic scattering, total elastic and total inelastic cross sections. In these cases, the only theory available was the ROP and CCC methods and therefore it is superfluous for this thesis to discuss other theoretical methods in detail. As the work in chapter 6 focuses on atoms, the descriptions below are applicable only for positron scattering from atoms.

Relativistic Optical Potential

The relativistic optical potential (ROP) method attempts to solve the time-independent Dirac equation, incorporating the inelastic channels corresponding to electronic excitation and ionisation as well as elastic scattering (the current form is outlined in Chen et al. (2008)). The optical potential consists of a real part, describing elastic scattering, and an imaginary part, often referred to as an absorption potential, representing the loss of flux to inelastic channels. In these cases, the phase shifts, $\delta_l(k)$, become complex. The real potential used, in an

atomic system, is a combination of the static $U_{static}(r)$ and polarisation $U_{pol}(r)$ potentials

$$\Re[U(r)] = U_{static}(r) + U_{pol(}r) \tag{2.3.19}$$

Earlier versions of the ROP did not include Ps formation, which can make a significant contribution to the total cross section. By noting the similarities between ionisation and Ps formation, more recent models have simulated Ps formation (McEachran and Stauffer, 2013) in the absorption potential. This addition affects the shape and magnitude of the elastic differential cross sections above the Ps formation threshold, and often decreases the size of some previously predicted features and increases the forward angle scattering.

Close Coupling and Convergent Close Coupling

The close coupling (CC) method attempts to solve equation 2.3.1 by expanding the wavefunction, Ψ, over a complete set of eigenfunctions. In the most complete two-centre formulation Utamuratov et al. (2010), Ψ is given by

$$\Psi = \sum_a F_a(\boldsymbol{x}_0)\Phi_a(\boldsymbol{x}_1, ..., \boldsymbol{x}_N) + A\sum_{bc} G_{bc}(\boldsymbol{R}_1)\phi_b(\boldsymbol{t}_1)\Phi_c^+(\boldsymbol{x}_1, ..., \boldsymbol{x}_{N-1}) \tag{2.3.20}$$

where the first term uses the atomic states $\Phi_a(x_1, ..., x_N)$, with $F_a(x_0)$ as the positron scattering functions. The second term is the expansion about the Ps centre of mass, where A is an antisymmetrization operator which operates on $\phi_b(t_1)$, the Ps states. $G_{bc}(R_1)$ are the Ps scattering functions and $\Phi_c^+(x_1, ..., x_{N-1})$ are the states of the residual ion. This full description is particularly difficult to calculate and currently has only been solved to a high degree of accuracy for the simplest positron-hydrogen scattering system (Kernoghan et al., 1996; Kadyrov and Bray, 2002). The next simplest system, positron-helium scattering, has been solved using a two-centre method but required some approximations, introducing errors which are of particular concern near the Ps formation threshold (Utamuratov et al., 2010). As the scattering systems become more complex, the two-centre method must be reduced to a single-centre method (Fursa and Bray, 2012) to allow for calculation. This method drops the second term of equation 2.3.20,

meaning that Ps is no longer explicitly included. However, by adjusting the target state expansion it is possible to model Ps formation reasonably. The wavefunction is then substituted into equation 2.3.1 to find a system of coupled differential equations.

The convergent close coupling (CCC) method is based on the CC method and employs pseudostates to describe the excited states of the target electrons into the continuum and Ps formation. This treatment of the continuum states is the main strength of the CCC method and allows a more complete description of the scattering system, although approximations must still be made in order to solve the ensuing equations.

Chapter 3

Experimental Apparatus

The results presented in this thesis were collected using the same positron source and trap apparatus (section 3.1), but with different scattering and detection stages. Single scattering cross sections (such as total scattering or differential scattering) were collected using the single scattering stage and detection (section 3.2), whereas fully differential cross sections used the positron reaction microscope (section 3.3).

In this chapter, I will outline the experimental setup for these two experiments, reserving a detailed discussion of the operation procedure and data analysis methods for chapters 4 and 5. The single scattering apparatus was developed by Jones (2010), although since then I was involved in the design and implementation of an oven to the scattering stage (section 3.2.1). The reaction microscope spectrometer, drift tubes and detectors were constructed prior to this thesis and I contributed to the data acquisition system development (section 3.3.4), working with Simon Armitage and Dennis Mueller of the University of North Texas in 2013, and modifying this with Dennis Mueller in 2014.

3.1 Trap and Beam Formation

The trap and beam formation sections of the beamline are common to both the single scattering and positron reaction microscope experiments, although there are differences in the selection of potentials and magnetic fields between the two experiments. The following discussion uses typical settings for the single scattering experiment, and the changes made to these settings for the reaction microscope are detailed in section 3.3.

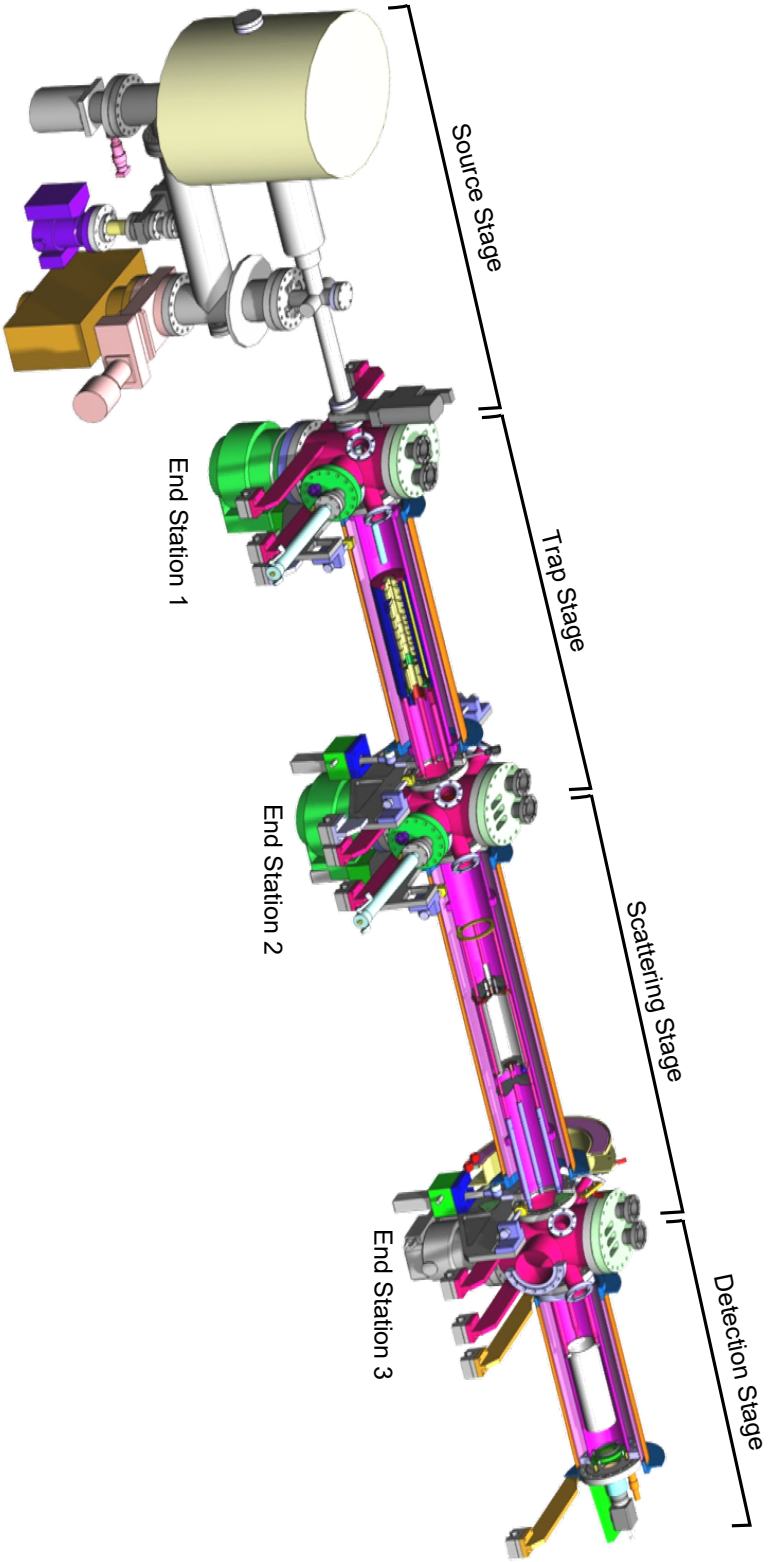

Figure 3.1.1: Schematic of the beamline

The complete single scattering experiment, including the source, trap and scattering and detection stages is shown in figure 3.1.1). Each stage is separated by an end station and the chambers are surrounded by solenoids producing a magnetic field to guide the positrons along its length. The entire beamline is under high vacuum, typically $\sim 1 \times 10^{-9}$ Torr, provided by turbomolecular pumps backed by mechanical roughing pumps in the source stage and at each end station.

3.1.1 Source Stage

The source stage (see figure 3.1.2) is designed to produce a moderated beam of positrons from a radioactive source. The source stage was manufactured by First Point Scientific, Inc. and includes the source assembly, vacuum system and solenoids for radial beam confinement and additional coils for velocity discrimination. It also includes a cryogenic coldhead and gas handling setup which are used to grow solid neon moderators. The sources stage pressures and temperatures and monitored continuously through Labview software. A substantial amount of radiation shielding, in the form of lead shot, surrounds the source assembly to reduce exposure to ionising radiation.

Radioactive Source

The positron source used is the radioactive isotope Sodium-22 (^{22}Na) which has a half life of 2.6 years and the source in these experiments has an initial activity level of 50 mCi. Positrons are produced through β^+ decay in the decay process

$$^{22}_{11}\mathrm{Na} \rightarrow {}^{22}_{10}\mathrm{Ne} + e^+ + \nu_e + \gamma(1.27\ MeV) \tag{3.1.1}$$

which produces positrons in ∼91% of decays, with the other 9% of ^{22}Na isotopes decay through electron capture and do not produce positrons (Allen et al., 1955). The positrons emitted by the source have a wide energy range up to 0.54 MeV (Allen et al., 1955). A solid neon moderator is used to reduce this energy spread to produce the more monochromatic beam necessary for low energy scattering experiments.

The source is held in a Halle-b type mount constructed from elkonite (a dense material with a 7:3 ratio of tungsten to copper) covered in a thin layer of titanium.

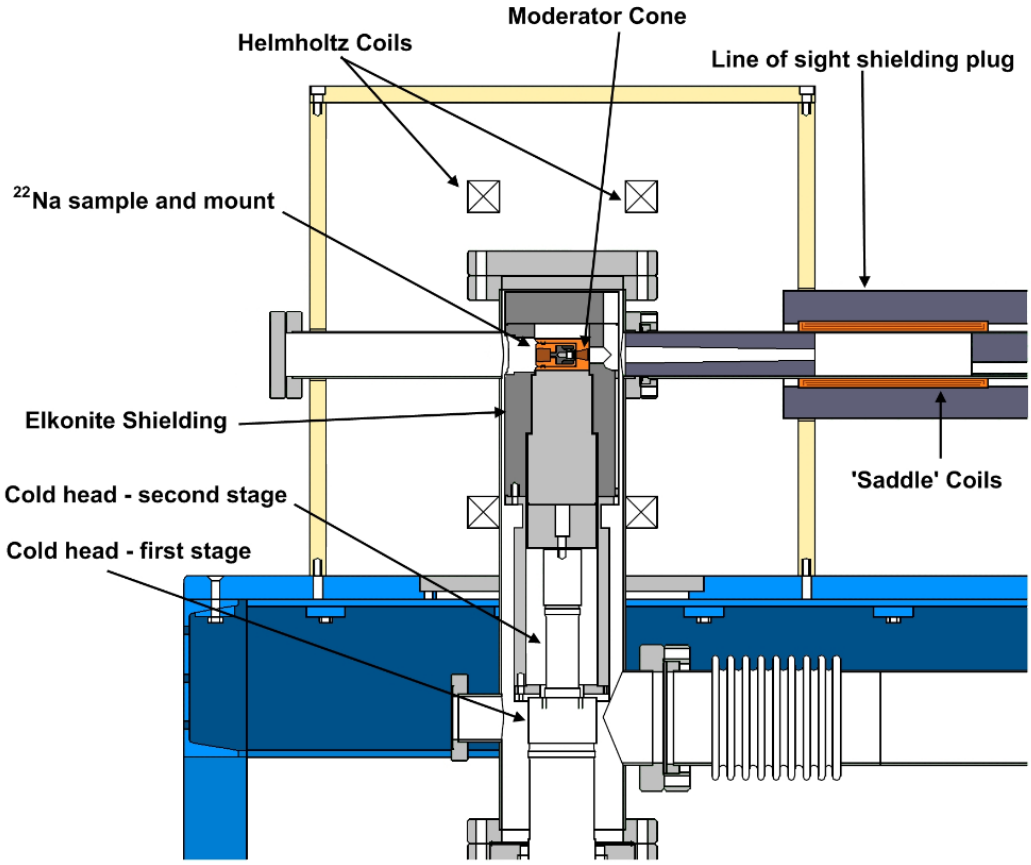

(a) Source Stage

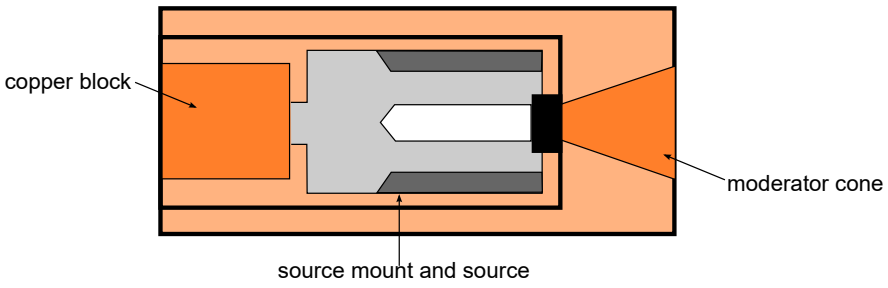

(b) Source Mount

Figure 3.1.2: a) Schematic of the source stage, reproduced from Jones (2010). The beam tube extends from the saddle coils, downstream from the source, and is blocked by a gate valve. b) Schematic of the source mount including the conical copper moderator cone where the moderator is grown.

The dense elkonite and titanium mount increases positron intensity by reflecting positrons which are ejected backwards. The source mount is attached to a solid copper block and faces a conical copper surface upon which the moderator is grown (see figure 3.1.2b). The copper block is situated on top of a cryogenic coldhead assembly (Advanced Research Systems, model DE204) which is capable of keeping the copper surface at a constant temperature of 7-8.5 K to facilitate the growth of a solid neon moderator. The moderator efficiency, defined as the ratio between the number of positrons in the beam compared to the number of positrons emitted by the source, is $\sim$1% and the energy spread of the beam after moderation is 1.5-2 eV (Mills and Gullikson, 1986) confirmed in this experimental setup by Jones (2010)).

The radioactive decay of ^{22}Na produces high energy γ rays, thus requiring shielding to provide a safe working environment. The source assembly is surrounded by an elkonite block, the dense material providing some shielding and this is contained within a vacuum system. The whole system is then encapsulated in a lead shot filled canister, providing around 10 cm of shielding. Due to the positioning of the vacuum system, some additional external lead shielding is included to reduce the γ ray solid angle, for example at the join between the beam tube and the source assembly. Overall, the shielding reduces ionising radiation to background levels at a distance of $\sim$1 m.

Source Stage Vacuum System

The vacuum in the source stage is provided by a turbomolecular (turbo) pump, backed by a mechanical roughing pump capable of achieving pressures of 10^{-3} Torr. Additional pumping is provided by the coldhead, although this can have a negative impact on the experimental setup as impurities in the moderator reduce its efficiency. To mediate this, the coldhead is pumped and baked thoroughly before initial operation. Generally, the background gases in the source chamber should be mostly neon with some nitrogen from the trap. The source stage vacuum system produces a vacuum of 10^{-9} Torr without a moderator and 10^{-7} Torr under normal operating conditions with a moderator, which is consistent with the vapour pressure at 7 K.

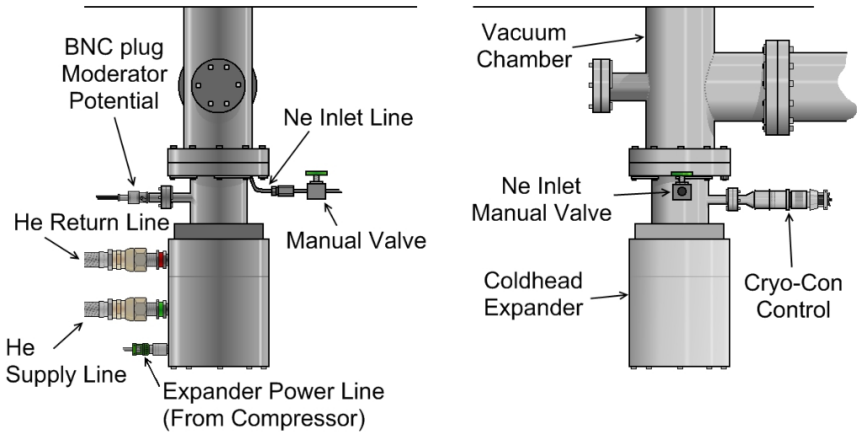

Figure 3.1.3: Schematic of the source stage coldhead viewed from underneath the source stage assembly, reproduced from Jones (2010).

The Coldhead

The coldhead is manufactured by Advanced Research Systems and is model DE204, a schematic view of its attachment is shown in figure 3.1.3. It uses the compression and expansion of ultra high purity helium gas to cool through two stages, the first can achieve 30 K and the second is capable of producing temperatures as low as 5 K. However, due to the thermal mass of the source assembly the achieved minimum temperature is 6.5 K. The required temperature for solid neon moderator growth is only around 7 to 10 K, well within the capabilities of the coldhead. The coldhead temperature is maintained through use of a heating element positioned around 10 cm above the source mount, this element is used to provide consistent temperatures for the moderator growth cycle and maintenance. A Cryo-Con 34 Temperature Controller monitors a diode attached to the top of the source mount block and is able to record and maintain temperature with a precision of 0.1 K.

Moderator Gas System

Moderators are generally grown in an automated process made possible by the moderator gas handling system shown in the schematic in figure 3.1.4. Ultra high purity neon gas (99.999%) neon is attached to a pressure regulator set at $\sim$5 to 10 atm. A computer-controlled piezoelectric needle valve admits neon gas into

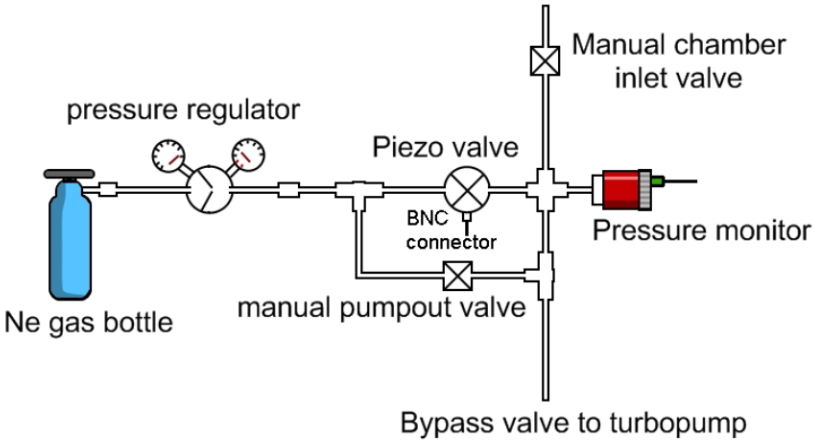

Figure 3.1.4: Schematic of the moderator gas handling system, reproduced from Jones (2010).

the source stage and the pressure of the neon gas is monitored by a Proportional-Integral-Derivative (PID) controller close to the needle valve. During the growth period, the pressure at this point is 1×10^{-4} Torr. Following growth, the needle valve is closed and the residual neon gas is removed by the turbo pump.

Magnetic Confinement and Guidance

Moderated positrons need to be extracted and guided from the moderator region along the beam tube and into the rest of the beamline. This is done through the use of electric and magnetic fields. In the moderator region there are a pair of Helmholtz coils, shown in figure 3.1.2, with diameters of 15 cm, providing a magnetic field of 88 G. A positive potential bias is applied to the moderator to accelerate positrons away from this area and towards the beam tube, where a solenoid applies an axial magnetic field of 273 G. There are two non-axial saddle coils which produce a 'kink' in the magnetic field. Moderated positrons follow the field lines and are guided up, through the off-axis beam tube, and down, through the on-axis beam tube, whereas unmoderated positrons hit the shielding and annihilate. Therefore only moderated positrons are extracted beyond the source stage.

In addition to the main source stage solenoids, there is one at the the beam tube gate valve and a second at end station one which produces a magnetic field perpendicular to the beam axis. These are used to provide fine tuning of

the magnetic field, allowing for optimisation of the beam alignment between the source and trap stages. The magnets use water cooling to prevent overheating and damage and the temperature of the beam tube magnet is monitored and connected to an interlock system to turn off the solenoid power supplies if it rises above 70 °C.

3.1.2 Trap Stage

A buffer gas trap further improves the energy resolution of the moderated positrons and produces a pulsed beam. The trapping of positrons originated when Dehmelt et al. (1978) modified a Penning discharge tube to store electrons and proposed their application to the trapping of positrons. In 1980, Malmberg and Driscoll (1980) developed this concept further, using cylindrical confinement electrodes to successfully store electron plasmas, thus creating the 'Penning-Malmberg' trap. The inclusion of buffer gases (initially N_2 and later also CF_4) to the Penning-Malmberg trap setup slowed the incoming positrons down, cooling them to room temperature (Surko et al., 1989). The trap employed in this work is based on the techniques developed by the Surko group at the University of San Diego (Murphy and Surko, 1992) and is often referred to as a 'Surko' buffer gas trap.

The trap stage includes the trap itself, the magnetic confinement solenoid and pumping at end stations one and two. In addition, two beam flags are generally located at end stations one and two which can be moved into the beam to assess the trap efficiency. These beam flags are relocated to different end stations as required by the specific experiments.

Magnetic Confinement and Vacuum System

The trap sits inside a solenoid constructed from thick copper wire, wrapped around a water jacketed steel chamber and supported by manually controlled jacks providing vertical movement and adjustable bolts providing horizontal movement. A current of 15 A is provided to the solenoid, producing an axial magnetic field of 530 G. Positrons are confined by the magnetic field and the ability to physically move the the solenoid allows for precise 'tuning' of the magnetic field to maximise the transmission of positrons from the source stage and through the trap stage.

The trap assembly is centred within the solenoid's field in a region with very little variation in the magnetic field strength.

Pumping is provided at end stations one and two by turbo pumps, backed by mechanical roughing pumps capable of achieving pressures of 10^{-3} Torr. In the absence of gases in the trap stage, these pumps provide a vacuum of 10^{-9} to 10^{-8} Torr, measured in the end stations. There are differential pumping tubes at each end of the trap stage: at the trap entry there is a tube with a diameter of 10 mm and length 194 mm, at the trap exit there is a tube with a diameter of 28 mm and a length of 151.4 mm. This results in asymmetric pumping and lowers the pressure in the second stage of the trap, extending the lifetime of positrons in this region. The pressures at each end station are monitored using Pirani-ion gauges.

The Trap Assembly

The trap consists of nine cylindrical, gold-plated copper electrodes, as shown in figure 3.1.5. The first three electrodes (forming stage 1) have an internal diameter of 1 cm, the first electrode is 2 cm long and the second and third are 4 cm. Nitrogen (N_2) is admitted into the trap through an inlet at the second electrode. These electrodes are electrically isolated from each other by insulating spacers which also provide a gas seal. Electrodes four to nine (stage 2) are larger, with an internal diameter of 2 cm and electrodes four to eight have a length of 3 cm. The sixth electrode, or rotating wall, has four electrically isolated segments and can increase the beam intensity by radially compressing the beam (based on the principles from Greaves and Moxom (2008)), although this can be at the expense of the energy resolution. The final, ninth electrode has a length of 6 cm and the whole trap assembly is surrounded by a grounded, stainless steel outer housing. Tetrafluoromethane (CF_4) is admitted into the space between the outer housing and the trap, small ruby balls separate the second stage electrodes, electrically isolating them and allowing the gas to diffuse into the trap.

The N_2 and CF_4 gas systems have a driving pressure of around 100-200 mTorr and 8-14 mTorr respectively while the actual pressure inside the trap is much lower at approximately 4-5 mTorr (N_2) or 0.1 mTorr (CF_4).

The operation procedure for the trap, to produce the pulsed beam used for single scattering experiments, is outlined in section 4.2.2.

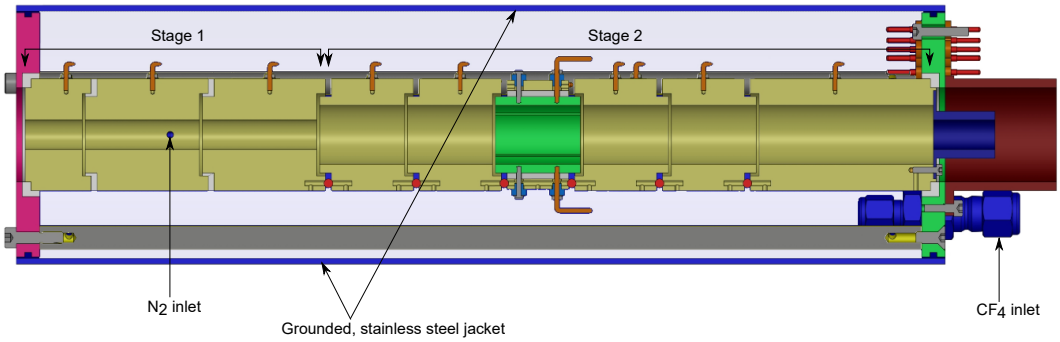

Figure 3.1.5: A schematic of the trap setup. Labels indicate the gas inlets for CF_4 and N_2 as well as the outer housing - a grounded, stainless steel jacket. Reproduced from Jones (2010), with some additional labels.

3.2 Single Scattering Stage and Detection

The single scattering stage of the beamline includes a retarding potential analyser and a gas cell, whereas the detection stage consists of a second retarding potential analyser and a microchannel plate used to collect scattered positrons. The setup also incorporates pumping at end station three, a large solenoid around the scattering stage, a smaller solenoid around the second retarding potential analyser and a small additional magnet around the microchannel plate in the detection stage.

Magnetic Confinement and Vacuum System

Axial magnetic fields are again used to confine the positron beam and scattered positrons after the scattering stage. The solenoid around the scattering stage (SC solenoid) is similar to the trap magnet, consisting of thick copper wire wrapped around a water jacketed cylindrical chamber and mounted to allow for manual control of vertical and horizontal positioning. A second, shorter solenoid (RPA2 solenoid), with the same design features, surrounds the second retarding potential analyser (RPA2) at the beginning of the detection stage, however, the position of this solenoid is not adjustable. A final, small, non-water cooled solenoid is placed at the end of the beamline where the microchannel plate (MCP solenoid) is located to extend the magnetic field. The solenoids are all set to produce a magnetic field of 530 G with the scattering cell and RPA2 assemblies positioned such that the variation in the magnetic field is minimised in the region. The

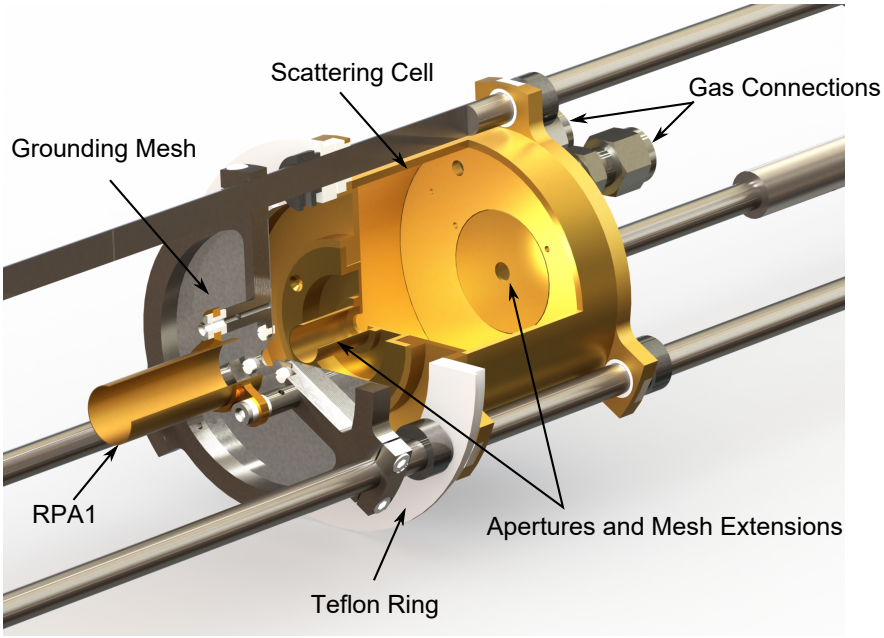

Figure 3.2.1: A typical scattering cell and RPA1 configuration.

RPA2 solenoid field is adjusted when necessary to allow for measurements of elastic and inelastic cross sections (see section 4.3.1).

Pumping is provided at end station three using the same setup as the other end stations, including a turbo pump and a mechanical backing pump.

3.2.1 The Scattering Stage

The scattering stage assembly is mounted on bars attached to end station three so that the scattering cell is located at a point where a 530 G applied axial magnetic field is approximately constant. The scattering cell configuration is shown in figure 3.2.1.

A gold-plated, copper mesh retarding potential analyser (referred to as RPA1) is located in front of the scattering cell entrance and independent potentials can be applied to both RPA1 and the scattering cell. A grounding mesh with an aperture is placed in between the RPA1 and the scattering cell to ensure there is no interaction between the RPA1 and scattering cell electric fields. Acting as retarding potential analysers, the scattering cell and RPA1 are sensitive only to $E_{\parallel}$ (the parallel energy, see section 4.1) and prevent any positron with an energy greater than qV, where V is the potential applied to the element, from passing through.

The teflon ring at the entry of the scattering cell is large enough to touch the sides of the chamber and provides some differential pumping, reducing the trap gas pressure after the scattering cell. This reduces the probability that positrons which have scattered due to the target gas undergo any secondary scattering events as they travel from the scattering cell to the detector stage.

The majority of targets studied with the AMO beamline are gases at room temperature or have a sufficiently high vapour pressure to allow measurements without significant heating. The scattering cell used for these measurements is a gold-plated, copper cylinder 45 mm in radius and 50, 100 or 200 mm in length dependent upon the specific target being studied and the required gas pressures. Two end pieces with 5 mm diameter apertures and cylindrical mesh extensions extend the electric field of the scattering cell and account for the drop in pressure at the entry and exit apertures allowing the scattering length to be assumed equal to the geometric length of the cell. There are two gas connections on the exit side of the scattering cell, one allows target gas to be admitted into the cell at a pressure controlled by a needle valve on the air side gas line. The second is connected to a MKS 630 baratron gauge (a capacitance manometer) which measures the gas pressure in the cell. It has a resolution of 10^{-6} Torr and a stated accuracy of 0.5%.

Oven

When in use, the oven replaces the scattering cell and RPA1 configuration in figure 3.2.1, and is used to study targets which are solid at room temperature. Heating these targets produces a vapour pressure which is sufficient for gas phase scattering experiments and, dependent upon the target, the oven must achieve temperatures of up to several hundred °C.

The oven, as shown in figure 3.2.2, is a copper cylinder, 100 mm in length and 30 mm in radius and heating is provided by helically wrapped twin core Thermocoax resistive wiring. A 1.4 cm^3 crucible, heated by a second Thermocoax wire, holds a powdered target sample and can be unscrewed from the oven to facilitate reloading of the target during an experimental run. The inside of the oven is lined with a fine copper mesh, preventing condensation of the target which can form significant patch potentials. Similar to the scattering cell used for gas targets, the oven has end pieces with apertures 5 mm in diameter and

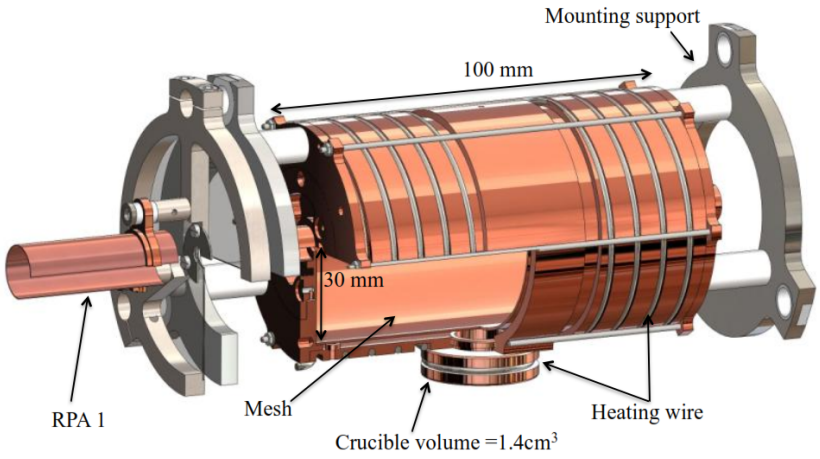

Figure 3.2.2: A schematic of the oven configuration including RPA1. The stainless steel heat shield is not shown.

copper mesh extensions. Thermal shielding is provided by a stainless steel shim wrapped around the oven. A copper RPA1 is used in the oven setup which, if necessary, can be heated using a halogen lamp to prevent condensation of the target and patch potential formation.

Solid targets used with the oven will tend to condense onto cold surfaces once they exit the heated oven. A system of cold arms and apertures (see figure 3.2.3) are employed to protect sensitive areas of the beamline such as the trap and the detection region. The vertical section of the cold arms is made from solid copper bar and is cooled using a Peltier system to subzero Celsius temperatures. A Peltier device, when a potential is applied, produces a significant temperature difference between the two sides. The temperature difference is dependent upon the potential provided and the heat sink used for the 'hot' side. The Peltiers in this experiment are clamped between two pieces of copper, with the cold side in contact with the copper cold arm feedthrough and the hot side is water cooled, allowing the cold side to reach temperatures of a few degrees below zero Celsius. The horizontal section of the cold arms is constructed from a hollow copper bar, supported by polyether ether ketone (PEEK) rings to prevent bending under their own weight, a problem which can introduce significant misalignments with the positron beam. Cold plates with 6.5 mm diameter apertures are mounted on each cold arm and located around 35 cm from the entrance and exit apertures of the scattering cell. This position should maximise condensation of target onto the cold plates while allowing the positron beam to pass through unaffected.

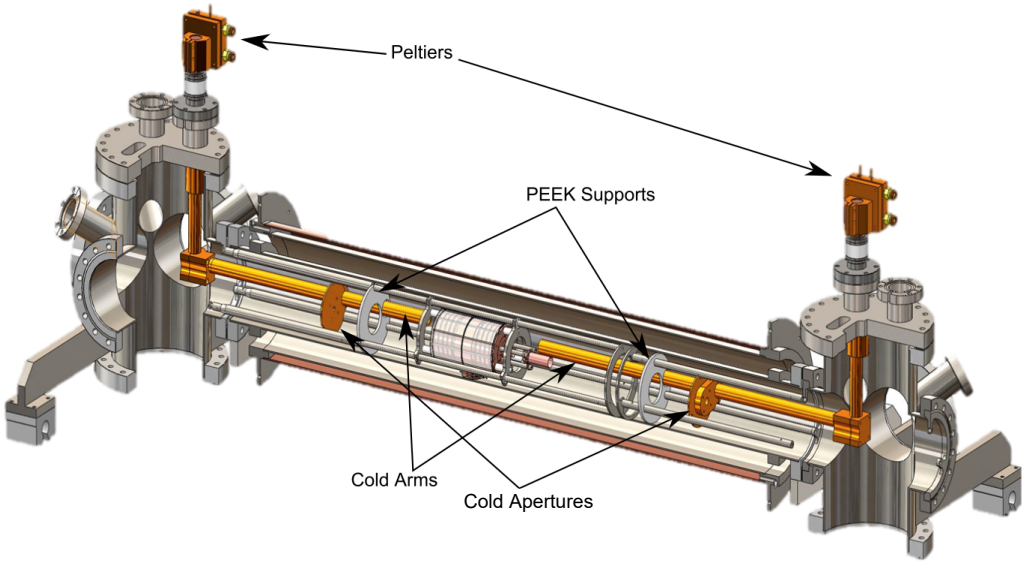

Figure 3.2.3: Schematic of the oven setup. The positron beam enters from the right, passing through a cold aperture and into the oven. The scattered beam leaves the oven, passing through a second cold aperture and travels into the detection region

The temperatures of the oven and crucible are measured by attaching resistive temperature devices (RTDs, model: Omegafilm F2010-1000-1/3B) to the surfaces of the oven and crucible using relief plates, small copper pieces with a groove which ensures good contact with the surface without compressing the RTD. A four-wire configuration is employed to reduce uncertainties due to the resistance of the wires and they are connected to a National Instruments (NI) TBX-68T isothermal terminal block. A NI 4351 high precision voltmeter provides a small current (I =25 μA) to the RTDs via the TBX-68T and the potential drop over the RTDs is monitored throughout the experiment. The potential (V) drop is simply converted to the resistance of the RTD (R_{RTD}) at the temperature (T) through $V = IR_{RTD}$, which can then be converted to find the temperature using the Callendar-Van Dusen equation (valid for $T > 0$):

$$T = \frac{2(\frac{R_{RTD}}{R_0} - 1)}{A + \sqrt{A^2 + 4B(\frac{R_{RTD}}{R_0} - 1)}} \tag{3.2.1}$$

where A and B are constants depending upon the RTD, in this case $A = 3.9080 \times 10^{-3}$ and $B = -5.8019 \times 10^{-7}$. R_0 is the resistance of the RTD at 0, equal to 1000Ω for this RTD. The temperature can be converted into a scattering

cell target gas pressure using appropriate vapour pressure curves for the target. However, it should be noted that since vapour pressure curves can often include a lot of uncertainty, for example, the oven discussed above was used in this thesis to measure total scattering cross sections for C_{60} (see chapter 7). The large differences between the vapour pressure curves from Popović et al. (1994) and Piacente et al. (1995), coupled with the measurement uncertainties, contributed significantly to the uncertainties. These uncertainties should be considered when selecting targets and when considering uncertainties in measurements.

3.2.2 The Detection Stage

The detection stage consists of a second retarding potential analyser (RPA2)- a gold plated, hollow copper cylinder, 35 mm in radius and 130 mm in length. RPA2 provides an axial electric field which allows the positron energy in the direction of the magnetic field to be determined.

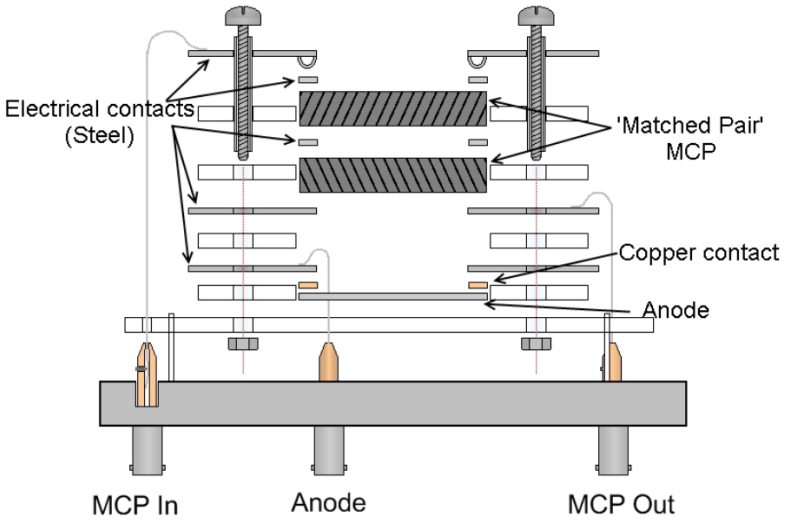

Figure 3.2.4: Exploded view of the single scattering experiment microchannel plate detector, reproduced from Jones (2010).

Positrons passing through RPA2 hit a double stack, 40 mm diameter microchannel plate (MCP) detector, shown in figure 3.2.4. A large accelerating potential is applied from the front to back plates, amplifying the signal produced by the impact of positrons by a factor of 10^7. The signal is collected from the flat, steel anode plate and passed through a simple resistor-capacitor (RC) circuit, high-pass filter which isolates the pulsed signal from the large DC potential

(around 1.5 kV) on the anode. The resultant signal is then passed through a current amplifier and recorded using a computer as a function of the RPA1, scattering cell and RPA2 applied potentials.

3.3 Positron Reaction Microscope Scattering and Detection Stages

The reaction microscope utilises the source stage for positron production and the trap and scattering cell solenoids of the beamline to confine and transport the positron beam into the reaction microscope region. A few alterations are made to the beamline configuration (see figure 3.3.1): the scattering cell and associated RPA1 are removed and replaced with RPA2 (allowing the energy of the beam to be measured before entry into the reaction microscope), the RPA2 solenoid and MCP are removed and replaced with a smaller, tuning solenoid mounted on a short chamber, to which the reaction microscope is attached. The following discussion focuses on the configuration of the reaction microscope itself.

3.3.1 Positron Beam Guidance

The reaction microscope does not currently use the trap to improve the energy resolution, however it does make use of the magnetic fields to confine and guide the beam. The magnetic fields are reduced compared to those used by the standard single scattering beamline setup, and are summarised in table 3.1. In addition to the listed coils, the beam tube gate valve coil and tuning coil at end station one are used to help guide the beam along the beamline. The position of the tuning coil between end station three and the reaction microscope can be manipulated manually and is crucial to guiding the beam through the 2 mm aperture (which defines the size of the positron beam in the interaction region) and into the reaction microscope.

3.3.2 Spectrometer and Drift Tube Regions

The spectrometer region is a key feature of the reaction microscope as it allows, through the application of extraction potentials, the separation of positive

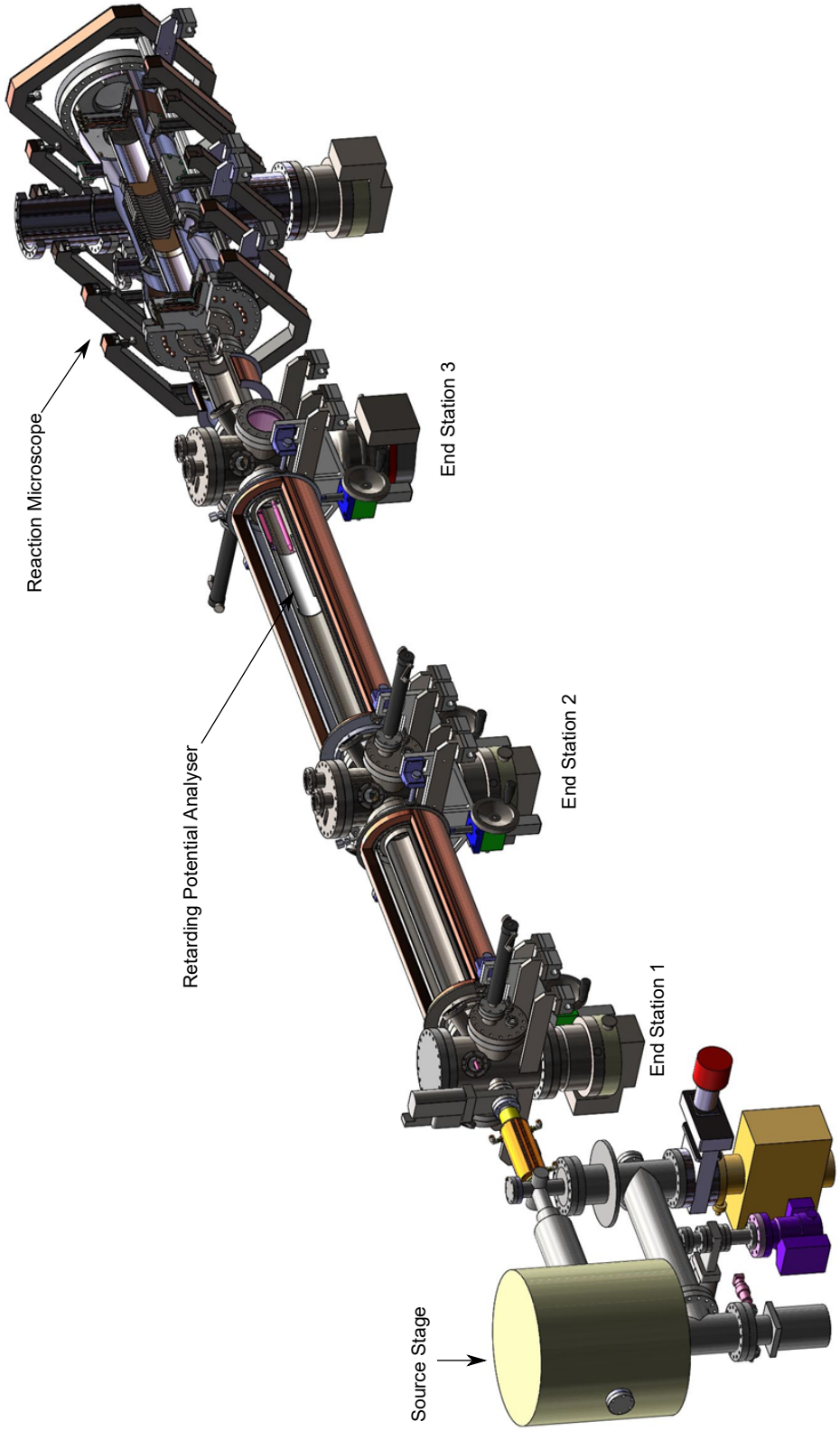

Figure 3.3.1: Schematic of the reaction microscope mounted on the beamline. The beam is magnetically guided from the source stage to the reaction microscope by the solenoids shown in brown.

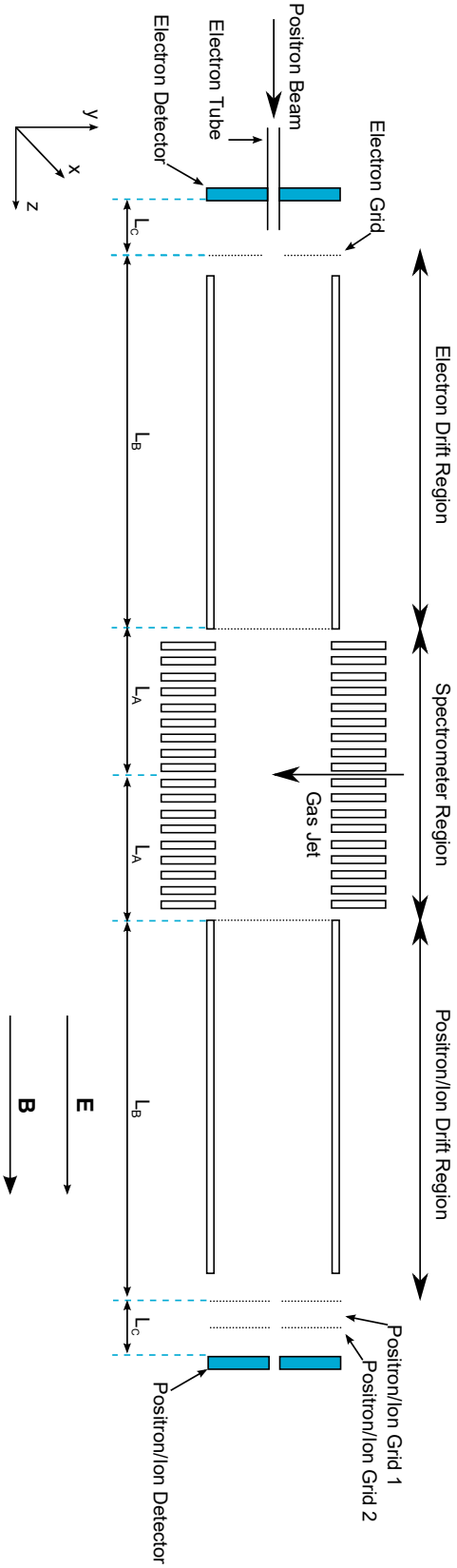

Figure 3.3.2: The reaction microscope consists of a spectrometer region, drift tubes and two detectors. The coordinate system is defined such that the centre of the experiment, where the positron beam and gas jet intersect, is $(x, y, z) = (0, 0, 0)$. The confining magnetic field and accelerating electric fields are both applied in the $+z$ direction.

Solenoid	Current (A)	Magnetic Field (G)
Helmholtz	1.1	24.2
Beam Tube	13	273
Saddle Coils	0.9	23
Trap	13	460
Scattering Cell	10	300
Reaction Microscope A and F	1	10
Reaction Microscope B and E	0.6	10
Reaction Microscope C and D	1	10

Table 3.1: Magnetic fields used for the reaction microscope

(positrons and ions) and negative (electrons) particles. Figure 3.3.2 indicates the different regions of the reaction microscope and defines the coordinate system (x, y, z). The projectile beam is guided and confined by magnetic fields applied by a series of coils (as shown in figure 3.3.1, labelled A-F starting at the entrance aperture), producing a magnetic field of 10 G, into the centre of the experiment where it interacts with an effusive gas jet. The effusive gas jet is produced by a gas needle with a regulated backing pressure and the position can be manipulated a few centimetres in the x, y and z directions. An accelerating electric field (extraction field) of 6.262 V/cm is applied across the spectrometer region, where $L_A = 10.7\ cm$. Positrons and ions are extracted in the $+z$ direction and electrons in the $-z$ direction, where they are detected by different detectors. As the particles leave the spectrometer region they enter drift tubes of length $L_B = 19.2\ cm$ where there is no further acceleration. There is another accelerating electric field over the distance L_C=1.32 cm due to the potential applied to the front of the MCP.

3.3.3 Detectors

The reaction microscope uses two time and position sensitive detectors, one for positively charged particles (the positron/ion detector) and the other for negative particles (the electron detector). The full configurations are shown in figure 3.3.3a and figure 3.3.3b. The electron detector is located at the entrance of the reaction microscope and the positron/ion detector at the far side.

Microchannel plates (MCPs), 80 mm in diameter, are located above the delay lines on both detectors. Delay lines are long wires, in this case wrapped in the

hexagonal layout shown in figure 3.3.3, that allow for position sensitive measurements of the point on the detector that a pulse was produced. Particles hitting the MCP produce an electron avalanche inside the plate which then exits as an electron cloud, colliding with the delay lines. This produces a signal which propagates from the impact point to each end of the wire, the time difference between the two time signals is proportional to the position of the initial signal. This general principle is illustrated in figure 3.3.4, given t_1 and t_2 (the time taken for the pulse to reach each end of the wire), the position coordinate x is calculated as

$$x = \frac{v_\perp}{2}(t_1 - t_2) \tag{3.3.1}$$

where $v_\perp$ is the effective propagation speed of the signal in the direction of x, given by $v_\perp = c \cdot \Delta x / l_w$ where c is the speed of light, Δx is the coordinate distance between two windings of the wire and l_w is the circumference of one winding.

Knowledge of the geometric size of the detectors and timing methods removes the requirement to know $v_\perp$ in the data analysis used with these detectors. Two-dimensional position information can be found if signals are detected on a minimum of two delay lines, this is discussed further in section 5.4.5. The delay lines used in these detectors are wires wrapped in a hexagonal configuration in three layers around an insulator where U is outermost, V is in the middle and W is innermost. This layered wrapping means that each layer has a slightly different length (figure 3.3.3c and figure 3.3.3d).

Electron Detector

The electron detector (figure 3.3.3b) is located at the entry of the reaction microscope. The beam enters the reaction microscope through a 2 mm diameter aperture, defining its size, and travels through the grounded electron tube (attached to the baseplate) which transports it through the entire electron detector.

The tube means that the delay lines must be wrapped with a gap and the MCP must have a hole in the centre to admit the positrons into the experiment. The dimensions and placement of the delay line gaps is shown in figure 3.3.5 and must be considered in the position reconstruction of electrons.

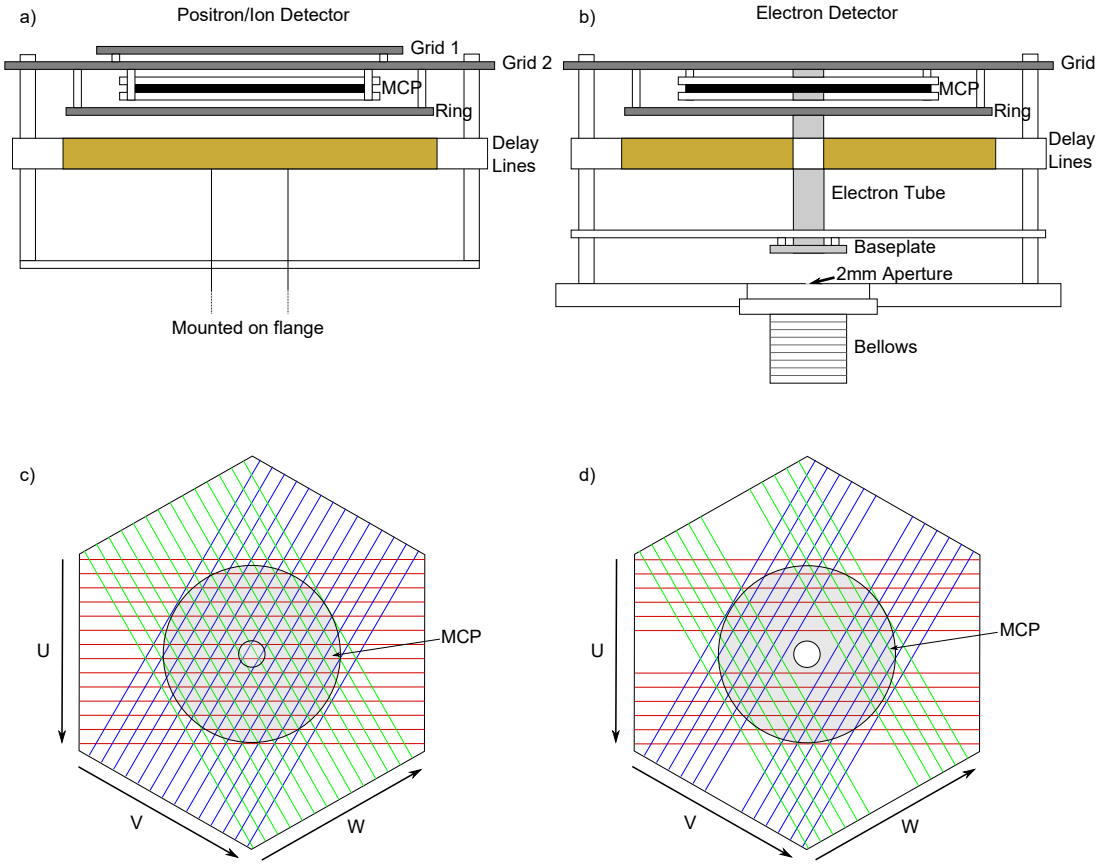

Figure 3.3.3: Schematic view of the positron/ion and electron detector configurations. The electron detector has a gap in the delay line windings to allow the electron tube to pass through the entire detector.

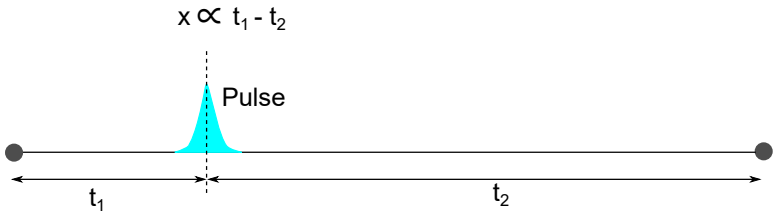

Figure 3.3.4: General principle of delay line operation. The electron cloud is shown in blue and the pulse travels to both ends of the wire.

The electron detector assembly includes a grid on top of the MCP which is typically set to the same potential as the electron drift tube in order to extend the field free region. A ring sits between the back of the MCP and the top of the delay lines, providing an extension of the electric field between the two.

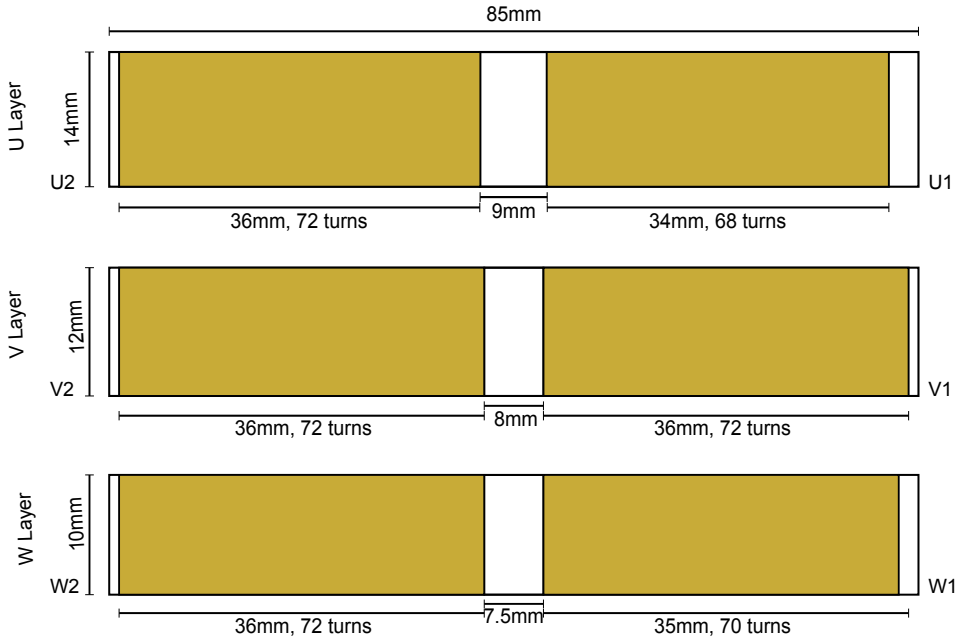

Figure 3.3.5: Side view of electron detector delay line windings including dimensions and placement of the gap in each layer

Positron/Ion Detector

The positron/ion detector MCP also has a hole in the centre, similar to the electron detector, where the unscattered positron beam can be directed. The delay lines beneath do not need a gap as if there is no MCP above (see figure 3.3.3), there will be no electron cloud and no delay line signals. If the unscattered positron beam is guided into the hole, only scattered positrons and ions can be detected, reducing the amount of unusable data collected but also rejecting positrons scattered at a sufficiently low angle.

Two grids sit in front of the positron/ion detector, grid one extends the electric field of the drift tube whereas grid two is set to a potential similar to the front of the MCP. This high potential prevents most negative particles, mostly secondary electrons, from hitting the MCP and being detected. Secondary electrons come from a range of sources, but generally are due to positrons, ions or electrons colliding with grids or other elements within the reaction microscope setup.

3.3.4 Data Acquisition

The detector potentials are applied using a pair of potential dividers with a stable, high voltage input source. As a particle hits the front MCP it produces a cascade

of secondary electrons, which are amplified and accelerated by the application of a high accelerating electric field between the front and back MCPs. The front MCP of the positron/ion detector is held at a potential of -2.85 kV, with the back MCP at ground. Conversely, the electron detector front MCP is grounded, with the back MCP at +2.65 kV. The potential divider also applies a DC potential to the delay lines. In addition to its role providing potentials to the detector, additional RC circuits within the units act as high pass filters to extract the pulses from impacting particles from the background DC potentials. These pulses make up the signals collected and further processed by the later electronics.

There are up to seven signals for each hit on a detector: an MCP signal (a pulse generated when particles hit the front of the MCP) and two signals from each delay line corresponding to the pulse at each end of the wire. For example, a hit on the U layer wire can produce two signals, U1 and U2, and likewise for layers V and W. These signals pass through a number of electronic units, including amplification, further signal processing and logic units providing signal pre-processing, before being recorded by a computer. Slight adjustments to the electronic unit setup over the two periods of data acquisition covered in this thesis, are indicated in the schematics in figure 3.3.6 (2013 setup) and figure 3.3.7 (2014 setup).

Amplification and Signal Processing

Detector signals typically have a low amplitude and therefore initially undergo amplification using a series of fast and variable gain amplifiers. The amplified signals for the MCP signal and up to six delay line pulses per detector are sent to constant fraction discriminators (CFDs) which process the raw signals into nuclear instrumentation module (NIM) standard pulses, triggering at 20 % of the pulse peak. The amplified MCP signal generated by the electron detector is inverted prior to CFD processing, as the CFDs trigger only on negative pulses. 5 ns cables are used to connect the output of the potential dividers to the Ortec 820 fast amplifiers for both detectors, 1 ns and 3 ns cables connect amplification units and CFDs for the positron/ion and electron detectors respectively.

The NIM pulses produced by the CFDs are passed along cables to the LeCroy 4616 ECL-NIM-ECL unit where they are converted into emitter-coupled logic (ECL) signals. The positron/ion detector cables are consistently 10 ns in length,

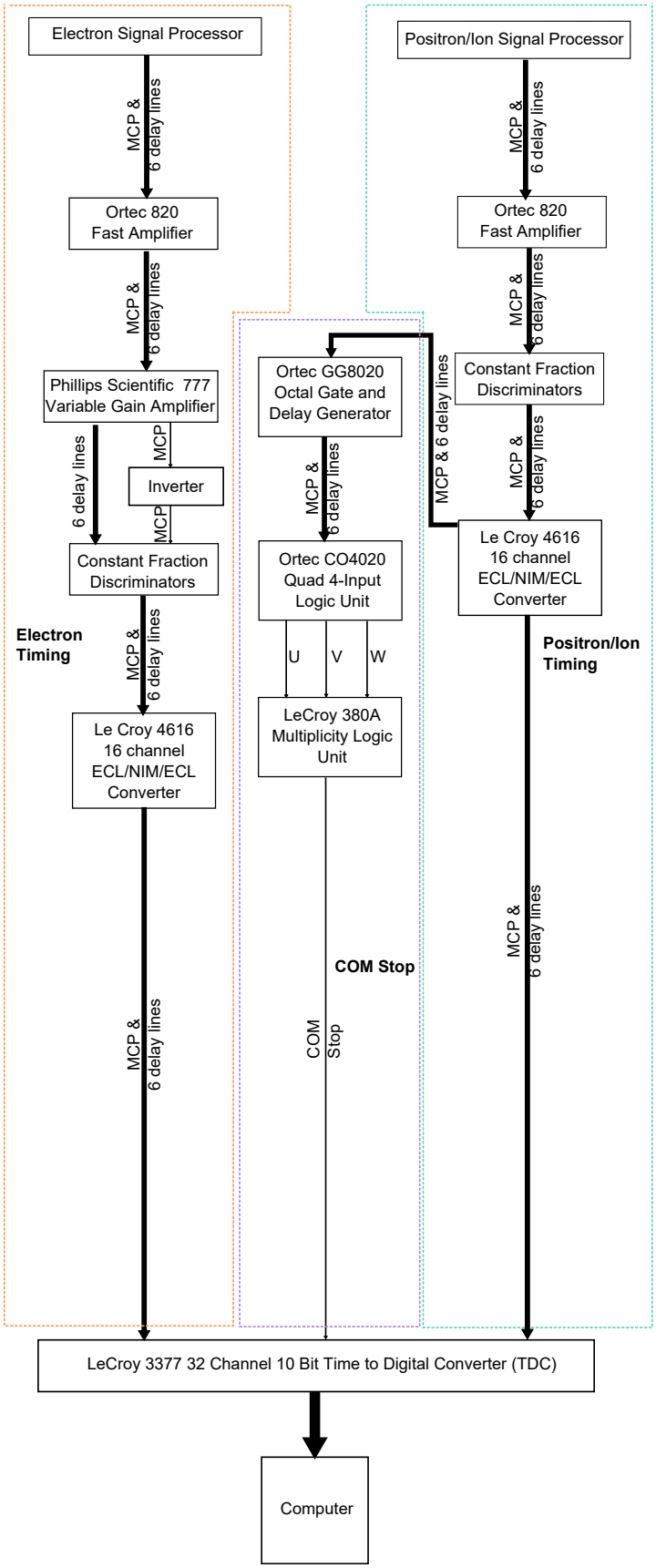

Figure 3.3.6: Electronics setup for 2013 data acquisition.

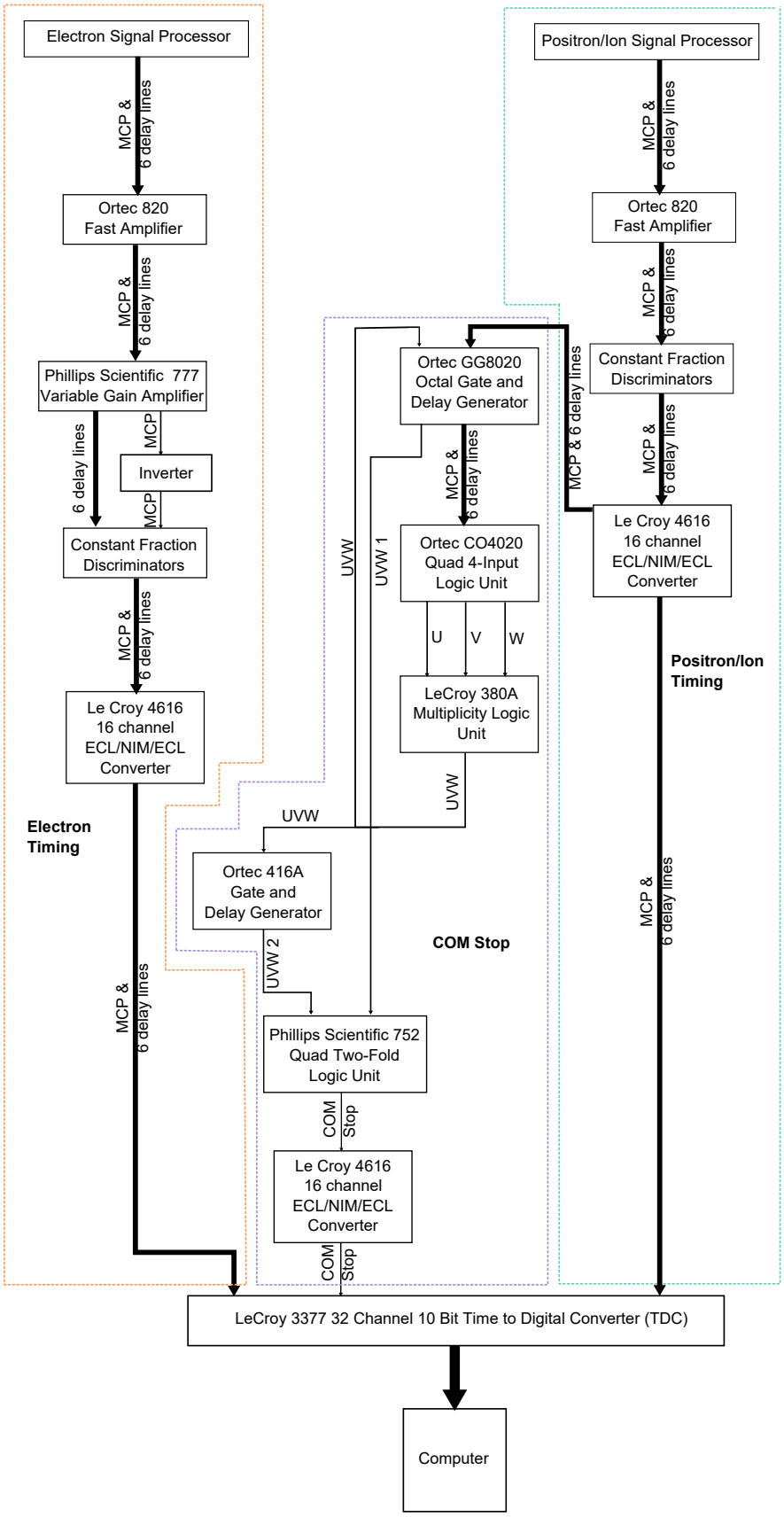

Figure 3.3.7: Electronics setup for 2014 data acquisition.

Electron Detector Signal	Cable Time Delay (ns)
MCP	16.2
U1	37.6
U2	37.6
V1	20.4
V2	18.0
W1	37.4
W2	37.2

Table 3.2: Electron detector signals and time delays due to connecting cables.

however due to positioning of the electronic logic units longer cables are used for the electron detector and these vary in length (see table 3.2). The ECL signals from the LeCroy 4616 unit are sent to the LeCroy 3377 time to digital converter (TDC) which is the final stage of data acquisition electronics, has a resolution of 500 ps and is run in double word common stop mode (COM stop). The MCP signal from the positron/ion detector is split prior to the TDC, and the undelayed signal is recorded by the TDC, whilst the other signal is delayed by 28.6 μs and forms the COM stop signal.

Signal Pre-Processing

The reaction microscope experiments tend to produce large data files, therefore it is good practice to reduce the amount of unusable data collected. Some of this can be done online, before data is recorded, using electronic logic units. At this stage good data must have

- an MCP signal
- enough position coordinates (a minimum of two complete delay lines)
- an ion candidate event (2014 only)

The position coordinates, for the positron/ion detector only, is checked by sending the MCP and delay line signals to the Ortec GG8020 unit where they are delayed by 280 ns and the pulse width is set to 255 ns. These delays and widths are selected to exceed the total time for a signal to propagate from one end of a delay line to the other, which is <110 ns dependent upon the length of the

delay line. The delayed and extended signals travel to the Ortec CO4020 logic unit where they are compared. For example, a U coordinate requires U1 and U2 signals, therefore these two signals are inputted into the same channel and an AND operation performed. This is repeated with an additional two channels for V and W, and all channels are gated with the MCP signal, since none of the data is useful unless there is an MCP signal associated with it. The Ortec CO4020 unit therefore produces three signals: U, V and W corresponding to each of the three possible coordinates. U, V and W are passed to the LeCroy 380A multiplicity logic unit which is set to N>1 i.e. there must be a minimum of two out of the three possible coordinates present. If there is enough position information, the signal from the LeCroy 380A unit (signal UVW) is delayed by 28.6 μs by an Ortec 416A unit and sent, via a second LeCroy 4616 ECL-NIM-ECL unit, to the COM stop input of the TDC.

This basic logic was used in both the 2013 and 2014 runs and ensures that hits on the positron/ion detector are only recorded if there is a reasonable chance that they will contain sufficient coordinate information for their position to be determined. In 2014 a second event on the positron/ion detector (an ion candidate) was required as well. In this setup, the UVW signal is split into two: one delayed by 28.6 μs by the Ortec 416A unit as before (UVW 1) and the other sent to the Ortec GG8020 where it is delayed by 3 μs and the width is set to 12.4 μs (UVW 2). These signals then undergo an AND operation using a Phillips Scientific 752 logic unit, if this is true the signal is passed through a second LeCroy 4616 ECL-NIM-ECL unit to the COM stop TDC input. This extra criterion means that a second hit on the positron/ion detector must occur between 13.2 and 28.6 μs after the first event, which includes the time when an Ar^+ ion is likely to arrive.

The TDC communicates with a dedicated computer where Labview code is used to set control registers, receive data and convert the data from binary into an easier to read format, saving output files with candidate data.

Chapter 4

Single Scattering Experiment Methods and Analysis

In this chapter, I will discuss the single scattering experimental techniques I used to make measurements of total scattering, positronium formation, total elastic, total inelastic and elastic differential cross sections. The apparatus itself was presented in chapter 3. The key experimental and analysis methods were previously developed by Gilbert et al. (2000), Sullivan et al. (2002) and Sullivan et al. (2008) and have been applied to this apparatus by others, for example in Jones (2010). I have applied these methods to data I collected for measurements of positron impact on argon (chapter 6) and C_{60} (chapter 7), making some modifications to improve the inclusion of background corrections or to incorporate the use of an oven in the scattering stage.

4.1 Scattering in a Magnetic Field

A charged particle moving in a magnetic field experiences a force which causes it to move in a helical motion along the magnetic field lines. The circular motion part of this helical path is due to the Lorentz force, given by

$$F = q\boldsymbol{v} \times \boldsymbol{B} \tag{4.1.1}$$

where q is the charge of the particle, $\boldsymbol{v}$ its velocity and $\boldsymbol{B}$ is the magnetic field. The helical motion means that the energy of the particle, E has both parallel ($E_{\|}$) and perpendicular ($E_{\perp}$) energy components, defined as either in the direction of or

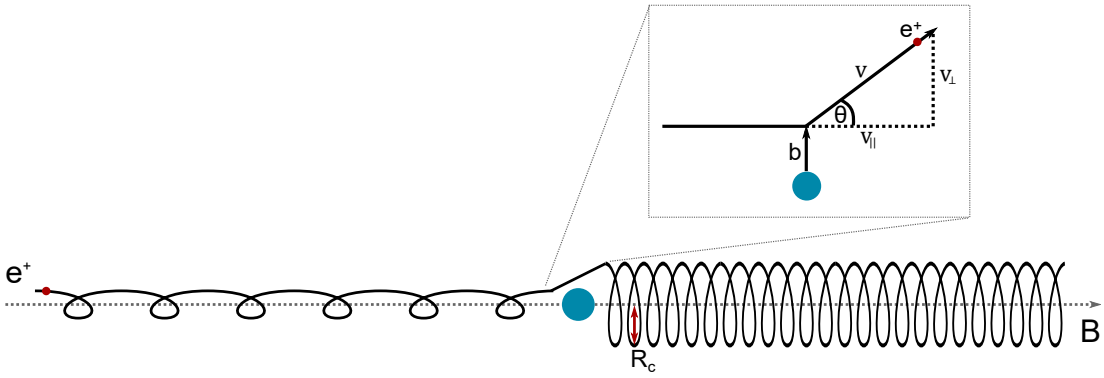

Figure 4.1.1: Schematic representation of positron motion in a magnetic field before and after elastic scattering at an angle, θ, from a target (in blue). R_c is the cyclotron radius, b is the impact parameter and $v_\parallel$ and $v_\perp$ are the parallel and perpendicular positron velocities respectively relative to the direction of the magnetic field B. Note that this diagram is not to scale.

perpendicular to the direction of the magnetic field respectively. $E_\perp$ is related to the perpendicular velocity $v_\perp$ through the kinetic energy equation $E_\perp = \frac{1}{2}mv_\perp^2$, and the cyclotron radius, r_c in figure 4.1.1, of the motion, can be calculated through the relationship

$$R_c = \frac{mv_\perp}{qB} \tag{4.1.2}$$

where m is the mass of the particle, for a positron this is the mass of an electron, m_e. Low energy positrons from the trap will have a perpendicular velocity spread of $\Delta v_\perp \sim \sqrt{2kT/m}$, where k is Boltzmann's constant and T is the temperature. At room temperature (300 K) the perpendicular energy spread is ~25 meV and in a magnetic field of 530 G, a typical field for the single scattering experiment, $R_c \sim 10\mu$m.

Figure 4.1.1 shows the motion of a positron as it approaches the target, where the cyclotron radius has been exaggerated, and scatters elastically at an angle θ converting parallel velocity into perpendicular velocity and increasing the cyclotron radius. The interaction occurs on an atomic length scale, $b \sim 1$Å which is much smaller than the cyclotron radius so the positron effectively scatters in a field-free region. After an elastic scattering event, the total energy of the positron is conserved and is given by the sum of $E_\parallel$ and $E_\perp$. The relationships between the velocity components and the scattering angle are

$$v_\parallel = v\cos\theta \tag{4.1.3}$$

$$v_\perp = v \sin\theta \tag{4.1.4}$$

where v is the initial velocity of the positron, assuming that the initial velocity of the positron is entirely parallel to the magnetic field. Given that $v = \sqrt{\frac{2E}{m}}$, the equations can be rewritten in terms of energy:

$$E_\parallel = E \cos^2\theta \tag{4.1.5}$$

$$E_\perp = E \sin^2\theta \tag{4.1.6}$$

where E is the initial energy of the positron. As the initial parallel energy of the beam is >1 eV, we can make the assumption that $E_\parallel >> E_\perp$. For a 10 eV positron beam elastically scattering at a 30° angle, the cyclotron radius in a 530 G field after the collision is $\sim$100μm, much larger than before the collision, but still small compared to the extent of the positron beam. The initial angular spread of a 10 eV beam is $\Delta\theta = \arcsin(v_\perp/v) \sim 3°$ which gives an estimate of the experimental angular resolution.

The motion of a positron changes as the magnetic field changes. The quantity $E_\perp/B$ is an adiabatic invariant and is important if the magnetic field is slowly changing. If a positron is adiabatically guided into a lower magnetic field (B_2), then its perpendicular energy component is changed by a factor, M, given by

$$M = \frac{E_{\perp 1}}{E_{\perp 2}} = \frac{B_1}{B_2} \tag{4.1.7}$$

where $E_{\perp 1}$ and $E_{\perp 2}$ are the perpendicular energy components in fields B_1 and B_2 respectively. The total energy of the positron does not change, therefore a reduction in $E_\perp$ corresponds to an increase in $E_\parallel$.

4.2 Experimental and Analysis Methods

4.2.1 Beam Production: Moderator Growth

Moderators (see also section 3.1.1) decay over time due to contaminants freezing onto the moderator surface, reducing the beam intensity. This necessitates regular

moderator regrowth which can be done either automatically using source control software or manually. Moderator condition and growth is monitored through a γ-counter positioned at the end of the beam tube, where there is a gate valve. When the beam tube gate valve is closed, moderated positrons annihilate upon impact with the gate valve and the 511 keV γ-rays are detected by the scintillator. A contaminated moderator is indicated by a steady decrease in the number of γ counts i.e. a decrease in the number of moderated positrons reaching the beam tube gate valve. The decision to regrow moderators is made taking into account the experimental downtime due to regrowth and the decrease in beam intensity. The regrowth interval is typically from 1 to 3 days depending upon the cleanliness of the source stage vacuum.

Preparation for the growth of a new moderator begins with the complete removal of the old moderator. The cryogenic coldhead is turned off, allowing the source stage temperature to typically rise to $\sim$ 20 K, such that the frozen neon evaporates. The evaporated neon gas is pumped out of the system by the source stage turbo pump. Once the pressure in the source stage has dropped to $< 1 \times 10^{-6}$ Torr, the coldhead is turned on again, reducing the source stage temperature to 7-8.5 K.

The moderator is grown in two stages, as shown in figure 4.2.1, using the system discussed in section 3.1.1 and the procedure is optimised to decrease grow time and maximise moderated positron beam intensity. During the first stage the turbo gate valve is closed, such that the source stage is no longer pumped. Ultra-high purity neon gas is admitted until the pressure as measured at the PID located close to the needle valve is stabilised at around 1×10^{-4} Torr, although the neon pressure downstream around the moderator cone is much higher. The neon freezes onto the moderator cone and the γ-counts measured at the beam tube gate valve increases as the moderator is formed. The grow time is typically 1000 s which is sufficient for the γ-count rate to plateau, this indicates that additional grow time may produce a thicker moderator but will not increase the positron beam intensity. During the second stage, the neon inlet is closed and the turbo gate valve reopened, removing excess gas. The measured count rate increases during this time as positron scattering from the neon gas, in particular, loss through positronium formation, is reduced. Once growth is complete, the moderator is maintained at a low temperature (7-8.5 K) and the beam tube gate valve is opened to allow the moderated positrons to pass into the trap stage.

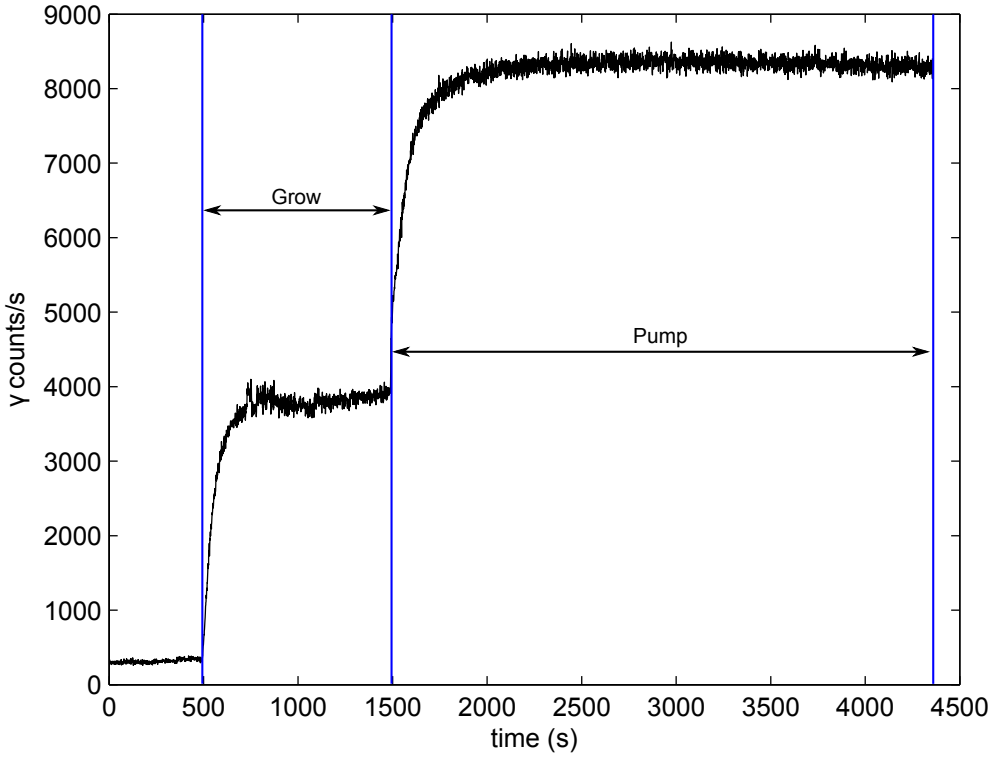

Figure 4.2.1: A typical moderator growth showing the grow phase, where neon is frozen onto the surface of the moderator cone, and the pump phase where excess gas is removed from the source chamber.

4.2.2 Beam Production: The Trap Cycle

The trap significantly improves the beam's energy spread, typically achieving FWHM energy spreads of ∼40-60 meV. The trap stage makes use of the buffer gases, nitrogen (N_2) and tetrafluromethane (CF_4), to trap and cool the positrons before ejecting them an energy up to 200 eV. The trap cycle consists of three stages: load, cool and dump, where the potentials for each stage are depicted in figure 4.2.2. It is important to note that the trap is constantly loading positrons during the cool and dump phases, improving the trap efficiency, and the cycle rate is usually around 50-70 Hz (i.e. there are 50-70 trap cycles every second).

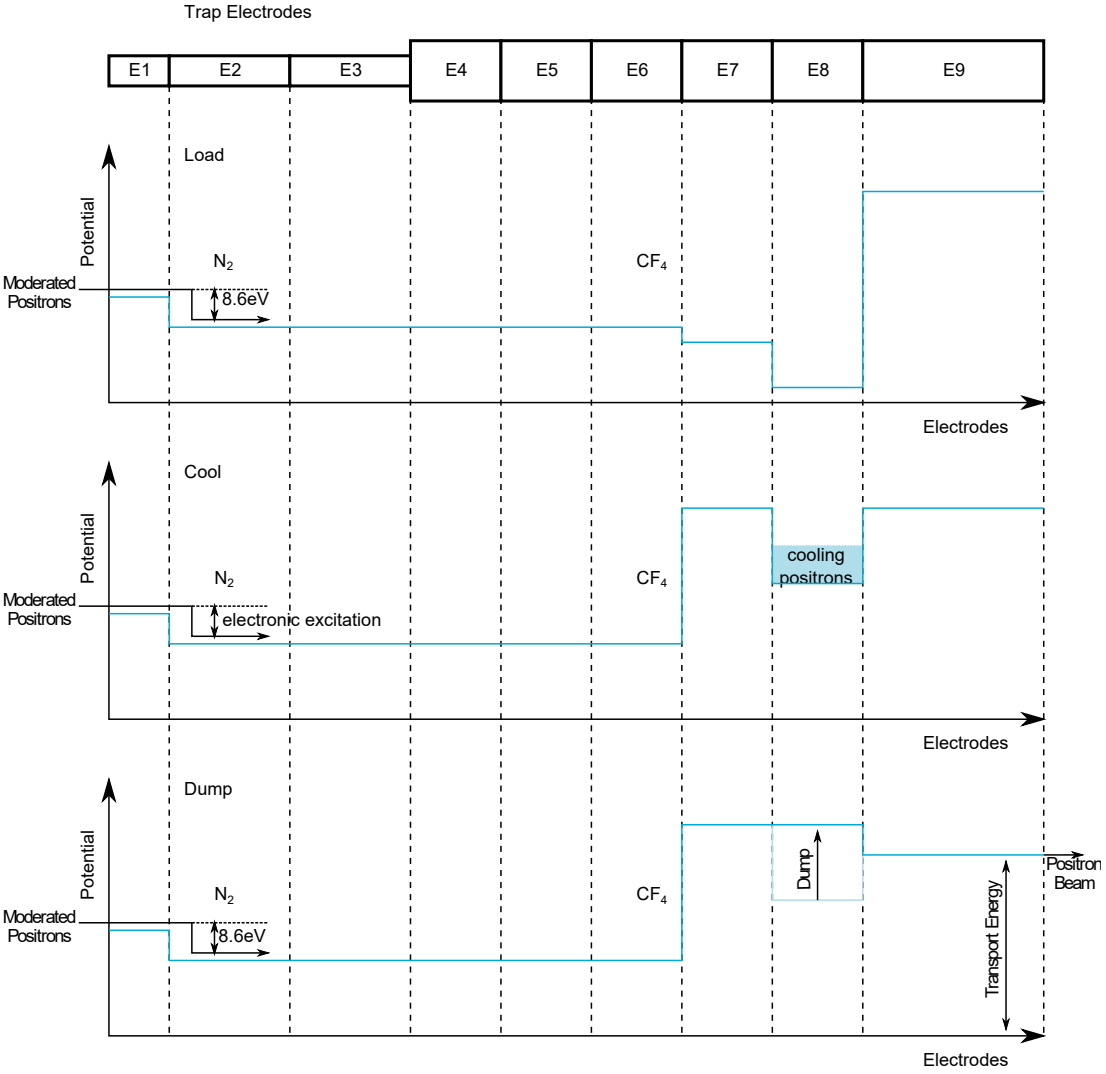

Figure 4.2.2: Trap cycle showing load, cool and dump stages. Electrodes are numbered E1-E9

Load

Loading is the longest phase, typically lasting 10-15 ms. The first electrode potential must be low enough to admit the moderated positron beam, which has an energy defined by the moderator bias. This is not trivial as the change in magnetic field from 88 G in the source stage to 530 G in the trap stage affects the distribution of the positron energy into the parallel ($E_{\parallel}$) and perpendicular ($E_{\perp}$) energy components. The moderated positron beam typically has $\Delta E_{\parallel} \sim 1.5 - 2\ eV$ FWHM in source stage, but this is increased fivefold in the trap stage as $M \approx 5$ (a detailed explanation of parallel and perpedicular energies, and their significance to the experiment is give in section 4.1). Therefore, the first electrode is set to ~ 7 V below the moderated beam energy allowing the majority of moderated positrons to enter the trap. Some positrons are lost at this point as the energy spread is asymmetric, demonstrated in Jones (2010).

The positrons are trapped through electronic excitation of the buffer gas, N_2. N_2 is unusual as the electronic excitation of the $a^1\Pi$ state has a threshold of 8.59 eV, lower than the positronium (Ps) formation threshold at 8.78 eV (Marler and Surko (2005a)). Ps formation results in a loss of positron beam intensity as it is not confined by the magnetic field and drifts off the beam axis and self-annihilates. To some extent, loss of positrons through through this process is inevitable. However, it can be mitigated by tuning the positron-N_2 impact energy, using the difference between the moderator potential and electrodes two and three, to ~ 10 eV. At this energy the electronic excitation cross section is significantly larger than the Ps formation cross section (see figure 4.2.3) and trapping efficiency is maximised.

The N_2 pressure is set so that positrons are trapped during a single transit of the trap. Gas is admitted at electrode two and stepped potentials on later electrodes allow the positrons to become trapped through the same collision process in areas where the buffer gas pressure is lower, reducing annihilation. Some collisions with CF_4 also occur in this region as the two buffer gases mix. Annihilation due to collision with trap gases is another loss process that must be considered carefully, although the cross section is several orders of magnitude lower than the other scattering cross sections. Annihilation of trapped positrons is minimised by ensuring that they do not spend an excessive amount of time in the trap.

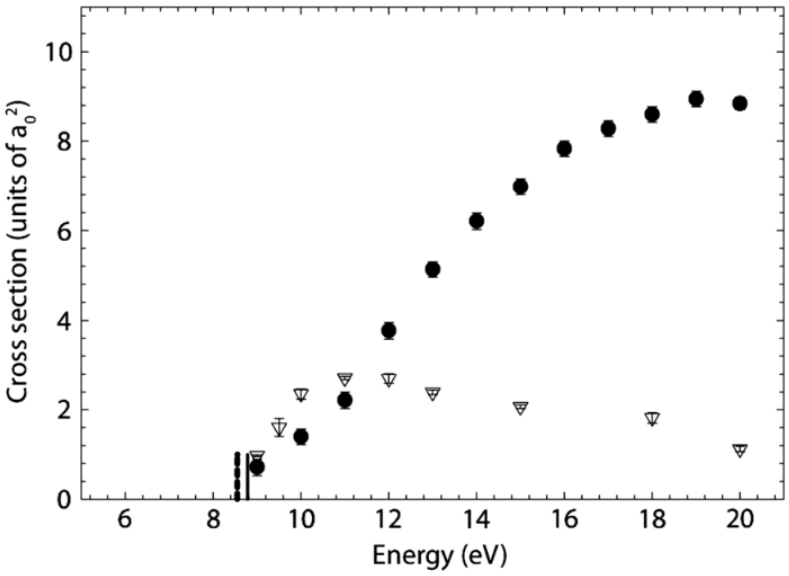

Figure 4.2.3: Energy dependence for N_2 electronic excitation and Ps formation cross sections, reproduced from Danielson and Dubin (2015). ▽ electronic excitation, original data from Sullivan et al. (2001b) and • Ps formation, original data from Marler and Surko (2005a).

Cool

During the cooling phase, the electrode seven potential is raised to prevent loading of more positrons into the final section of the trap, as shown in figure 4.2.2. The potential on electrode eight is also raised as this will affect the dump stage, discussed later. The positrons are thus trapped in the potential well formed between electrodes seven and nine and undergo collisions with N_2 and CF_4. Vibrational and rotational excitation of N_2 plays an important role in cooling the positrons at this stage, but CF_4 is much more efficient. A comparison of the scattering cross sections in figure 4.2.4, indicates that CF_4 has a significantly larger vibrational excitation cross section than N_2, especially for the antisymmetric ν_3 stretch mode. As the energy loss for each vibration is similar, CF_4 could be expected to cool positrons ∼100 times faster than N_2. Cooling positrons quickly is important to reduce annihilation in the trap. Positrons typically cool for 2-3 ms in this stage until they have reached room temperature, with an energy $E = 3/2kT \sim 40\, meV$, corresponding to $E_{\parallel} \sim 25\ meV$.

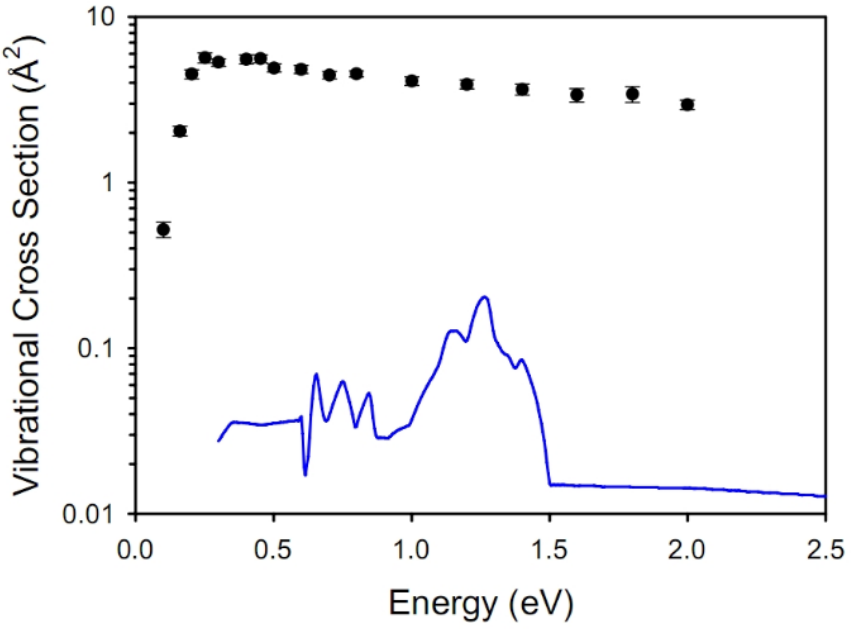

Figure 4.2.4: Comparison of N_2 and CF_4 vibrational cross sections. • ν_3 anti-symmetric stretch mode of CF_4, measured by Marler and Surko (2005b). — Close coupling calculation of the integral N_2 vibrational cross section from Gianturco and Mukherjee (1997). Diagram reproduced from Jones (2010).

Dump

The dump phase is relatively short, taking around 0.5 ms, and consists of raising the electrode eight potential as a function of time as shown in figure 4.2.5. Positrons are ejected from the trap in a pulse with a beam energy defined by the potential applied to electrode nine, often referred to as the transport energy. The speed at which the electrode eight potential is increased affects the temporal and energy resolution of the beam, where the energy resolution is of greater importance in the single scattering experiments. If the potential is increased too rapidly it can result in unintentional heating of the beam, degrading the energy resolution. The final result of this cycle is a pulsed beam with thousands of positrons per pulse.

In addition to the loss processes already discussed, cross field transport due to misalignment of the trap solenoid with the trap electrodes, or scattering from the buffer gases can further reduce the trap efficiency. Cross field transport causes the positrons to hit the electrodes and annihilate and can, to some extent, be reduced by aligning the trap solenoid for maximum beam intensity. When

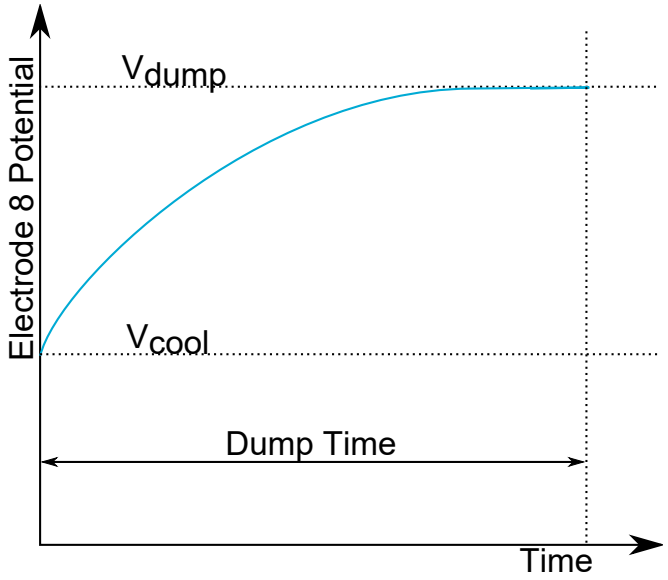

Figure 4.2.5: The typical change in voltage of electrode eight as a function of time is logarithmic, rising from V_{cool}, the electrode eight potential during the cool phase, to V_{dump}, the final electrode eight potential in the dump phase, over a specified dump time.

positrons scatter from the buffer gases, they do not necessarily remain on-axis making them susceptible to cross-field transport. However, since the presence of buffer gases is essential for operation, cross field transport due to scattering is impossible to remove completely. The overall efficiency of the trap is ∼10%, based on measurements made by Jones (2010). Loss of positron intensity is mostly due to

- Ps formation
- Cross field transport
- Transfer of energy from $E_{\parallel}$ to $E_{\perp}$ due to magnetic field changes moving from the source stage to the trap

4.2.3 Pulse Characterisation

Characterisation of the pulse is necessary for optimisation of the trap settings and to provide appropriate settings for potentials for data collection. It is possible to monitor the beam intensity, its energy and energy resolution as well as its temporal resolution.

Beam Intensity

The beam intensity corresponds to the number of moderated positrons passing from the trap into the scattering cell. It can be measured two different ways: beam flags or with the MCP detector.

Beam flags are copper plates which can be manually moved into the beam path. Positrons annihilate on the plates producing a current, measured using a current preamplifier which produces a time-averaged pulse current with an accuracy of a few femtoamps. When measured at end station two, after the trap, typical currents are ∼10 to 50fA with a much higher peak current depending upon the trap settings. Generally, the further the beam flag is from the source, the lower the measured current as positrons are lost in the trap and on their passage through the scattering cell. However, these measurements can be useful for optimisation of settings and diagnostic purposes as they provide an absolute measurement of the beam intensity.

During experiments, the intensity is measured using the MCP which provides a more reliable measure of the relative intensity of pulses, although it is not easily directly linked to an absolute current.

Beam Energy and Spread

The beam energy and energy spread are two of the most important features of the pulse and are determined using a retarding potential analyser, as described in section 3.2. The beam transport energy is set by the potential of trap electrode nine, whereas the beam energy in the scattering cell is determined by the potential applied to the cell. The beam energy and spread are measured by raising the potential of RPA1, the scattering cell and RPA2 and recording the beam intensity at the MCP. These measurements lead to the characteristic dependency shown in the cutoff curve in figure 4.2.6. Fitting a Gaussian curve to the differentiated cutoff curve, provides measures of the cutoff potential, which corresponds to the beam transport energy and is determined by the potential at which 50% of the beam is blocked, and the full width half maximum (FWHM), which corresponds to the energy spread.

During operation, the cutoff curves for each element (RPA1, scattering cell and RPA2) are determined to allow for individualised potential settings during

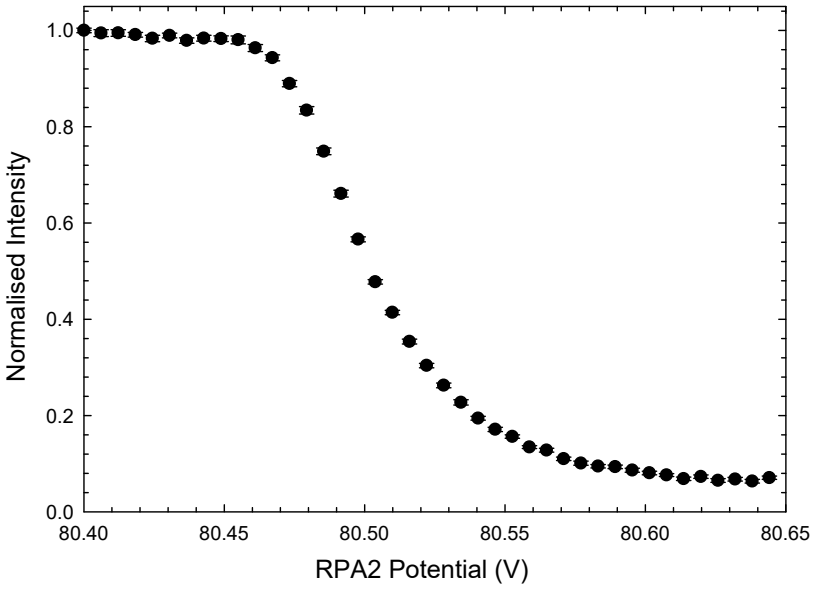

(a) RPA cutoff curve

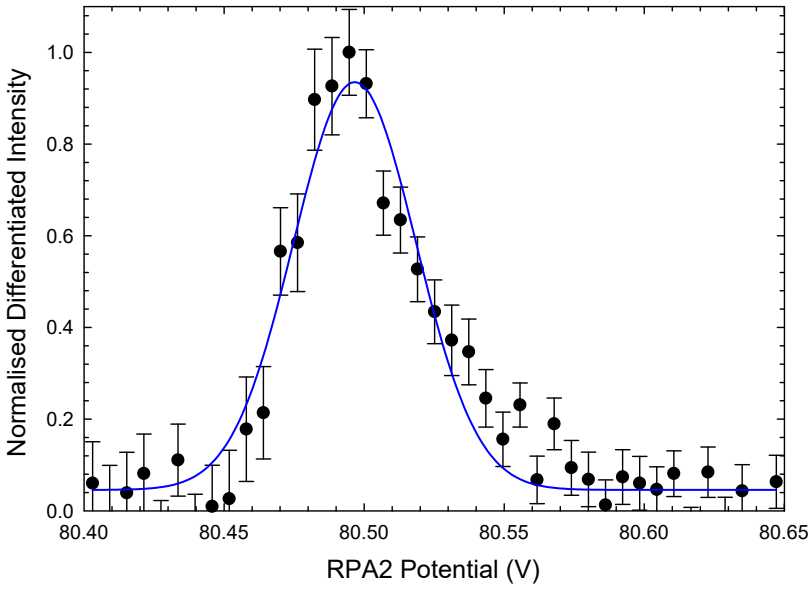

(b) Differentiated cutoff curve

Figure 4.2.6: An example RPA cutoff curve. Figure 4.2.6a is the normalised data collected as the RPA potential is scanned whereas in figure 4.2.6b this data has been differentiated, the peak normalised to 1 and a Gaussian fit is plotted. The cutoff potential here is determined to be 80.50±0.001 V, with a FWHM of 52±3 mV.

data collection. Since each element is controlled by separate amplifier channels, with several different electrical connections which leads to small contact potential offsets, the cutoff potentials can vary by typically a few hundred mV.

Temporal Resolution

The temporal resolution is less important in the current measurements, although minimising the time width of the pulse ensures that background counts collected during a pulse measurement are negligible. The temporal resolution can be determined through analysis of the pulse shape as measured by the MCP and associated electronics and, depending upon the trap settings, is typically around 1-5 μs in width.

4.3 Scattering Cross Sections in a Magnetic Field

Total Scattering Cross Section

The total scattering cross section, σ_T, is defined as the ratio of the number of specific outcome 'events' per unit time, per unit scatterer, to the relative flux of the incident particles with respect to the target (see section 2.1). In the single scattering experiment it can be measured using the Beer-Lambert law (from work by Lambert (1760) and Beer (1852), modern versions, for example from Ingle and Crouch (1988)),

$$\sigma_T = -\frac{1}{nl} \ln\left(\frac{I_T}{I_0}\right) \tag{4.3.1}$$

where I_0 is the full incident intensity, I_T is the unscattered, transmitted intensity after passing through the target, n is the target number density and l is the scattering path length. This law applies to a 'thick' target, in this case the scattering cell.

If the diameter of the scattering cell apertures is much smaller than the internal diameter of the scattering cell, the gas pressure drops off sharply at the edges, with a small pressure drop inside the cell close to the apertures which is compensated for by a non-zero pressure just outside the cell. If the energy is the

same inside the cell and just outside the cell, in this case achieved through the extension meshes, these pressures cancel each other out, meaning that we can assume a pressure step function at the aperture, and thus l can be taken as the geometric length of the cell. To accurately determine n it is necessary to ensure these pressure measurements are taken at a point which is unaffected by these pressure drops.

In the single scattering experiments described here, the total cross section, σ_T, can be partitioned into the contributing cross sections such that

$$\sigma_T = \sigma_{Ps} + \sigma_{el} + \sigma_{inel} \tag{4.3.2}$$

where σ_{Ps}, σ_{el} and σ_{inel} are the Ps formation, total elastic and total inelastic cross sections. σ_{inel} includes all available inelastic processes (such as electronic excitation and ionisation). In the case of scattering from molecules, σ_{el} includes contributions from any vibrational and rotational excitations at the scattering energy due to the energy resolution limitations of this experiment. In practical terms, the partial cross sections are calculated as a fraction of the total:

$$\begin{aligned} \sigma_{Ps} &= R_{Ps}\sigma_T, \\ \sigma_{el} &= R_{el}\sigma_T, \\ \sigma_{inel} &= R_{inel}\sigma_T \end{aligned} \tag{4.3.3}$$

where R represents the fraction of σ_T contributed by the specific channels.

Elastic Differential Cross Sections

The differential cross section (DCS) gives the angular dependence of σ_{el} at the scattering energy. The derivation of the equation, presented below, is adapted from Gilbert et al. (2000) and Sullivan et al. (2002) and applies to elastic DCS in a magnetic field.

If the target pressure is low enough that single scattering events is the only possibility, the DCS can be written as

$$\begin{aligned}\sigma_{DCS}(\theta) &= -\frac{1}{nl} I_s^{e^+}/I_0^{e^+} \\ &= -\frac{1}{nl}\frac{dI(E_\parallel)}{d\Omega} \\ &= -\frac{1}{nl}\frac{dE_\parallel}{d\Omega}\frac{dI(E_\parallel)}{dE_\parallel}\end{aligned} \tag{4.3.4}$$

where the scattered intensity, $I_s^{e^+}$, is related to the energy distribution of the transmitted intensity as a function of the solid angle Ω, $dI(E_\parallel)/d\Omega$, expanded into $dI(E_\parallel)/dE_\parallel$ and $dE_\parallel/d\Omega$. The constant of proportionality $1/nl$ allows the measurement of absolute cross sections and the full incident intensity, $I_0^{e^+}$, is equal to I_0 in equation 4.3.1 and normalised such that $I_0^{e^+} = 1$. The solid angle is related to the angles θ and ϕ, defined in figure 2.1.1. DCS measurements in this experiment are summed over all azimuthal angles (ϕ). Equation 4.3.4 can thus be rewritten as

$$\sigma_{DCS}(\theta) = -\frac{1}{2\pi nl\sin\theta}\frac{dE_\parallel}{d\theta}\frac{dI(E_\parallel)}{dE_\parallel} \tag{4.3.5}$$

The angular dependence of $E_\parallel$ is given by equation 4.1.5, differentiating and simplifying this gives

$$\frac{dE_\parallel}{d\theta} = 2E\sin\theta\cos\theta = 2\sqrt{EE_\parallel}\sin\theta \tag{4.3.6}$$

Combining equations 4.3.4, 4.3.5 and 4.3.6, the DCS is

$$\sigma_{DCS}(\theta) = -\frac{\sqrt{EE_\parallel}}{\pi nl}\frac{dI(E_\parallel)}{dE_\parallel} \tag{4.3.7}$$

4.3.1 Cross Section Measurements and Analysis

Total and Partial Cross Sections

The intensity measurements necessary for calculation of σ_T, and determination of the partial cross sections, given by equations 4.3.1, 4.3.2 and 4.3.3, are shown in figure 4.3.1. The scattering energy, E, of the positrons is defined by the difference

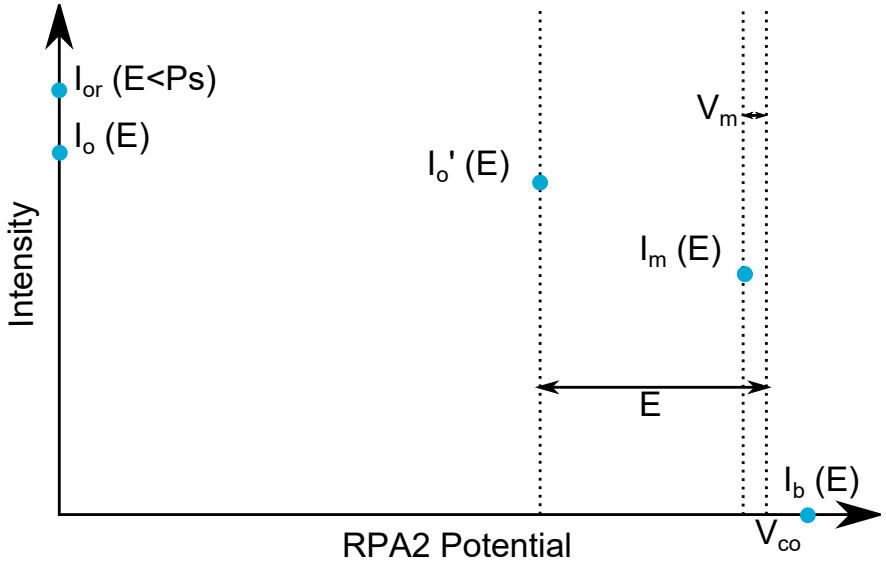

Figure 4.3.1: Intensity measurement points for total scattering and Ps formation cross sections. V_{co} is the RPA2 cutoff potential and E is the positron impact energy.

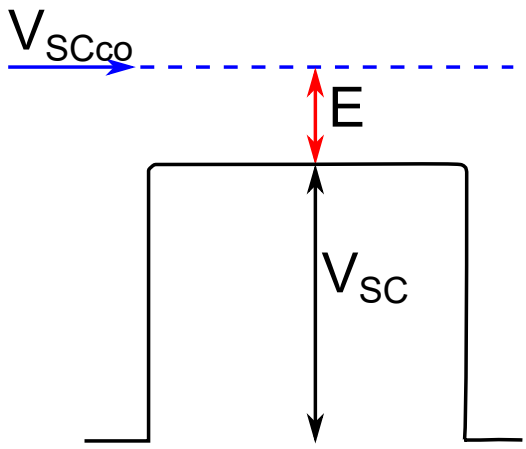

Figure 4.3.2: Positron scattering energy, E, as set by the scattering cell. The cutoff potential V_{SCco} corresponds to the beam energy, positrons lose energy equivalent to qV_{SC} as they pass over the potential wall produced by the scattering cell potential resulting in a scattering energy of $E = qV_{SCco} - qV_{SC}$.

between the scattering cell cutoff potential, V_{SCco}, and the potential applied to the scattering cell, V_{SC} as shown in figure 4.3.2.

The full incident intensity, referred to as I_0 in equation 4.3.1, is given by I_{or} as shown in figure 4.3.1 and is taken with gas in the cell. RPA2 is set to 0 V such that all positrons, regardless of their energy, are transmitted through the RPA2 section. Positronium will decay in flight via self-annihilation, so Ps formation manifests as a loss in the beam intensity. Therefore, I_{or} is taken with the scattering energy below the Ps formation threshold of the gas target. This measurement is made with gas in the cell as the point is measured at the beginning of every scan, allowing for an accurate determination of the full incident intensity which accounts for any degradation in beam intensity due to moderator decay.

Due to the energy resolution of the positron beam it is not possible to determine the true unscattered, transmitted intensity, I_T, in equation 4.3.1 as this corresponds to a measurement at the cutoff point of the positron beam. As demonstrated by the cutoff curves, the positron beam intensity begins to decrease before the cutoff potential, even in the absence of a target gas due to the finite energy width of the positron beam. Therefore, at scattering angles close to the cutoff potential, scattering at small angles is indistinguishable from the drop in intensity due to the energy resolution of the beam. The energy spread of the beam defines the angular resolution of the experiment, where the smallest angle that can be measured, the minimum angle, θ_m, is given by

$$\theta_m = \sin^{-}1\left(\sqrt{\frac{eV_m}{E}}\right) \tag{4.3.8}$$

where e is the charge of an electron and V_m is an RPA2 potential offset. Appropriate values of V_m are selected with reference to the RPA2 cutoff curve and correspond to a potential where there is no decrease in the positron intensity due to the energy spread of the beam, typically <100 meV. The transmitted intensity, I_m, is measured at the scattering energy of interest and at an RPA2 potential given by $V_{RPA2co} - V_m$, where V_{RPA2co} is the cutoff potential for the RPA2 curve.

Given the values of n and l determined from the pressure and geometric length of the scattering cell respectively, the total cross section is calculated using

$$\sigma_T = -\frac{1}{nl}\ln\left(\frac{I_m}{I_{or}}\right) \tag{4.3.9}$$

which is an underestimation of the true total scattering cross section due to the minimum angle defined by the scattering energy and energy spread of the beam.

In order to extract partial cross sections from σ_T, additional intensity measurements are made as shown in figure 4.3.1. The Ps formation cross section requires the measurement of the point I_o, taken at the scattering energy of interest, with an RPA2 potential of 0 V such that positrons with all parallel energies can be detected. The change in positron intensity between I_o and I_{or} is related to the Ps formation cross section by

$$\sigma_{Ps} = R_{Ps}\sigma_T = \frac{I_{or} - I_o}{I_{or} - I_m}\sigma_T \tag{4.3.10}$$

If the scattering energy is below the Ps formation cross section then $I_{or} = I_o$ and $\sigma_{Ps} = 0$ Å^2.

I'_o is always taken at the scattering energy and if M is 1, the RPA2 potential is given by $V_{RPA2co} - E/q$ corresponding to scattering at an angle of 90°. Any difference between I_o and I'_o is indicative of scattering from background gases and will tend to increase the total cross section, and if necessary this difference is used to determine a correction for background scattering, as described in section 4.4.

Measurements of σ_{el} are often made with $M > 1$ and measuring σ_{inel} requires $M > 1$, in order to distinguish the two contributions. Figure 4.3.3 shows two curves, where the blue curve represents the positron intensity as a function of RPA2 potential at $M = 1$, with the red curve corresponding to $M > 1$. The scattering energy, E, in this figure is greater than the first inelastic threshold, thus inelastic and elastic scattering are present.

When $M = 1$, the difference between I'_o and I_m includes scattering due to inelastic and elastic processes and it is not possible to separate the contributions. However, if $M > 1$, the magnetic field in the RPA2 region is decreased meaning that some of the perpendicular energy of elastically scattered positrons (due to angular scattering) is transferred into parallel energy as per equation 4.1.7. The total energy of the elastically scattered positron is maintained, but this transfer between energy components results in an 'compression' of the elastic scattering into a smaller energy region as represented by the red curve. Therefore, I'_o is taken at the scattering energy with an RPA2 potential of $V_{co,RPA2} - E/M$.

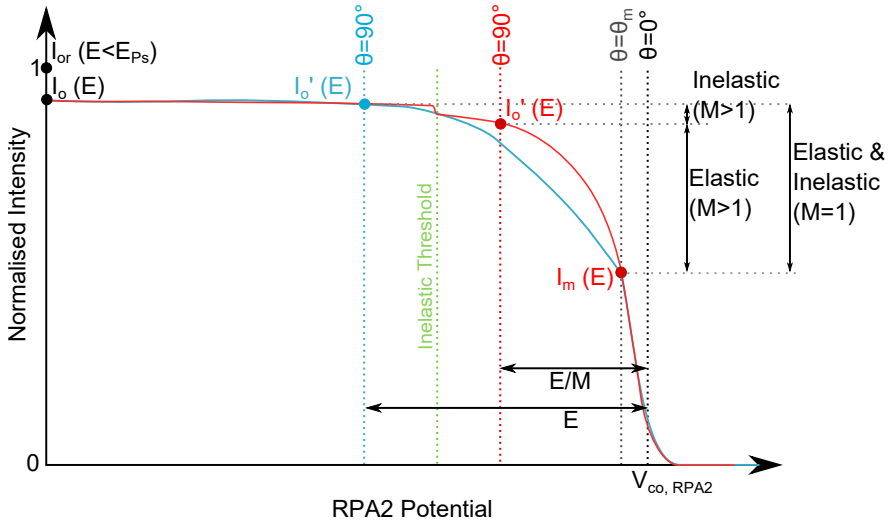

Figure 4.3.3: Intensity measurement points. — $M = 1$; — $M > 1$. $V_{co,RPA2}$ is the RPA2 cutoff potential and E is the positron impact energy.

Separation of the elastic and inelastic scattering requires M to be greater than E/E_{thresh}, where E_{thresh} is the energy of the first inelastic threshold. The total elastic cross section is then given by

$$\sigma_{el} = R_{el}\sigma_T = \frac{I'_o - I_m}{I_{or} - I_m}\sigma_T \tag{4.3.11}$$

As reducing the magnetic field in the RPA2 region does not impact the inelastic thresholds, once the elastic scattering has been compressed the difference between I_o and I'_o corresponds to the inelastic portion. The total inelastic cross section is given by

$$\sigma_{inel} = R_{inel}\sigma_T = \frac{I_o - I'_o}{I_{or} - I_m}\sigma_T \tag{4.3.12}$$

Elastic Differential Cross Sections

Elastic differential cross sections (DCS) are calculated using equation 4.3.7. This requires measurement of the scattering cell pressure to determine n and knowledge of the geometric length of the scattering cell in order to find l. A more challenging element is the measurement of $dI(E_\parallel)/dE_\parallel$.

As previously discussed, measurements are made at points I_{or}, I_o and I'_o (shown in figure 4.3.3). These measurements allow the normalisation of the DCS

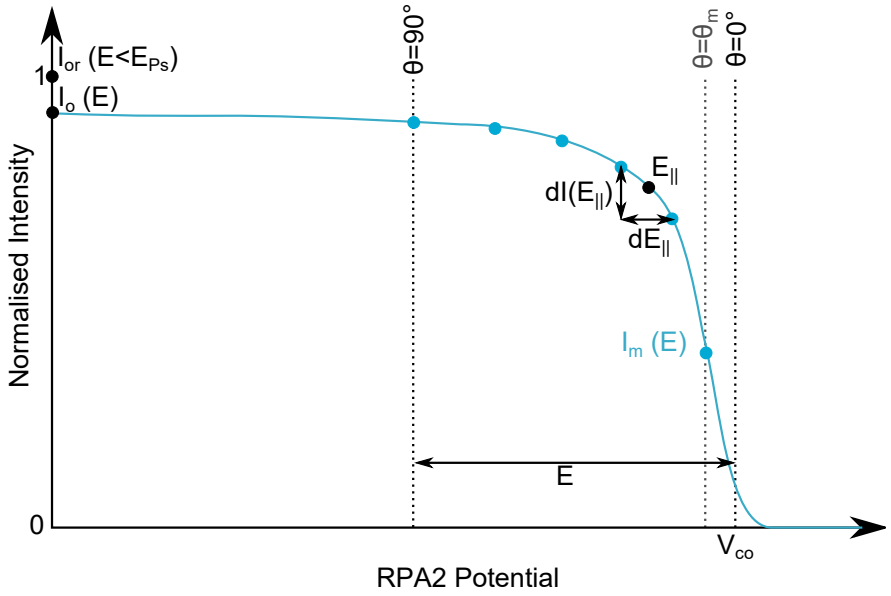

Figure 4.3.4: Intensity measurement points for elastic differential cross sections. V_{co} is the RPA2 cutoff potential and E is the positron impact energy.

and the calculation of σ_{Ps}, as well as providing a useful check for systematic effects during measurements.

Figure 4.3.4 indicates the multiple DCS intensity measurements made between RPA2 potentials $V_{RPA2co} - E/eM$ (corresponding to point I'_o) and V_{RPA2co}. Each of these points is related to a scattering angle where the positron parallel energy can be determine using equation 4.1.5. Typically, DCS are calculated for every 5° multiple, and to achieve this measurements are taken at the appropriate parallel energies.

$dI(E_\parallel)/dE_\parallel$ is calculated using each of the intensity measurements corresponding to angles θ =0-90°. The measured intensities $I\theta_1$ and $I\theta_2$ are related to scattering angles θ_1 and θ_2 respectively, such that the desired scattering angle $\theta = \frac{\theta_1+\theta_2}{2}$. These points are taken at potentials V_{θ_1} and V_{θ_2}, corresponding to the relevant parallel energies. The differential is then given by

$$dI(E_\parallel)/dE_\parallel = (I\theta_1 - I\theta_2)/(E_\parallel\theta_1 - E_\parallel\theta_2) \tag{4.3.13}$$

Finally, $E_\parallel$ is calculated from the midpoint between $V_(\theta_1)$ and $V_(\theta_2)$ and all values are substituted into equation 4.3.7.

All DCS measured using these techniques are 'folded' around 90°. Backwards scattered positrons are scattered at an angle θ between 90 and 180° and initially

travel away from the detector. They are reflected by the RPA1 potential and travel back through the scattering cell at an angle of $180-\theta$ before impacting the detector. Therefore, positrons scattered at angles of θ and $180-\theta$ are indistinguishable and are summed together in the final measurements. As the scattering percentage is low in the scattering cell, it is assumed that backscattered positrons do not undergo multiple scattering events on their second transit through the cell.

If the scattering energy is below the first inelastic threshold for the target then $M = 1$, but when the scattering energy is above this threshold $M > 1$ in order to separate the elastic portion of scattering. The use of $M > 1$ negatively impacts upon the minimum DCS angle that can be determined and the angular resolution, due to the compression of the elastic scattering curve and the finite energy resolution of the beam. Any angular measurements impacted by the RPA2 cutoff curve decrease close to the cutoff potential are discarded, giving the minimum angle. The angular resolution, $\delta\theta$, is dependent upon the scattering energy and energy spread of the beam δE and is given by

$$\delta\theta = \frac{\delta E}{2\sqrt{EE\| - E\|^2}} \tag{4.3.14}$$

4.3.2 Target Gas Pressure

Multiple scattering events are when scattered positrons undergo further scattering events before detection. If a positron undergoes multiple scattering events then, for example, the detected scattered angle is not the same as the angle at which it first scattered. It can lead to a small underestimation of the total cross section, but can have a significant effect on the shape of the measured DCS.

In order to decrease the probability of multiple scattering events, the target gas pressure is set so that fewer than 10% of positrons scatter during their transit of the scattering cell. If the target is a gas or a liquid with a high vapour pressure at room temperature, the target pressure is controlled using a needle valve. The percentage of positrons scattered is measured by taking the full incident intensity, $I_o r$ and the transmitted intensity at I_m. 10% scattering is equivalent to a ratio of 0.9 between these two measurements and the gas pressure can be adjusted until this criterion is met. The same procedure is followed when the oven is used, except that the temperature of the oven is gradually increased until a ratio of 0.9 between the full incident and transmitted positron intensities is achieved.

4.4 Corrections

Corrections to the measured scattering cross sections are made due to a range of systematic issues, these are summarised in table 4.1 below and discussed in further detail in this section.

Correction	**Description**
Moderator Decay	Due to a gradual reduction in the moderator efficiency over time, short scans are made over a few minutes and measurements are normalised to the I_{or} for each scan.
Background Corrections	Scattering outside the cell from non-target gases is accounted for by taking measurements without target gas in the scattering cell as well as measurement of the points I_o and I'_o where no positron intensity change would be expected. This is generally a contribution of $\sim 1\%$.
Baratron Drift	Variations in the zero point of the baratron are accounted for by taking pre and post scan measurements with no target gas in the scattering cell. This is most of the overall $\sim 3\%$ uncertainty in cross sections.
Thermal Transpiration	A temperature differential between the baratron and scattering cell results in an overmeasurement of the true pressure in the cell. Thermal transpiration corrections are made using either Knudsen (1910) or Takaishi and Sensui (1963), corrections are usually $\sim 3\%$ of the pressure measured.
Missing Angle	The energy spread of the positron beam means that it is not possible to distinguish between the positron beam and scattering at angles close to $0°$. When reliable theoretical DCS are available, the 'missing' portion of the total cross section can be added to the measured total scattering cross section.

Table 4.1: A summary of the corrections made when measuring scattering cross sections.

4.4.1 Moderator Decay

Moderator efficiency tends to decrease over time as the moderators 'decay' and the number of extracted positrons reduces (see figure 4.4.1). To account for this, measurements are made in short scans over a time scale of a few minutes, during

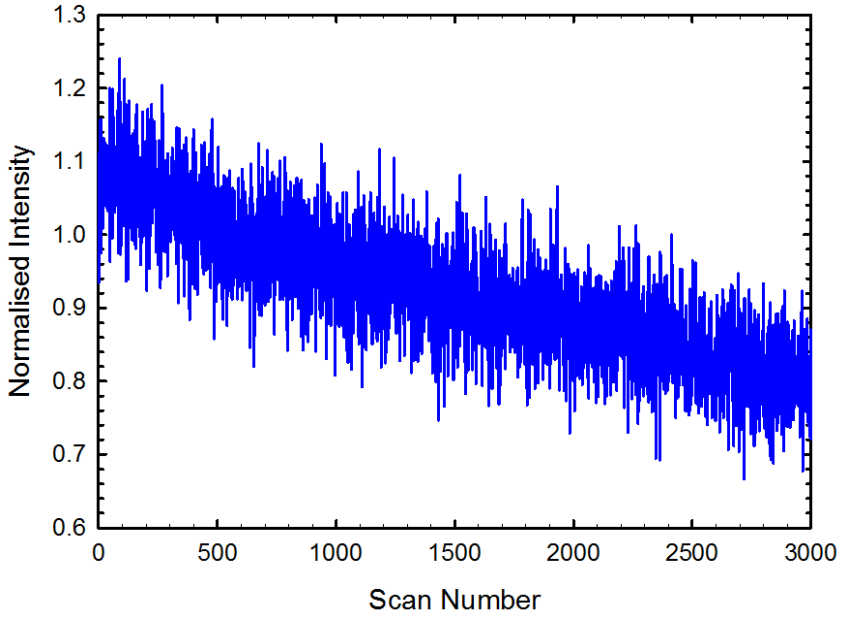

Figure 4.4.1: Example of moderator decay (seen in the I_{or} point) over the course of a run, normalised to the intensity in the first scan. Each scan takes approximately 1 minute depending upon the number of measurements taken, this data set corresponds to around 2 days of measurements.

which moderator decay is negligible. A full data set typically contains thousands of these short scans, and corresponds to a time period of hours to days. As moderator decay is significant over this longer time scale, all measurements are normalised to the I_{or} measurement for each of the short scans.

4.4.2 Background Corrections

Total Scattering and Partial Cross Sections

Background scattering refers to any scattering outside the scattering cell, due to the presence of background gases (most likely N_2 from the trap) or from target gas diffusing from the scattering cell apertures. This scattering can occur at several points in the system beyond the trap. Typically around 10% of positrons leaving the trap scatter due to trap buffer gases which have diffused from the trap exit. As scattering events result in a reduction of the positron's parallel energy, these scattered positrons are rejected by RPA1 which significantly reduces the background scattering issues.

However, additional background scattering may occur between the end of RPA1 and the detector, with the majority of this around the scattering cell itself. In order to account for this scattering a number of provisions are made including measurements of

- the target gas out scattering cell intensity-potential curve
- the target gas out RPA2 intensity-potential curve
- I_o and I'_o during target gas in experiments

The target gas out scattering cell and RPA2 intensity-potential curves involve scanning the respective potentials of each element and recording the positron intensity at the detector. This gives a clear view of background scattering due to non-target gases in the experiment. Figure 4.4.2 shows an example intensity-potential curve taken with no target gas in the scattering cell. If there was no background scattering, the normalised intensity would be 1 at all potentials until it approached the cutoff potential. However, as shown in the figure, the reality is that the background shows a gradual decrease in intensity across the potential range indicating background scattering which is usually less than 1%. Corrections for the scattering cell and RPA2 are calculated, I_d in the figure, and are added to the measured intensities with target gas present to account for this additional attenuation.

As discussed previously, during total cross section points I_o and I'_o are measured. Ideally, the difference between these intensities would be zero as I'_o is taken at the scattering energy and any scattering between these two points would correspond to scattering at energies higher than the energy of interest. Generally, there is a small difference (typically $\leq 1\%$) between these intensities which persists after the target gas out background corrections have been applied. This suggests that additional background scattering occurs due to target gas diffusing from the scattering cell. To account for this extra scattering, the total cross sections measurements are reduced.

Elastic Differential Cross Sections

Background scattering can occur for DCS measurements, but the corrections are simplified as each DCS measurement corresponds to a single scattering energy.

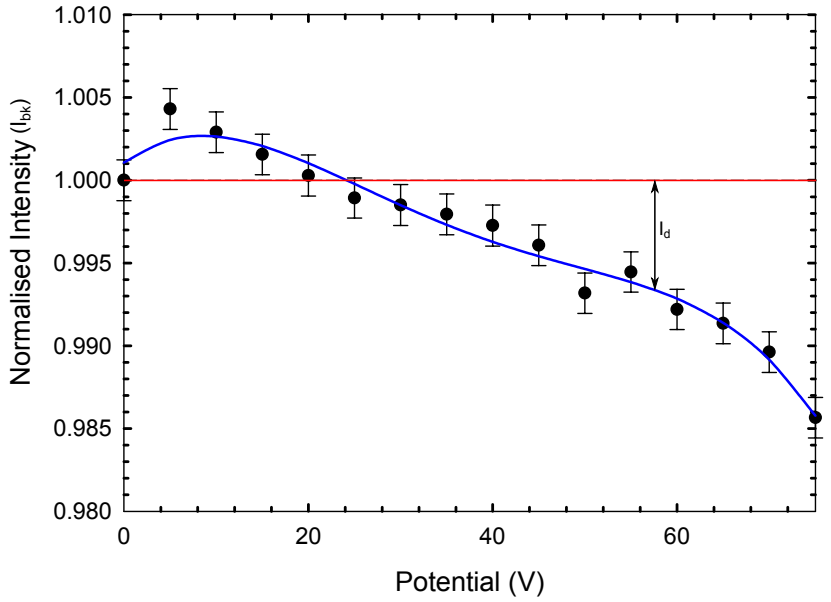

Figure 4.4.2: Example of a background correction measurement showing a polynomial fit to the normalised data.

Measurements are taken at the same scattering cell and RPA2 potentials as used in a DCS scan with no target gas in the cell. As above, ideally there would be no scattering of positrons when the target gas is present, but this is generally not the reality. Intensity corrections, I_d, are calculated as shown in figure 4.4.2 and applied to each measurement point in the DCS.

4.4.3 Pressure

Accurate pressure measurements allow for the determination of absolute scattering cross sections. The pressure is measured using a baratron and corrections to the pressure arise from baratron drift, the gradual change in the baratron's zero level, and thermal transpiration.

Baratron Drift

Baratron drift is the gradual change in the zero point of the baratron itself, if this is not accounted for it introduces a systematic over or under estimation of the true pressure. To reduce the drift, the baratron itself is surrounded by an insulated protective box during measurements to prevent sudden changes in temperature

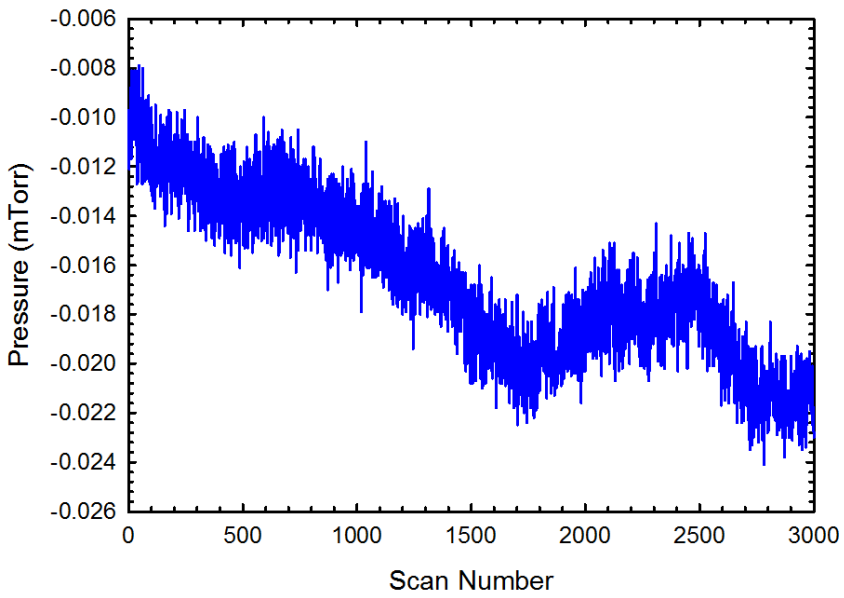

Figure 4.4.3: Example of baratron drift over one full run, taken from a background measurement to remove the contribution from varying target gas pressure

or knocks. Figure 4.4.3 indicates a typical variation of the 'baratron zero' across throughout a day, recorded with no target gas in the system. During experiments it is not possible to directly monitor the baratron drift.

In order to account for the systematic baratron drift effect an initial baratron zero measurement is recorded, B_i, before target gas is admitted to the system and a final baratron zero, B_f, is made after the experimental measurements once the target gas has been removed. The average of B_i and B_f is the baratron zero, B_0, is used to adjust the measured pressure p to give the true pressure, p' using

$$p' = p - B_0 \tag{4.4.1}$$

Uncertainties in the pressure measurement are estimated from the difference between B_i and B_f. The baratron drift can introduce one of the largest uncertainties in an experiment, for example, in the argon measurements presented in chapter 6 the baratron drift accounts for most of the estimated ~3% uncertainty.

Thermal Transpiration

The baratron head is held at a constant temperature of 45°C, which reduces the temperature coefficient of the span and zero coefficients, allowing for greater

stability and accuracy of measurements. It is connected to the scattering cell, which is at a lower temperature of 27°C(300 K), by tubing with a 4.6 mm internal diameter, d. The low pressures and temperature difference between the baratron and cell means there is a pressure differential which leads to an overmeasurement of the true pressure in the cell. When measurements of the cell pressure are made with the baratron (such as those in chapter 6), corrections for thermal transpiration are required.

If the pressure in the system is low enough that the mean free path of the molecules is much less than d, a simple thermal transpiration correction (Knudsen, 1910) may be used

$$p_{cell} = p_{baratron}\sqrt{\frac{T_{cell}}{T_{baratron}}} \tag{4.4.2}$$

where T_{cell}, $T_{baratron}$ are the temperatures of the scattering cell and baratron in Kelvin respectively, $p_{baratron}$ is the pressure measured by the baratron and p_{cell} is the true pressure inside the cell. This is valid only if $T_{baratron} > T_{cell}$ and results in a pressure correction of ∼3% for the current system, assuming $T_{baratron}$=318 K and T_{cell}=300 K.

If the pressure is very high, then there is no pressure differential. However, in between these two regions, which applies to this experiment, the ratio $p_{cell}/p_{baratron}$ will range between these two extremes. An empirical equation for thermal transpiration in this region was developed by Liang (1953) and a modified form, was produced by Takaishi and Sensui (1963). It is used, when all empirical variables are known, in these experiments to fully correct the pressures (such as those in chapter 6). If the variables are not known, then equation 4.4.2 provides a reasonable estimate of the correction.

The empirical relationship between p_{cell} and $p_{baratron}$ is given by

$$p_{cell} = p_{baratron} \cdot \left(\frac{AX^2 + BX + C\sqrt{X} + 1}{AX^2 + BX + C\sqrt{X} + \sqrt{T_{baratron}/T_{cell}}} \right) \tag{4.4.3}$$

where

$$
\begin{aligned}
A &= A^* \left(T^*\right)^{-2} \\
B &= B^* \left(T^*\right)^{-1} \\
C &= C^* \left(T^*\right)^{-0.5} \\
T^* &= 0.5 \left(T_{cell} + T_{baratron}\right)^{-2} \\
X &= 0.133 p_{baratron} d
\end{aligned} \tag{4.4.4}
$$

where A^*, B^*, C^* are reduced constants where the temperature dependence has been removed. These are available for a small selection of gases studied by Takaishi and Sensui, from this data they propose that the reduced constants can be calculated from the molecular diameter, D, of a gas. The reduced constants are thus

$$
\begin{aligned}
A^* &= 1.4 \times 10^4 \exp\left(1.17 \times 10^{10}\right) \\
B^* &= 5.6 \exp\left(1.40 \times 10^{10}\right) \\
C^* &= \left(1.10 \times 10^{-8}/D\right)
\end{aligned} \tag{4.4.5}
$$

when the molecular diameter is not available in literature, it can be calculated from viscosity data using kinetic theory where

$$
\eta = \frac{5}{16D^2} \left(\frac{mkT}{\pi}\right)^{1/2} \tag{4.4.6}
$$

where η is the viscosity, m is the molecular mass, k is Boltzmann's constant and T the temperature.

4.4.4 Missing Angle

If reliable theoretical DCS are available for the target, corrections can be made to σ_T and σ_{el} in order to account for the underestimation due to the angular resolution of the beam (see Sullivan et al. (2011)). The measured σ_{el} is equivalent to the integral of the DCS between $\theta_m{}^\circ$ and $180 - \theta_m{}^\circ$ as the data is 'folded' about 90°. The 'missing' part of σ_{el} is estimated by integrating between these angles

and comparing this with the integration of the DCS from 0-180°. Correction of σ_{el} in turn corrects σ_T. If the DCS for the specific target and energy is very forward peaked, this correction can be very significant (>10%).

Chapter 5

The Reaction Microscope Methods and Analysis

The reaction microscope is designed to study ionisation in triple coincidence to extract triply differential cross sections, as defined in section 2.1. The apparatus was detailed in section 3.3. In this chapter, I will discuss the operational procedures I developed alongside Simon Armitage and Dennis Mueller of the University of North Texas to study the single ionisation of atoms by positron impact. I will also describe the post-processing analysis code I created, based upon the electron reaction microscope work discussed in Dürr (2006) and Senftleben (2009), which I adapted for our experimental setup and use of positrons. My contribution to the code handled the raw data, determining events which would be considered 'good', performing corrections and calculating Cartesian position coordinates for each particle (see sections 5.4.1 to 5.4.5). The final momentum reconstruction method was developed by Dennis Mueller and Eric Knudsen, also of the University of North Texas, as detailed in section 5.4.6. I applied this analysis code to data I collected from the reaction microscope for positron-argon single ionisation during 2013 and 2014, the results of this are presented in chapter 8.

5.1 Introduction

The positron reaction microscope is designed to investigate positron induced ionisation of atoms and molecules by measuring fully differential cross sections. So far, it has been used to study single ionisation of argon (Ar) atoms in triple coincidence, where the ion, scattered positron and ejected electron are detected using

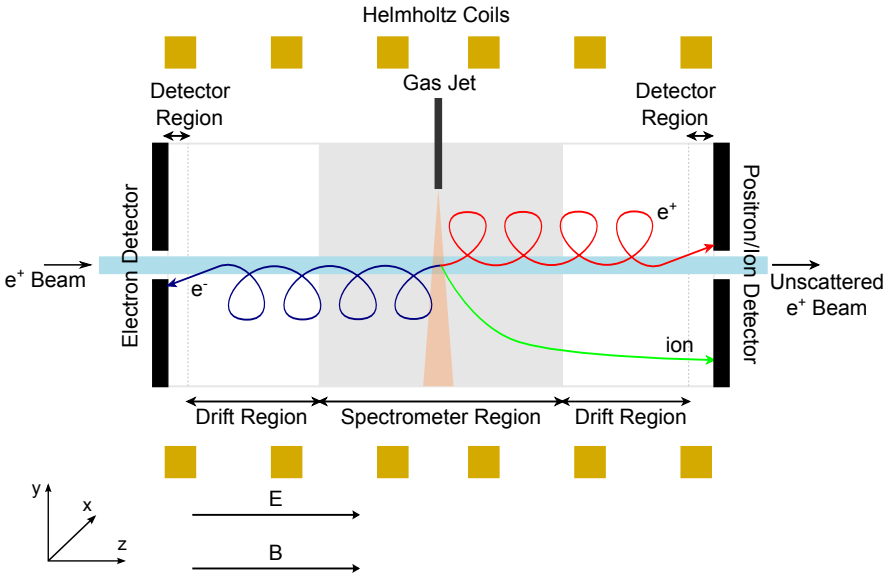

Figure 5.1.1: The general concept of reaction microscope operation showing the paths of particles following an ionisation event

position sensitive detectors with the goal of determining the longitudinal, $\boldsymbol{p}_z$, and transverse, $\boldsymbol{p}_r$, momentum vectors.

The operation concept of the reaction microscope is depicted in figure 5.1.1. Ionisation occurs at the approximate centre of the experiment where the continuous positron beam and effusive gas jet intersect. Following a single ionisation event, the particles are extracted from the interaction region using an extraction field- an accelerating electric field which accelerates the positive particles in the $+z$ direction, towards the positron/ion detector, and the negative particles in the $-z$ direction towards the electron detector. On their transit through the experiment, the particles pass through a drift tube, where there is no acceleration, and finally hit the detectors giving a detection point (x, y). For a continuous positron beam, it is not possible to measure the time of flight for each of the particles individually. Therefore, the times of flight for the ion and electron are determined relative to the arrival time of the positron at the positron/ion detector, where

$$\begin{aligned} t_{e^+ion} &= t_{ion} - t_{e^+} \\ t_{e^+e^-} &= t_{e^-} - t_{e^+} \end{aligned} \tag{5.1.1}$$

where t_{e^+}, t_{e^-}, t_{ion} are the times of flight for the positron, electron and ion respectively, and t_{e^+ion} and $t_{e^+e^-}$ are the positron-ion and positron-electron relative

times of flight. These measurements can then be used to calculate the longitudinal and transverse momenta.

Longitudinal Momentum

The longitudinal momentum is related to the time of flight for the particle and the potentials applied across the experiment for the extraction field and in the detector regions. Figure 3.3.2, in section 3.3, shows the three main regions of interest: the spectrometer region, the drift tube region of length L_B and the detector region. In the spectrometer region an accelerating electric field or extraction field, E_{ex}, is applied across a distance L_A. Due to the potential applied to the front of the MCP, there is an additional accelerating electric field in the detector region, over the distance L_C, from the end of the drift tube to the front of the MCP.

After ionisation, a particle with mass, m, and charge, q, has an initial longitudinal momentum $\boldsymbol{p}_z$. In the spectrometer region (region A) it experiences an acceleration, a_A:

$$a_A = \frac{q}{m} \cdot E_{ex} \tag{5.1.2}$$

Note that due to the product qE_{ex}, for a positron or ion with initial longitudinal momentum in the $+z$ direction, or an electron with initial longitudinal momentum in the $-z$ direction, the product qE_{ex} is always positive, extracting the particle away from the interaction region. The time of flight for the particle in region A, t_A, is thus given by

$$t_A = \frac{2L_A}{\sqrt{v_z^2 + 2a_A L_A} \pm v_z} = \frac{2mL_A}{\sqrt{p_z^2 + 2qmU_A} \pm p_z} \tag{5.1.3}$$

where $v_z = p_z/m$ is the initial longitudinal velocity and $U_A = E_{ex}L_A$ is the potential applied at the end of the spectrometer region, the same potential applied to the drift tube. The $\pm$ in the denominator refers to the direction the particle is accelerated in and is positive for positrons and ions and negative for electrons. In the drift tube region (region B), there is no further acceleration, therefore the

time of flight in region B, t_B, depends only upon the longitudinal momentum of the particle at the end of the spectrometer region:

$$t_B = \frac{L_B}{\sqrt{v_z^2 + 2a_A L_A}} = \frac{mL_B}{\sqrt{p_z^2 + 2qmU_A}} \tag{5.1.4}$$

Finally, near the detectors, the particle experiences a final acceleration, a_C,

$$a_C = \frac{q}{m} \cdot E_{MCP} \tag{5.1.5}$$

where E_{MCP} is the electric field between the front of the MCP and the end of the drift tube, given by

$$E_{MCP} = \frac{U_{MCP,F} - U_{drift}}{L_C} = \frac{\Delta U_{MCP,F}}{L_C} \tag{5.1.6}$$

where $U_{MCP,F}$ and U_{drift} are the potentials applied to the front of the MCP and the drift tube respectively and their difference is ΔU_{MCP_F}. E_{MCP} can be very large ~2 kV/cm, but is applied over a very small distance. The time of flight for the particle in region C, t_C, is thus

$$\begin{aligned} t_C &= \frac{2L_C}{\sqrt{v_z^2 + 2a_A L_A + 2a_C L_C} + \sqrt{v_z^2 + 2a_A L_A}} \\ &= \frac{2mL_C}{\sqrt{p_z^2 + 2qmU_A + 2qmU_{MCP,F} L_C} + \sqrt{p_z^2 + 2qmU_A}} \end{aligned} \tag{5.1.7}$$

The total time of flight for the particle travelling from the ionisation event to the detector, t, is the sum of the times of flight in each region:

$$\begin{aligned} t = &\frac{2L_A}{\sqrt{v_z^2 + 2a_A L_A} \pm v_z} + \frac{L_B}{\sqrt{v_z^2 + 2a_A L_A}} \\ &+ \frac{2L_C}{\sqrt{v_z^2 + 2a_A L_A + 2a_{MCP} L_C} + \sqrt{v_z^2 + 2a_A L_A}} \end{aligned} \tag{5.1.8}$$

or, in terms of momentum,

$$t = \frac{2mL_A}{\sqrt{p_z^2 + 2qmU_A} \pm p_z} + \frac{mL_B}{\sqrt{p_z^2 + 2qmU_A}} + \frac{2mL_C}{\sqrt{p_z^2 + 2qmU_A + 2qmU_{MCP}} + \sqrt{p_z^2 + 2qmU_A}} \tag{5.1.9}$$

The relative times of flight can be calculated from the difference between the times of flight given by equations 5.1.8 or 5.1.9 for a given initial longitudinal velocity or momentum. However, it is not possible to rearrange these equations to calculate v_z or p_z for a measured time of flight.

Transverse Momentum

The helical motion of particles with a transverse momentum, p_r, after ionisation is confined by a magnetic field of strength, B, describing a circle in the $x-y$ plane shown in figure 5.1.2b as they travel from the ionisation point to the detection point. The circle has a characteristic cyclotron radius, R_c, dependent upon the initial transverse momentum of the particle and the field strength, while the specific detection point also depends upon the time of flight of the particle. With reference to figure 5.1.2b, the angle α is given by

$$\alpha = \omega t \tag{5.1.10}$$

where $\omega = qB/m$ is the cyclotron frequency and t is the particle time of flight given by equations 5.1.8 or 5.1.9. The distance from the ionisation point to the detection point, r, is related to the cyclotron radius by

$$R_C = \frac{r}{2\sin(\pi - \alpha/2)} = \frac{r}{2\sin(\omega t)} \tag{5.1.11}$$

Using the relationship between the cyclotron radius and the transverse velocity $R_C = mv_r/qB$, the magnitude of the transverse momentum, p_r, can be calculated using

$$p_r = mv_r = \frac{rm\omega}{2\sin(\omega t)} \tag{5.1.12}$$

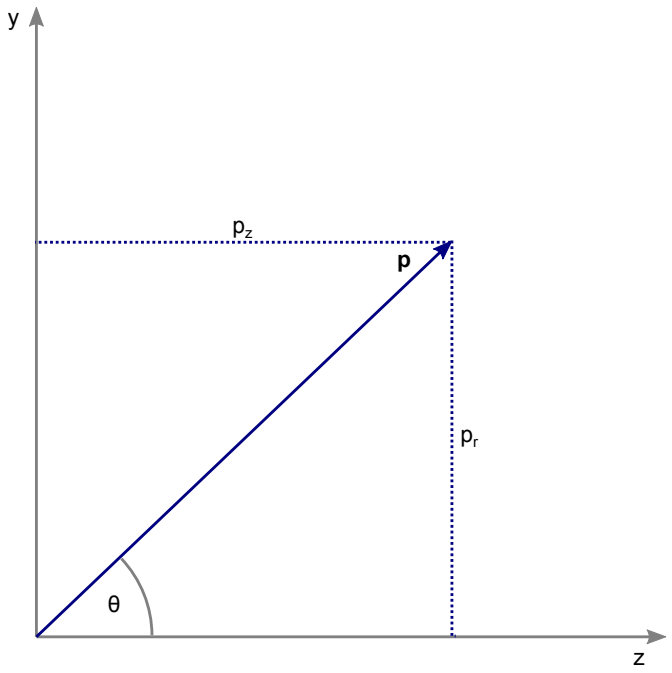

(a) $y - z$

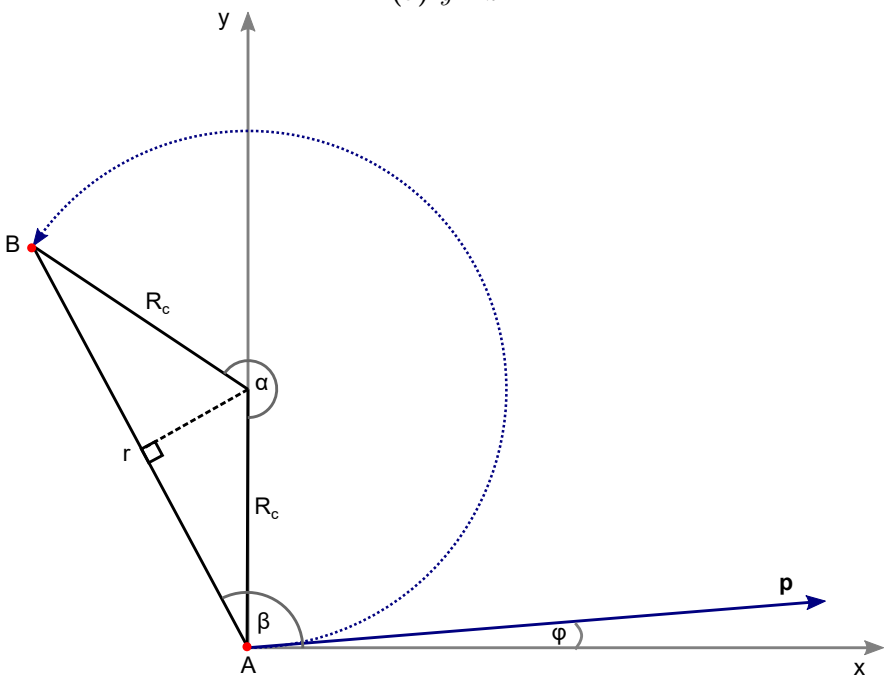

(b) $x - y$

Figure 5.1.2: Momentum reconstruction a) Scattering in the $y - z$ plane where p_z is the longitudinal momentum and p_r is the transverse momentum, with θ the angle between the momentum vector $\boldsymbol{p}$ and the z axis. b) Circle in the $x - y$ plane described by a charged particle moving in a magnetic field from A, the ionisation point, to B, the detection point. Angle ϕ is the angle between the x axis and the radial momentum vector $\boldsymbol{p}_r$

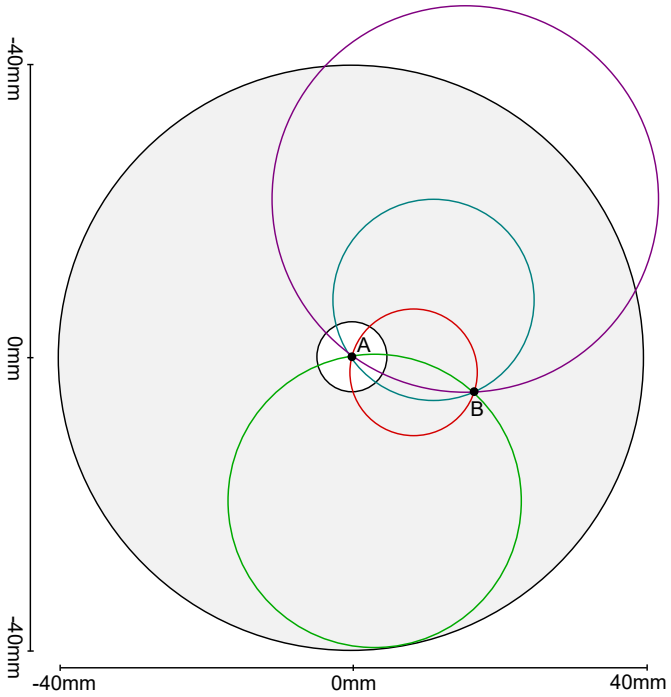

Figure 5.1.3: Representation of the relationship between ionisation point (A), detection point (B) and the transverse energy of a particle. Circles represent the paths described by particles with different transverse momenta, all passing through the same detection point. The underlying grey circle represents the active region of the detector.

Figure 5.1.3 shows a number of circles, representing the helical motion of particles with different transverse momenta, which all pass through the ionisation and detection points. This highlights the fact that knowledge of these two physical points is not enough to determine the transverse momentum, but combined with the time of flight of the particle a unique solution can be determined.

For the longitudinal and transverse momenta, the angle $\theta_{e^\pm}$ in the $y-z$ plane as shown in figure 5.1.2a, is

$$\theta = \cos^{-1}\left(\frac{p_z}{\sqrt{p_r^2 + p_z^2}}\right) \tag{5.1.13}$$

The azimuthal angle ϕ, between the x axis and the transverse momentum vector $\boldsymbol{p}_r$, can be calculated using angles α from equation 5.1.10 and β, given by

$$\beta = \tan^{-1}\left(\frac{y}{x}\right) \tag{5.1.14}$$

where (x, y) are the coordinates of detection point. ϕ is thus

$$\phi = \beta \pm \frac{\alpha}{2} \tag{5.1.15}$$

where the $\pm$ depends upon the direction of rotation of the particle in the magnetic field, in the case where the magnetic field is in the $+z$ direction, this is positive for the clockwise rotation of the electrons and negative for the positrons.

5.2 Experimental Methods

5.2.1 Beam Production

The moderator used for the reaction microscope is frozen neon and the growing procedure is similar to that outlined in section 4.2.1. During initial measurements it was noted that the beam position in the interaction region of the reaction microscope shifted position by around 0.5-1.0 mm, dependent upon the age of the moderator. This significantly affected the positron beam-gas jet intersection, but it was found that longer grow times (1500 s instead of 1000 s) improved the positional stability of the beam position over time.

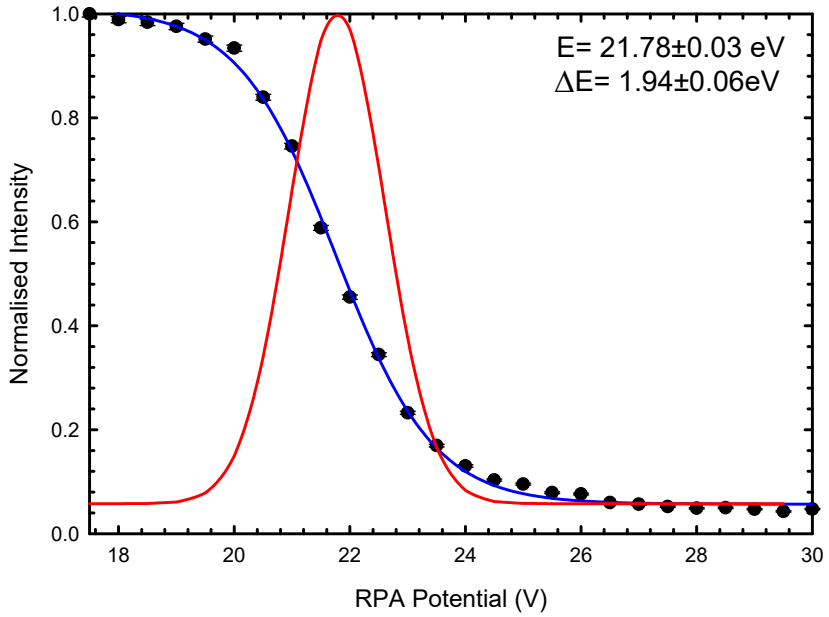

Figure 5.2.1: Measurement of the parallel FWHM energy spread of the positron beam in the scattering cell, at a magnetic field strength of 45 G. •, normalised positron counts/s; — fit to positron counts/s; — Gaussian distibution based on the positron counts/s.

As the trap is unused in the current reaction microscope configuration, the energy spread of the beam is determined by the moderator and the beam energy by the moderator potential. The retarding potential analyser, referred to as RPA2 in the single scattering experiment, is placed in the scattering cell magnet and can be used to measure the energy spread of the beam in the source stage. Figure 5.2.1 shows a cutoff curve, measured similarly to those in figure 4.2.6, using the RPA and the positron/ion detector MCP. The moderator potential was set to 22 V and the magnetic field strengths were 33 and 45 G in the source stage and scattering cell regions respectively. The beam energy is found to be 21.78±0.03 eV with an energy spread of 1.94±0.06 eV FWHM, using equation 4.1.7 this corresponds to an energy spread of 1.42±0.04 eV FWHM in the source stage.

5.2.2 Positron Beam-Gas Jet Interaction

The physical size of the positron beam is initially defined by the 2 mm diameter aperture at the entry of the reaction microscope (see figure 3.3.3). This beam and the effusive gas jet must intersect within the experiment, therefore the size

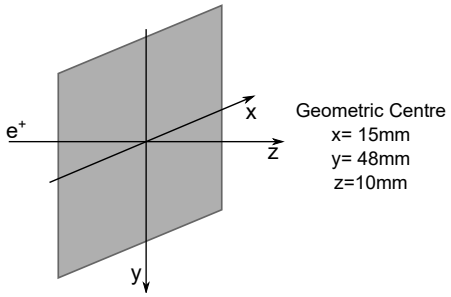

(a) Definition of gas needle coordinates

Counts/s

Counts/s

(b) Example measurement of beam position and size in the x and y directions

Figure 5.2.2: Definition of beam needle coordinates and example of beam position and size measurements using the beam needle.

and location of the beam must be measured. Figure 5.2.2a shows the geometry used to position the beam-gas jet intersection, the gas needle is held in a mount with vernier scales in the x, y and z positions allowing accurate positioning. The z position, along the beam axis, is fixed at $z = 10$ mm, corresponding to the geometric centre of the experiment. The x and y positions are measured by moving the gas needle through the positron beam and detecting the secondary electrons using the electron detector (see figure 5.2.2b for an example). A higher secondary electron count corresponds to positions where the needle is in the path of the beam. The x position is measured by setting y low, at 52 mm, so that the beam will overlap the needle in the vertical direction, and scanning the x position. The y position is measured by setting the x position to the centre of the beam (the peak in figure 5.2.2b) and scanning the y position. The example in figure 5.2.2b demonstrates that the beam does not necessarily pass through the geometric centre which can be due to poor alignment of the reaction microscope solenoids A-F or external magnetic fields from nearby experiments or the Earth's magnetic field.

The gas needle position is set with reference to the beam-gas needle position measurements to maximise the cross over of positron beam and gas jet. The x position is set to the centre of the positron beam whereas the y position is set to ∼3-4 standard deviations above the beam centre. This would be at $x = 16.4$ mm and around $y = 28.5$ mm from figure 5.2.2.

Gas is then admitted into the chamber, controlled by a variable leak valve, so that the background pressure in the reaction microscope is $< 10^{-5}$ Torr, typically this will be around 3×10^{-6} Torr. This pressure is high enough to produce a significant number of ions, but low enough not to damage the detector MCPs.

5.3 Acceptance

The reaction microscope acceptance determines the ranges of longitudinal and transverse momenta which can be detected, and these ranges depend upon the electric and magnetic fields chosen for the experiment. The following discussion is separated into positron and electron acceptance and ion acceptance due to the differences in mass and examples are calculated for single ionised argon atoms with an electric extraction field of 6.262 V/cm, a magnetic field of 10 G

and a 190 eV incident positron beam (the parameters used in data presented in chapter 8).

5.3.1 Positron and Electron Acceptance

The longitudinal momentum acceptance of the positrons and electrons is limited by the extraction field as this determines the potential applied to the drift tube, V_{drift}. Forward scattered positrons, where $\boldsymbol{p}_z$ is in the $+z$ direction, are accelerated in the direction of the positron/ion detector and will be detected for all initial longitudinal momenta. However, backscattered positrons must be turned around by the extraction field in order for them to reach the positron/ion detector, therefore, the maximum longitudinal energy a detectable positron can have in the $-z$ direction is eV_{drift}. Likewise, electrons ejected in the forward direction must have a longitudinal energy in the $+z$ direction less than eV_{drift}. In terms of momentum, these limitations are

$$\begin{aligned} -\sqrt{2m_e q V_{drift}} < \boldsymbol{p}_{z,e^+} &\leq p_{z,max} \\ -p_{z,max} \leq \boldsymbol{p}_{z,e^-} &< \sqrt{2m_e q V_{drift}} \end{aligned} \tag{5.3.1}$$

where $p_{z,max}$ is the maximum longitudinal momentum available in the system. For the experiments here, this corresponds to -2.218 to 3.576 a.u. for positrons and -3.576 to 2.218 a.u. for electrons.

The transverse momentum acceptance for the positrons and electrons is dependent upon the magnetic field strength, the size of the detector and the time of flight. The time for these particles to complete one orbit is given by the cyclotron period, T_C,

$$T_C = \frac{2\pi m}{qB} \tag{5.3.2}$$

For a positron or electron this is $\sim$36 ns, typical flight times are typically 100s of nanoseconds, therefore they can complete several orbits before hitting their respective detectors. If the time of flight for the particle is an integer multiple of the cyclotron period, then the particle will return to the same (x, y) coordinates as the ionisation point, passing through the detector aperture and be undetected.

In addition, particles which have undergone a rotation of close to 2π radians will have small detection radii, r, as calculated using equation 5.1.11. If their r is less than the aperture radius, R_{ap}, then these particles will also pass through the aperture and be undetected. Likewise, when r is larger than the detector radius, R_d, there is a chance that the detection point will not be on the active area of the detector and the particle will not be detected. For example, the purple path shown in figure 5.1.3 indicates a particle where $r \geq R_d$, this particle will only be detected if its time of flight allows it to impact the detector area shown in grey. Therefore, the transverse momentum is limited to

$$\frac{R_{ap} m\omega}{2\left|\sin(\omega t)\right|} < p_r < \frac{R_d m\omega}{2\left|\sin(\omega t)\right|} \tag{5.3.3}$$

where, R_d =40 mm and R_{ap} is 5 mm for the positron detector. Due to the gaps in the electron detector delay lines, R_{ap} is larger for electrons, estimated to be ∼9 mm due to the detector geometry and MCP electron cloud spread, discussed in detail in section 5.4.5.

The combination of the acceptance limitations for the longitudinal and transverse momenta produce acceptance areas as shown in figure 5.3.1, these are valid for the results presented in chapter 8. The sharp horizontal lines are due to the restrictions enforced by the extraction field selection, although overall a large portion of the momentum space is covered for both particles. For comparison, the electron acceptance is also calculated for an extraction field of 4 V/cm (figure 5.3.2a), with all other parameters the same as in figure 5.3.1a. In this example, there is an area at $\boldsymbol{p}_z$ =0 a.u. where electrons cannot be detected, regardless of their transverse momentum. On the other hand, when $\boldsymbol{p}_z$ =-3 a.u, transverse momenta below 0.5 a.u. can be detected at 4 V/cm but not when E_{ex} =6.262 V/cm. Additionally, reducing the magnetic field from 10 to 5 G (figure 5.3.2b) allows even smaller transverse momenta to be detected when $\boldsymbol{p}_z$ =-3 a.u, but transverse momenta greater than ∼0.9 a.u. are rejected. Therefore, in order to fully cover all momentum space the same experiments need to be completed for different extraction fields or magnetic field or combinations of both.

5.3.2 Ion Acceptance

The initial acceptance constraint for the ion is defined by the maximum time of flight which can be detected using the time to digital converter (TDC). The ion

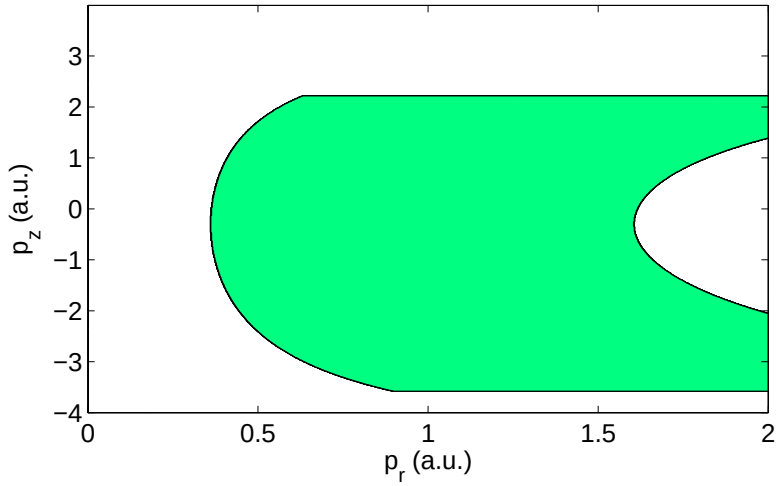

(a) Electron Acceptance

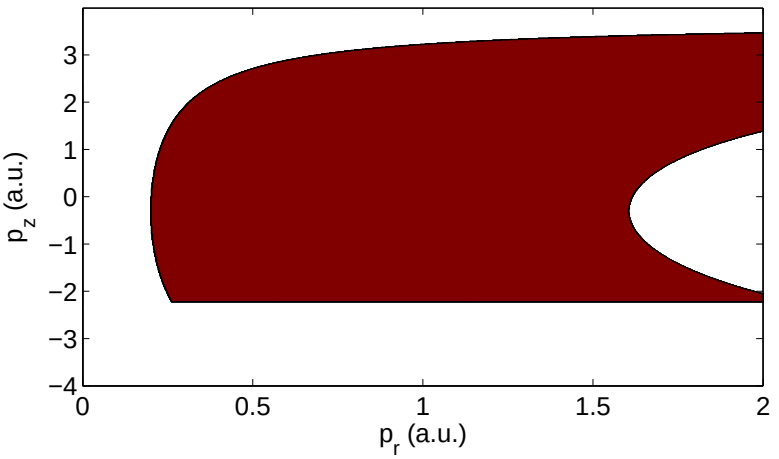

(b) Positron Acceptance

Figure 5.3.1: Calculated momentum acceptance areas for an extraction field of 6.262 V/cm

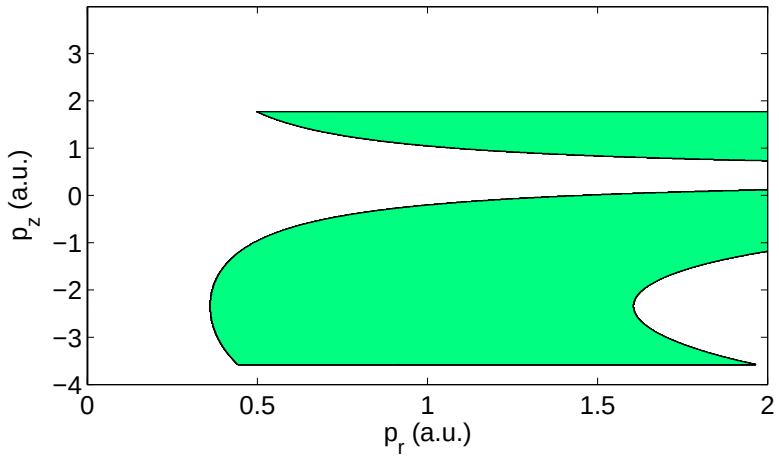

(a) Electron Acceptance at 10 G

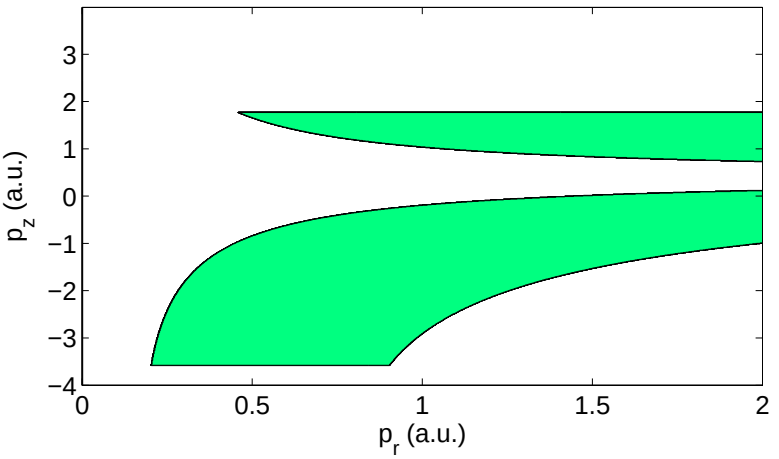

(b) Electron Acceptance at 5 G

Figure 5.3.2: Calculated momentum acceptance areas for an extraction field of 4.0 V/cm

mass, m_{ion}, is significantly larger than the positron or electron and therefore its time of flight is of the order 10^{-6}s as opposed to 10^{-9}s for the positrons and electrons meaning that it is possible for its time of flight to be longer than the time window available. The ion time of flight can be estimated using equation 5.1.9, assuming that the target initial longitudinal momentum is zero. For both supersonic and effusive gas jets, the target starts with a transverse momentum in the $-y$ direction but, whilst the initial longitudinal momentum for the target from a supersonic gas jet is negligible, argon atoms from an effusive jet can have a longitudinal momentum spread of 14.5 a.u. This produces a spread in the ion time of flight equivalent to a few microseconds. The time of flight for a positron, even for a very low extraction field of 1 V/cm, is less than 210 ns meaning that the time of flight for an ion, t_{ion} is approximately equivalent to the relative time of flight measured t_{e^+ion}.

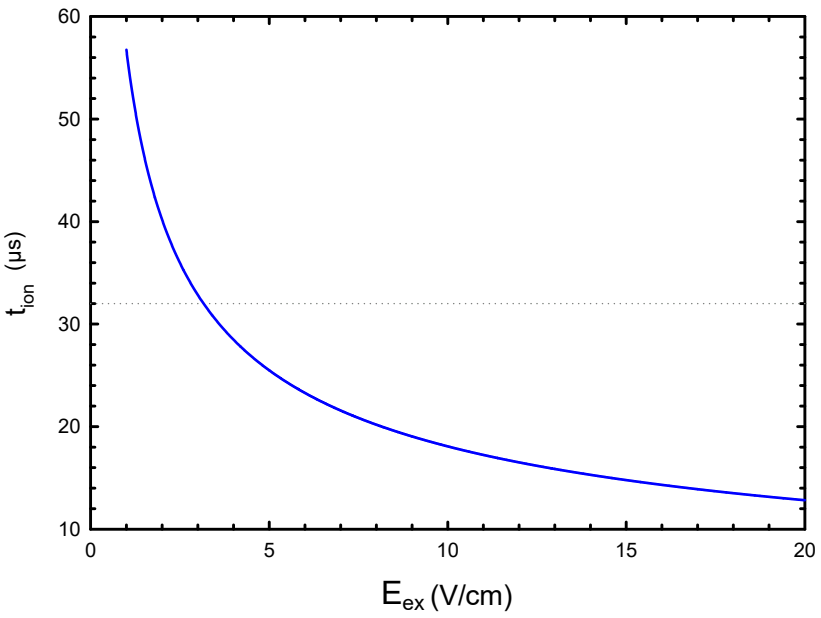

Figure 5.3.3: Simulation of the time of flight for an Ar^+ ion as a function of the extraction field, E_{ex}. The dotted line at 32 μs indicates the maximum time that can be measured using one LeCroy 3377 TDC.

Figure 5.3.3 shows the estimated time of flight for an Ar^+ ion as a function of the extraction field, E_{ex}. The dotted line at 32 μs indicates the maximum time that can be measured using one of the LeCroy 3377 TDCs, this limit can be increased by linking multiple TDCs together, although in the measurements

here only one TDC was used. The extraction field, therefore, must be greater than 3.1 V/cm in order to detect the Ar^+ ion with one TDC. In practice, the extraction field needs to be higher than this in order to account for the time of flight spread. For the measurements here, the time of flight for an Ar^+ ion is $\sim$22.78 μs.

However, appropriate selection of an extraction field is not just limited by the detection time restrictions of the TDC. Figure 5.3.4 shows an example of an experimental t_{e^+ion} spectrum for single ionisation of argon atoms by positrons. The predicted t_{e^+ion} can be seen with a peak at t_{e^+ion} $\sim$23 μs, but two additional features have appeared at t_{e^+ion} $\sim$7 μs and t_{e^+ion} $\sim$9 μs which are unrelated to argon ionisation. Adjusting the extraction field can allow for diagnosis of unexpected peaks, as features due to the presence of real charged particles (such as ionisation of background gases) should shift location in the time spectrum. Features which do not move are most likely to be due to a noise source in the experiment. The features at t_{e^+ion} $\sim$7 μs and t_{e^+ion} $\sim$9 μs do not shift when the extraction field is changed, suggesting that they are not due to charged particles in the system. However, they are consistently present in the measurements indicating some regular noise source, which may be due to an issue in the electronics used to collect data. Therefore, the extraction field should be set such that the peaks of interest (those due to the ionisation of the target) are well separated in time from any spurious signals.

The longitudinal momentum acceptance for ions is again defined by V_{drift} so that backscattered ions with a momentum greater than $\sqrt{2m_{ion}q_{ion}V_{drift}}$, where q_{ion} is the ion charge, cannot be turned around and detected on the positron/ion detector. However, for Ar^+ this is a momentum of -600 a.u., much higher than is possible for these collisions, so all ions should be detected.

The large ion mass also means that the cyclotron period is very large, for Ar^+, T_C =2.6 ms and in 22.78 μs completes 0.009 orbits. The ion mass also means that ω is very small, and equation 5.1.12 can be rewritten,

$$\lim_{\omega \to 0} p_r = \frac{mr}{t} \tag{5.3.4}$$

which removes the dependency upon B. The minimum and maximum transverse momenta that can be measured are again dependent upon R_d and R_{ap}, substituting these values for the positron/ion detector into equation 5.3.4 gives minimum

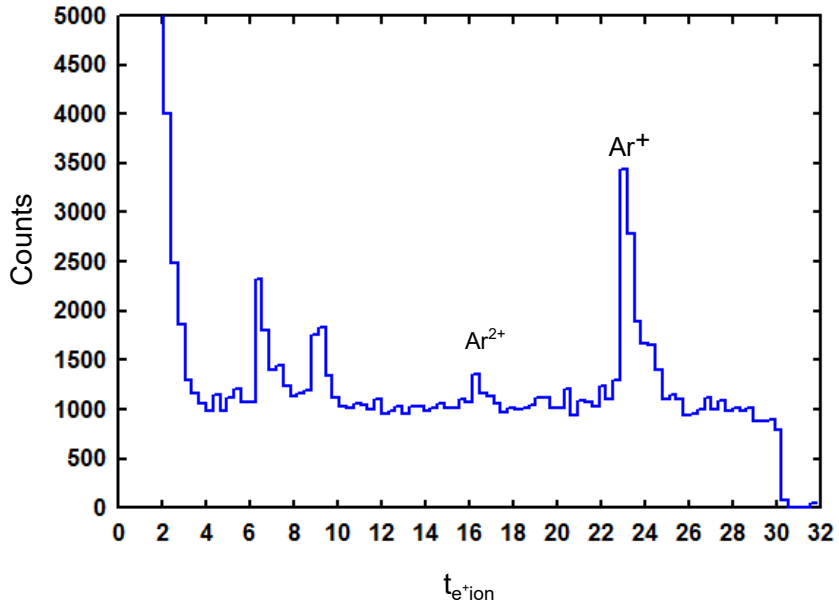

Figure 5.3.4: Example of a positron-ion time spectrum showing a peak due to the production of Ar_+ ions. Also shown is a small peak due to the production of Ar_{2+} ions. The peaks around 7 to 9 μs are experimental artefacts which occur regularly even when argon is not present in the system.

and maximum transverse momenta of 7.36 and 58.56 a.u. for t =22.78 μs. However, since the gas jet 'shifts' the transverse momentum in the $-y$ direction, argon ions which have not gained transverse momentum from the ionisation collision can still be detected.

5.4 Reaction Microscope Data Analysis

The reaction microscope produces files containing data which has been converted from the binary output of the time to digital converter (TDC) into channel numbers and the time the pulse arrived before the COM Stop signal. The pre-processing selection criteria provided by the NIM unit electronics removes some of the unusable data prior to saving it as an output file (as discussed in 3.3.4), however, there are multiple additional requirements which need to be met before the data can be finally accepted. Once accepted, time and spatial information must be extracted from the signals available. The criteria for a 'good' event are similar to those outlined in the discussion of signal pre-processing in section 3.3.4, but in order for the event to be included in the final data it must pass a number

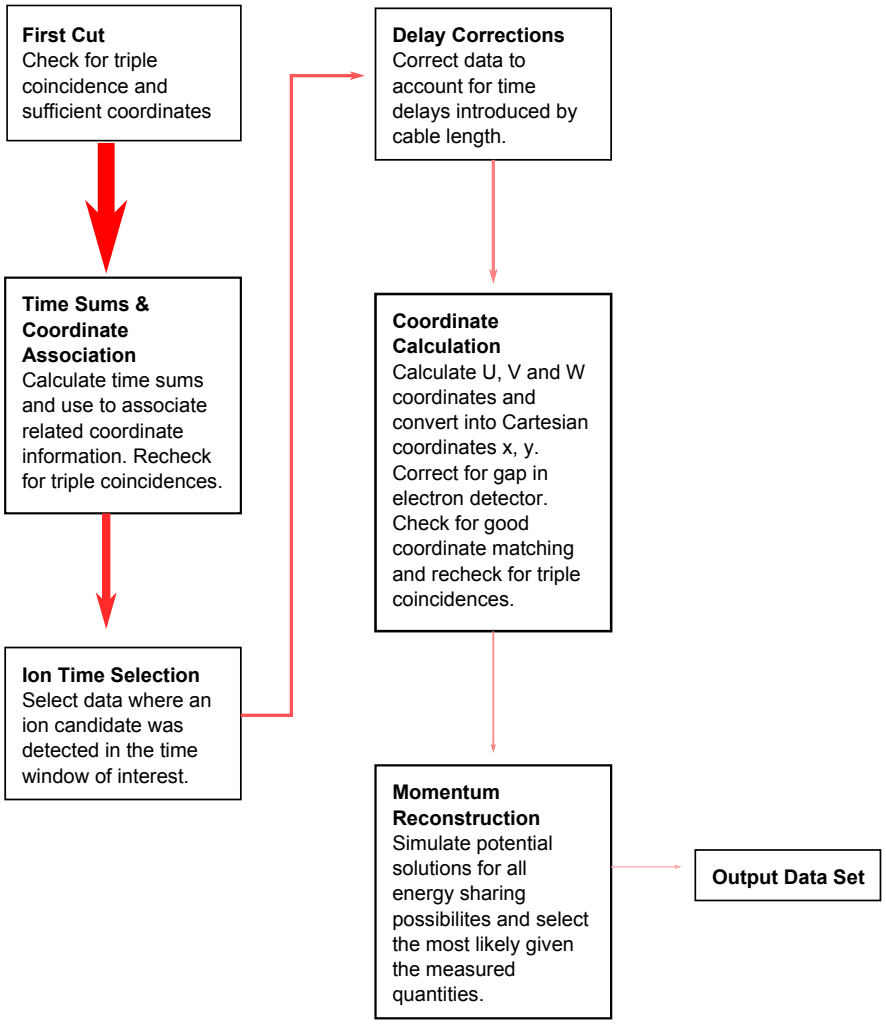

Figure 5.4.1: Summary of the post-processing analysis procedure. The thickness of the arrows qualitatively represents the amount of data which continues through each stage, where a thicker arrow indicates more data than a thinner arrow.

of additional checks and undergo some corrections, the process is summarised in figure 5.4.1.

5.4.1 First Cut

The first cut section roughly cuts out data where there is no possibility of a triple coincidence. A triple coincidence at this stage is assumed to be possible if there are at least two hits on the positron/ion detector and one or more hits on the electron detector, there must also be enough coordinate information for this number of hits. As mentioned previously, each coordinate (U, V or W) requires

two delay line signals (e.g. U1 and U2) and an MCP signal. The signals must simply exist and are not properly associated until the next steps. This rough cut reduces the size of the data files significantly.

5.4.2 Time Sums and Coordinate Association

The experimental data taken to date with the reaction microscope runs the time to digital converter (TDC) in COM Stop mode, meaning that the output time signals t_1 and t_2 for each delay line layer are given in bins (1 bin=500 ps) relative to the COM Stop signal. Figure 5.4.2 demonstrates this relative measurement where COM Stop is the delayed MCP signal . Since the delay lines sit very close to the bottom of the MCP, the time for the electron cloud exiting the MCP to travel to the delay line is assumed to be negligible and the time differences shown in grey between the MCP and U1/U2 signals is approximately equal to the time of propagation of the signal along the delay line.

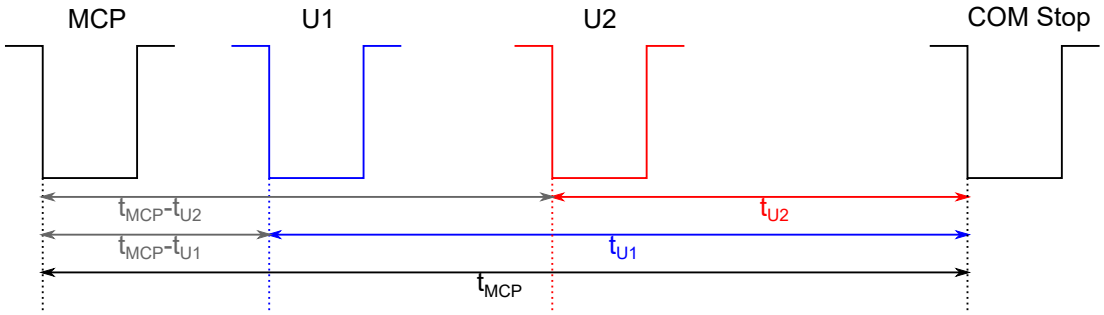

Figure 5.4.2: Example of time calculation relative to the MCP signal for delay line signals U1 and U2.

Following a hit on a detector MCP, it is possible for there to be up to six delay line signals associated with the initial MCP which contain coordinate information for that particle. Not all of these delay line signals are always detected, it is common to only acquire one of a pair. If this observed signal is due to noise it will not be associated with the MCP signal. The simplest check for correct association of delay line to MCP signals is to calculate the time sum, t_{sum},

$$t_{sum} = (t_{MCP} - t_1) + (t_{MCP} - t_2) \tag{5.4.1}$$

where t_1 and t_2 are the arrival times for the delay line signals at each end of the wire and t_{MCP} is the arrival time of the MCP signal as are shown in figure 5.4.2.

The time sum gives a characteristic time for the propagation of a signal from one end of the wire to the other, therefore delay line signals associated with each other must arrive within a time window defined by these time sums.

In order to find this time window, the time differences between MCP and each delay line signal are calculated and if this difference is more than 1000 bins (500 ns) they are discarded. Figure 5.4.3a shows the range of time sums for one of the layers in the positron/ion detector. This histogram can be fitted using a Gaussian function to give the peak time sum and the spread, in this case $\pm 3\sigma$ gives a range of around 20 bins or 10 ns, which is a typical time window width. Figure 5.4.3b summarises typical time sum fits for the U, V and W layers of the positron/ion detector, the time window is defined as the peak time sum $\pm 3\sigma$ and delay lines which do not meet this criteria are discounted. Since the time sums are calculated relative to the MCP, the time window is independent of the particle's actual time of flight from the ionisation event to detection, making the time sums valid for all hits on the detector in use. Time windows are calculated for each data folder, usually corresponding to around 24 hours of data collection, and for each layer of the detectors.

Following these coordinate checks, it is confirmed again whether the remaining data has triple coincidence candidates with sufficient coordinate information.

5.4.3 Ion Time Selection

Data selection is performed based upon the ionisation process of interest. It is possible to simply estimate the time of flight of an ion, formed at the centre of the experiment, with zero initial longitudinal momentum (momentum in the direction of the magnetic field) given the extraction field in use. For example, a singly ionised Argon atom (Ar^+) will take approximately 22.78 μs to reach the positron/ion detector in an extraction field of 6.262 V/cm. This time is measured relative to the positron arrival at the positron/ion detector, but since the positron time of flight is negligible compared to the ion time of flight (tens of ns), it can be ignored for this data selection.

The current use of an effusive gas jet for the target gas introduces some spread in the longitudinal momentum of the atoms prior to ionisation resulting in a range of expected ion arrival times. Figure 5.3.4 shows example data for argon with an

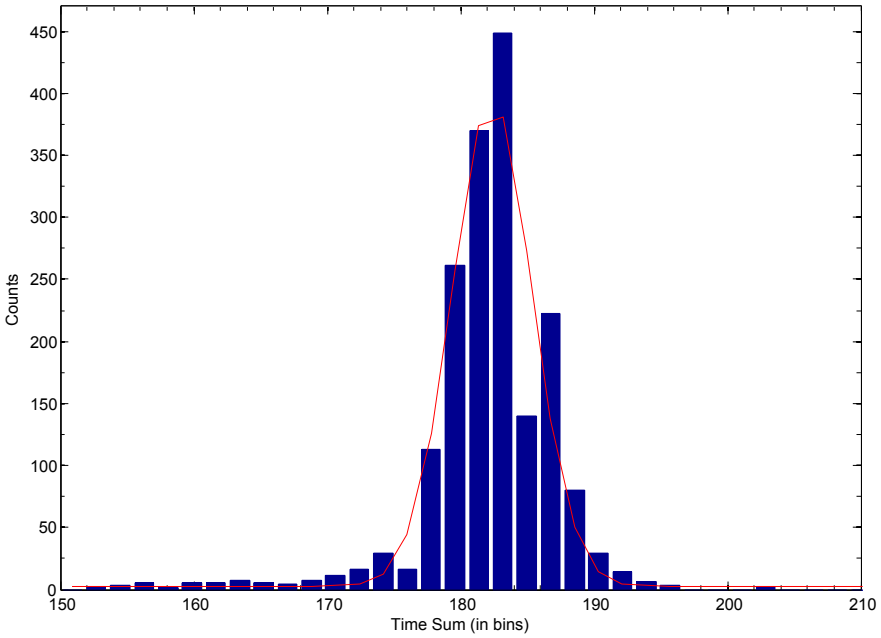

(a) Example of experimental time sum distribution for a layer in the positron/ion detector with a Gaussian fit shown in red

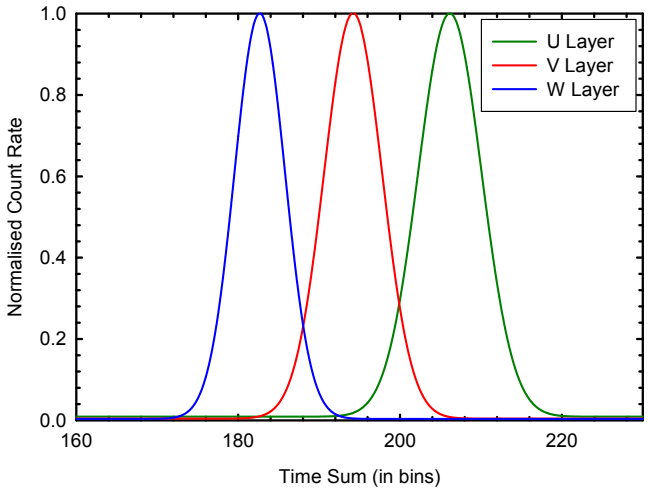

(b) Example of time sum fits for the positron/ion detector

Figure 5.4.3: Example of time sum data and fitting procedure.

extraction field of 6.262 V/cm, plotting the positron-ion time (t_{e^+ion}), the time difference between the arrival of the ion and positron versus count rate. The peak at ∼23 μs is due to Ar^+, whilst the smaller peak at ∼16.5 μs can be attributed to Ar^{2+}. The peaks at 7 and 11 μs are identified as noise, present whether target gas is in or out of the experiment. Selection of a good t_{e^+ion} time window allows noise or other events (such as multiple ionisation) to be removed from the data. In this example, an appropriate time window would be $22.3 \leq t_{e^+ion} \leq 25.4\mu$s to isolate the Ar^+ events, data outside this time window would then be removed from the final data set. Thus a data set containing candidate data can be produced for further processing.

5.4.4 Delay Corrections

Relative time of flight for particles is one of the key measurements made using the reaction microscope. The cabling between the potential dividers, through the amplifiers to the output of the constant fraction discriminators (CFDs) is kept consistent for each detector respectively. This means that the MCP signal for one detector is delayed by the same amount as the delay lines for that detector. However, as discussed in section 3.3.4 the cables from the electron detector CFDs to the LeCroy 4616 unit are not of uniform length which must be corrected for the extra time delay introduced. Simply, this is done by subtracting the delays in table 3.2 from each of the signals ensuring correct conversion from time in nanoseconds to TDC bins.

5.4.5 Coordinate Calculation

The signals from the detectors can be combined to give three coordinates, U, V and W by calculating the relative time difference between the arrival time of the MCP signal, t_{MCP}, and the delay line signals $t_{U1,U2...W2}$:

$$\begin{aligned} U &= (t_{MCP} - t_{U1}) - (t_{MCP} - t_{U2}) \\ V &= (t_{MCP} - t_{V1}) - (t_{MCP} - t_{V2}) \\ W &= (t_{MCP} - t_{W1}) - (t_{MCP} - t_{W2}) \end{aligned} \tag{5.4.2}$$

where the arrival times have been corrected for additional delays as discussed in section 5.4.4.

Each of the delay lines have a slightly different length dependent upon the detector wrapping, this is reflected by the differences in the peak of the time sums as shown earlier in figure 5.4.3b. In order to account for this the coordinates U, V, W are multiplied by scale factors S_U, S_V and S_W,

$$\begin{aligned} S_U &= TS_U/TS_U \\ S_V &= TS_U/TS_V \\ S_W &= TS_U/TS_W \end{aligned} \tag{5.4.3}$$

where TS refers to the peak time sum for each layer. The coordinates U, V and W are thus

$$\begin{aligned} U' &= S_U \cdot U \\ V' &= S_V \cdot V \\ W' &= S_W \cdot W \end{aligned} \tag{5.4.4}$$

Positron/Ion Detector

The conversion from U', V', W' to cartesian coordinates (x, y) for the positron/ion detector is relatively simple compared to the electron detector as there are no gaps in the delay line windings. The (x, y) coordinates from each pair of layers, UV, UW and VW are

$$\begin{aligned} x_{UV} &= U' \\ y_{UV} &= \frac{1}{\sqrt{3}}(U' - 2V') \\ x_{UW} &= U' \\ y_{UW} &= \frac{1}{\sqrt{3}}(2W' - U') \\ x_{VW} &= V' + W' \\ y_{VW} &= \frac{1}{\sqrt{3}}(W' - V') \end{aligned} \tag{5.4.5}$$

The three layers can be combined for this detector by averaging the contributing x and y coordinates for each pair of layers.

Electron Detector

The gap in the electron detector windings means that there are significant detector dead areas as when the electron cloud from the MCP hits the gap, there is no pulse generated. Unlike the positron/ion detector there is now no linear relationship between the difference in signal propagation times and the position on the delay line. To correct for this, the coordinates U', V', W' calculated from equation 5.4.4 are shifted depending upon which side of the gap the cloud hit. Figure 5.4.4) defines the dimensions of the electron detector gap where d is the total side length of the delay line, h is the size of the gap and $l_{1,2}$ are the lengths either side of the gap.

The position of the gap itself, is found by converting the bins from time into millimetres and using the geometric measurements for each layer of the detector which were given in section 3.3.3 in figure 3.3.5. Given this information the coordinates are shifted, for example, for the U layer where the gap is located at U_{gap},

$$U'_{shifted} = \begin{cases} U' - h/2 & \text{if } U' < U_{gap} \\ U' + h/2 & \text{if } U' > U_{gap} \end{cases} \tag{5.4.6}$$

likewise for the V and W layers.

If the centroid of the MCP electron cloud hits the gap, then the pulse which is detected no longer corresponds closely to the centroid's location, therefore hits on the electron detector which are within 3 mm of the edge of the gap are removed (where the electron cloud distribution is estimated using Lapington and Edgar (1989)). The shifted coordinates are then converted into cartesian coordinates using 5.4.5 where U' is replaced by $U_{shifted}$ and so on. The impact of these shifts is shown in figures 5.4.5a and 5.4.5b.

Finally, for both positron/ion and electron data the coordinate matching is tested. Good coordinate matching means that the x and y coordinates calculated from each pair of layers is similar, in this case the coordinates are considered to be well matched if the difference is $\leq$2 mm, the full width half maximum of the

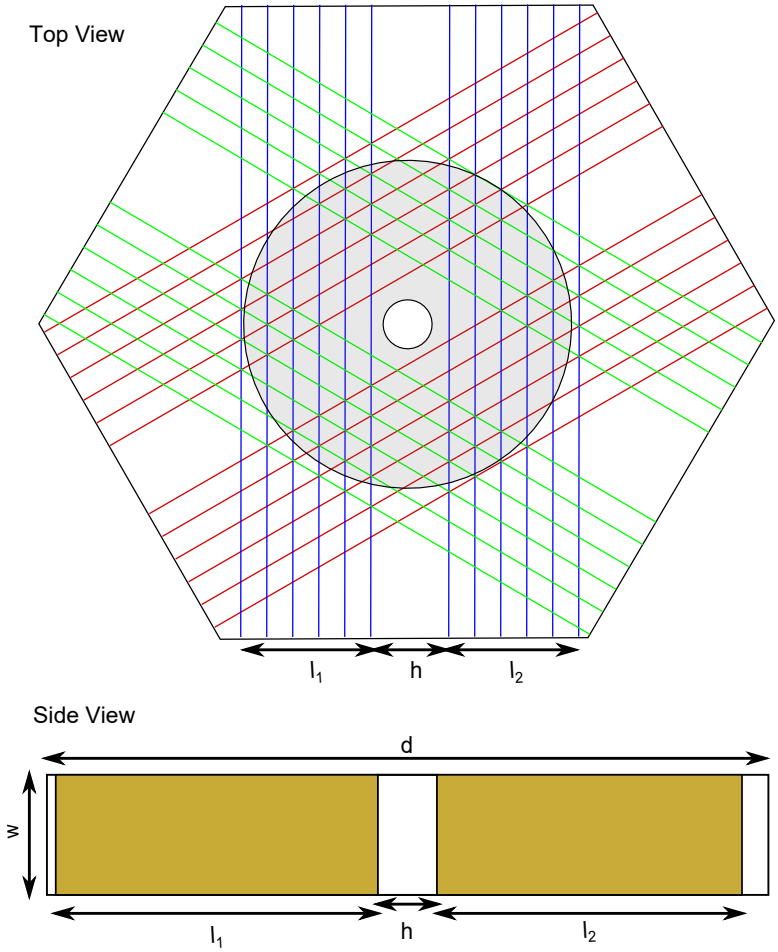

Figure 5.4.4: View of the gap in the electron detector from the top and side

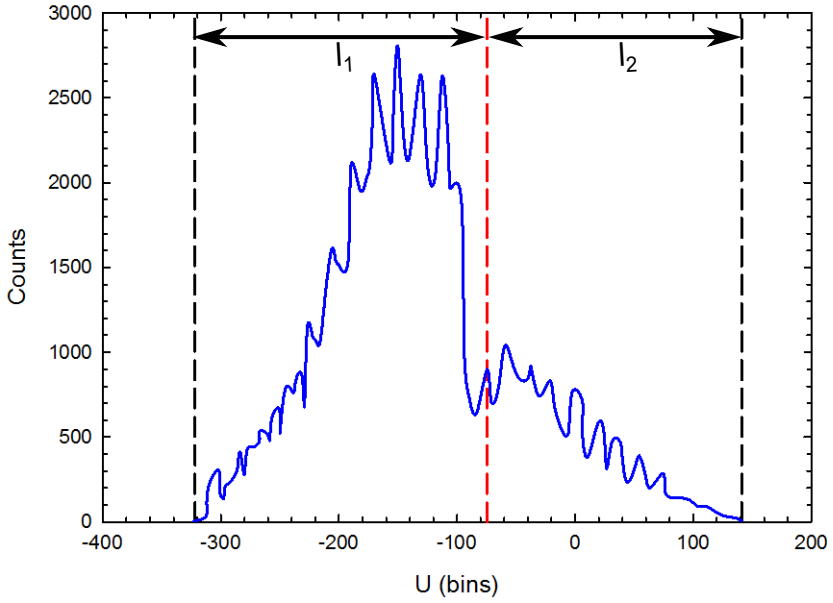

(a) Example data for the U layer before correction for the delay line gap

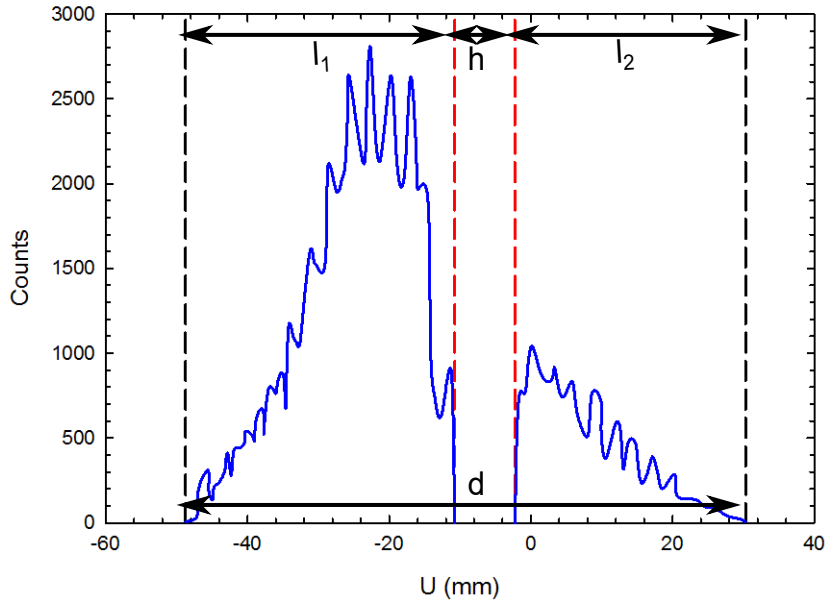

(b) The example data from a) with shifts accounting for the delay line gap

Figure 5.4.5: Example of the correction applied to data to account for the delay line gap in the electron detector.

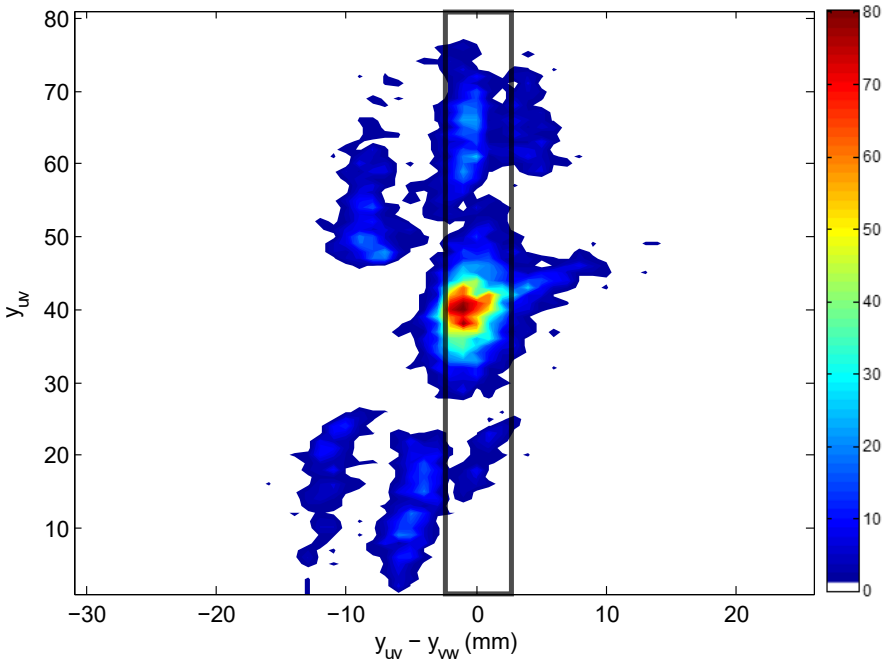

Figure 5.4.6: Comparison of the electron detector y coordinate calculated from the UV layers with that from the VW layers. The black box indicates events which would be considered well matched under the criterion $-2 \leq y_{uv} - y_{vw} \leq 2$ mm i.e. the difference in the y coordinate calculated from the two different pairs of delay lines is within 2 mm. The high intensity point in the centre of the image is simply indicative of a positron beam focused onto the detector, producing a lot of events in one location.

spatial spread of the positron beam. Figure 5.4.6 compares the matching of the y coordinates calculated from the UV and VW layers. 76% of coordinates are within acceptable limits in this example, therefore 24% of events are removed from the data set and a final check for triple coincidences is performed. Events where there is poor coordinate matching are indicative of a 'bad' U, V or W coordinate which can be due to noise, for example on the detector and associated electronics.

Following calculation of the (x, y) coordinates for each event, detector images can be constructed (see figure 5.4.7). The positron/ion detector has a characteristic hole in the centre due to the hole in the MCP and the electron detector has a star shaped hole in the centre due to the combination of the gaps in each layer.

Momentum reconstruction requires information about the deviation of the detected particle's position from the ionisation event position. When the positron

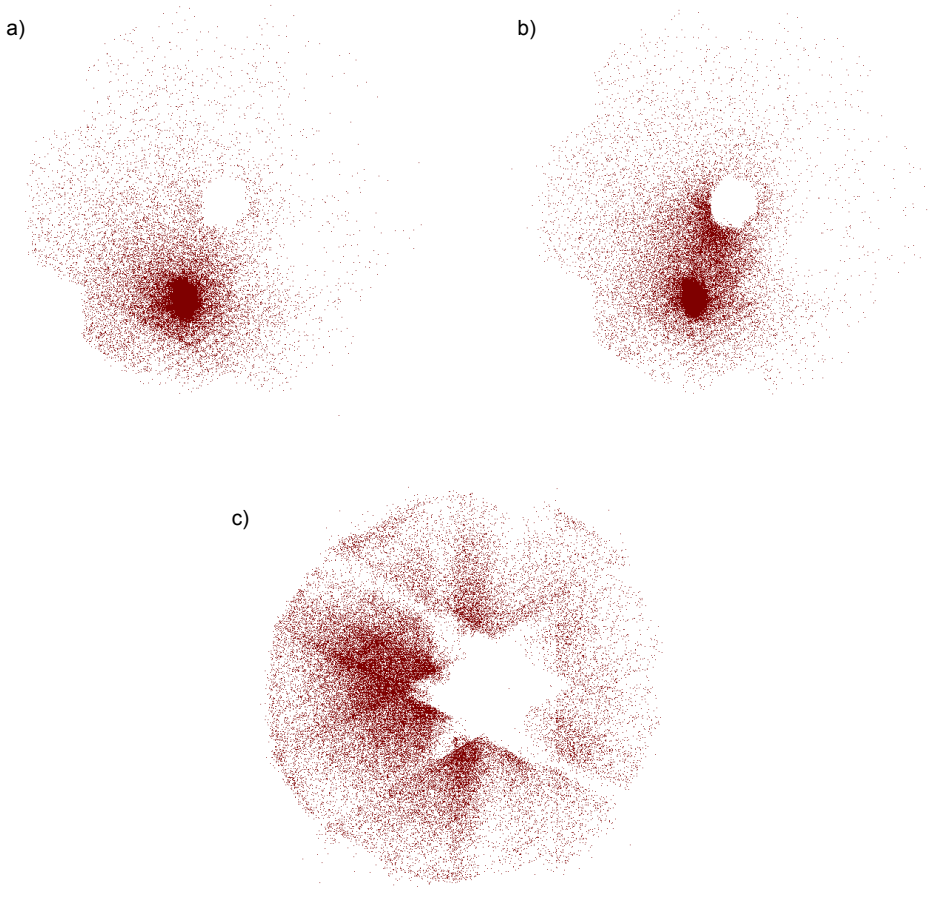

Figure 5.4.7: Examples of typical detector images a) Positrons on the positron/ion detector b) Ion candidates on the positron/ion detector c) Electrons on the electron detector

beam is directed through the centre of the positron/ion detector, the ionisation event location is assumed to be the centre of the detector image. However, when the unscattered positron beam is not central on the positron/ion detector, as in figure 5.4.7a), the centre is found by taking a histogram of the x and y coordinates. This gives an approximately Gaussian distribution and fitting to this allows the peak position to be determined. The scattered particle's detected position is then related to the peak position of the unscattered beam in order to find the difference. This method is also applied to the electron detector data and the final output coordinates for both detectors, (x', y') are the differences between (x, y) and the central position. Due to the cyclotron motion of charged particles in a magnetic field, the positions (x', y') describe a circle with a cyclotron radius $r_c = \sqrt{x'^2 + y'^2}$.

The output from this analysis is a list of potential events with the positron-electron time, $t_{e^+e^-}$, (x, y) coordinates and cyclotron radii for the positron, r_{c,e^+}, and electron, r_{c,e^-}, where there was a triple coincidence with an ion candidate in an appropriate time window where all particles have sufficient coordinate information.

5.4.6 Momentum Reconstruction

The reconstruction of the momenta for the particles is complicated significantly by the use of the effusive gas jet in the data taken at present. The target gas is at room temperature, 300 K, therefore its thermal energy is 39 meV ($3/2kT$) which converts into a momentum range up to 14.5 a.u. for argon. The initial positron beam has an energy of 190 eV resulting in a momentum of 3.7 a.u., since this momentum is much smaller than the argon target gas spread it means that conservation of longitudinal momentum cannot be used to find the initial momenta for the positron, electron and ion (the method used in Dürr (2006), Senftleben (2009) and Holzwarth (2010)). However, working in the energy regime it is reasonable to assume that the target atom gains a negligible amount of energy as its mass is much larger than the mass of the positron. It is therefore possible to model the energy sharing as split between the positron and electron and relate this to $t_{e^+e^-}$. The ion is then only used as a selection criterion for positron-electron times to investigate. The following fitting approach to analysis was developed by Eric Knudsen and Dennis Mueller of the University of North Texas.

Simulating Energy Sharing

Momentum reconstruction initially requires the calculation of a lookup table containing all energy sharing possibilities. The total incoming energy of the positron beam, E_{beam}, reduced by the ionisation potential, E_{IP}, can be split between the scattered positron and the ejected electron. Each particle has a longitudinal energy, $E_{z,e^{\pm}}$ in the direction of the magnetic field, and a transverse energy, $E_{r,e^{\pm}}$ in the $x-y$ plane (coordinate system as defined in figure 3.3.2). Thus,

$$E_{z,e^+} + E_{r,e^+} + E_{z,e^-} + E_{r,e^-} = E_{beam} - E_{IP} \tag{5.4.7}$$

where $E_{beam} - E_{IP}$ is referred to as the available energy. All possible combinations of $E_{z,e^{\pm}}$ and $E_{r,e^{\pm}}$ are used in order to calculate the simulated relative times of flight, t_{s,e^+e^-}, using equation 5.1.8. The simulated individual times of flight, t_{s,e^+} and t_{s,e^-}, and the detection positions $r_{s,e^{\pm}}$ using equation 5.1.12 are also calculated for each combination.

Selecting Solutions

The lookup table calculated using the method above is then used to select potential solutions based on the measured relative time of flight t_{m,e^+e^-} and the measured detection points $r_{m,e^{\pm}}$. Initially, only solutions where the simulated relative time of flight is within ± 1 ns (twice the smallest increment of time measurable, as times are measured in bins of 500 ps) of the measured relative time of flight are selected. This allows for removal of a large number of solutions that do not match this criterion. Secondly, an error ϵ is found using the measured and simulated detection points,

$$\epsilon = (r_{s,e^+} - r_{m,e^+})^2 + (r_{s,e^-} - r_{m,e^-})^2 \tag{5.4.8}$$

The best solution selected is when this error is minimised. However, as demonstrated in figure 5.1.3, there can be multiple solutions with a low error, therefore, these are marked for further investigation and are considered distinct if the difference between the cyclotron radii for each solution is greater than 5 mm.

Once solutions have been selected from the simulation, the angles $\theta_{e^{\pm}}$ and $\phi_{e^{\pm}}$ are calculated using equations 5.1.13 and 5.1.15. The angle $\phi_{e^+e^-} = \phi_{e^-} - \phi_{e^+}$

is the relative angle between the two particles. The final results table contains the longitudinal and transverse momenta for the positron and electron and their scattered angles θ and ϕ.

Chapter 6

Results I: Argon

In this chapter, I will present the results of an investigation I lead into the elastic and inelastic scattering of positrons from argon. Differential elastic cross sections were measured for a range of energies from 2 to 50 eV and total elastic and inelastic cross sections are also presented for 2-20 eV. I collected and analysed the data using the methods detailed in chapter 4 and have published these results in Boadle et al. (2016).

6.1 Introduction

The noble gas atom, argon, has a closed valence shell making it relatively simple to model positron-argon scattering. The ability to successfully model positron interactions is very important in terms of our general understanding of the quantum mechanics of these systems, but also helps to develop theoretical models for targets which are less experimentally accessible such as the transition metals and biomolecules. Argon's chemically inert nature, gaseous state at room temperature and ready availability makes it a simple target for experimental work. Similar small atoms, for which substantial, accurate theoretical calculations exist, such as helium and hydrogen are more challenging for experimental work. Helium as a target is simple to use in the laboratory as a chemically inert element, however, preliminary measurements made using this apparatus have demonstrated that the 'flat' differential cross section, where scattering is largely isotropic, can be challenging as backscattered positrons are reflected from the RPA and make a second transit of the scattering cell, increasing the chance of secondary scattering

events. Molecular hydrogen is achievable experimentally and experimental measurements exist, including for DCS (Machacek et al., 2013). Atomic hydrogen is more difficult as it is highly explosive. Therefore, on balance, argon makes an ideal target for experimental validation of theoretical predictions, occupying the space where both good quality theory and experimental accessibility overlap.

Until recently, there was a lot of uncertainty even with the measurement of total scattering cross sections for positron-argon systems. There were many discrepancies between the measured cross sections which could not be explained by consideration of the stated systematic errors for the experiments (Charlton, 1985). Measurements by Jones et al. (2011) of the total and positronium formation cross sections demonstrated that many of these discrepancies can be explained by the forward angle acceptance, the missing angle, of the experiments (see 4.4). Further investigations in Sullivan et al. (2011) showed that if the angular acceptance of the current single scattering experiment used in this thesis is degraded to match that of past experiments, the previous total scattering cross sections can be reproduced. Thus, previous difficulty in obtaining a convergence of experimental and theoretical results can be attributed, at least in part, to this misunderstanding.

The next level of complexity for theoretical modelling is the accurate calculation of partial scattering cross sections (total elastic and total inelastic in this case) and elastic differential cross sections (DCS). DCS in particular are very sensitive to the input parameters of the model. For example, the Relativistic Optical Potential (ROP) model, described in chapter 2, uses experimental measurements of the static dipole polarisability and higher multipoles as inputs, where larger polarisabilities tend to increase the elastic forward angle scattering and thus the total cross section. As discussed in section 2.3, theoretical models produce a set of phase shifts which can then be converted into DCS. The relative strength of each phase shift at a given incident energy affects the angular dependence of the DCS, for example, enhancing the forward angle scattering or in some cases, introducing structures such as 'dips' into the DCS. When integrated over all angles to produce total elastic cross sections (and the addition of other cross sections), this fine structure can be easily lost making it difficult to distinguish between theories which may, at the total cross section level, appear to be in agreement. In addition, the inclusion, or non-inclusion, of Ps formation channels in theories at relevant energies can have an impact on the phase shifts calculated and thus

the structure observed in the DCS. Comparison between experimental and theoretical data at the DCS level may allow for testing of different treatments of Ps formation, which is a challenging problem for theory to handle. Therefore, measurement of these cross sections provides an even more stringent test of available theories than the total cross section alone.

Experimentally, argon DCS have been measured by Coleman and McNutt (1979), Floeder et al. (1988), Smith et al. (1990) and Gilbert et al. (1999) (at energies of $\leq$ 1.5 eV). Floeder et al. (1988) and Smith et al. (1990) measured DCS below and above the positronium (Ps) formation threshold at 8.96 eV, up to a maximum energy of 50 eV (Smith et al., 1990). Both studies used crossed beam experiments where a positron beam from a ^{22}Na source, with a tungsten moderator, intersects a perpendicular gas jet. The scattered positrons were detected using a movable channel electron multiplier (CEM) allowing the flux at each angle to be determined. Physical limitations from the movement of the CEM restricts the scattering angles which can be investigated to 26-65°(±6°) and 30-134°(±8°) for Floeder et al. (1988) and Smith et al. (1990) respectively and the energy spread was ∼2 eV for both experiments. The difficulty in determining the pressure of the argon gas in the interaction region means that these measurements are all relative and were scaled to theory available at the time. They have been folded and rescaled to match the more recent theory and folded DCS experimental results presented (see section 4.4.4).

Coleman and McNutt (1979) investigated low energy DCS with mean energies of 2.2, 3.4, 6.7 and 8.7 eV (below the Ps formation threshold) in the angular range from 20-60°(±8°). Unlike the experiments of Floeder et al. (1988) and Smith et al. (1990), these were time of flight experiments. Positrons were again produced by a ^{22}Na source and fast positrons passed through a scintillator disk where almost all produced a flash of light which was detected by a photomultiplier tube, providing the start timing pulse. The fast positrons were then moderated using magnesium oxide to give an energy spread of ∼1.5 eV. A small (10 mm long) scattering cell contained the argon gas and scattered positrons exited the cell, hitting a CEM and producing an end timing pulse. Simple geometry indicates that positrons scattered at an angle, θ, must travel a longer distance from the cell to the CEM than unscattered positrons, meaning their time of flight is increased by a factor of $1/\cos\theta$. Measurements of the count rate with respect to the positron time of flight allowed the DCS to be calculated and absolute total scattering cross

sections from Coleman et al. (1980) were used as a multiplier to convert relative DCS into absolute DCS. However, the missing angle of the experiment means that the absolute total scattering cross sections were underestimated by ∼40% for an energy of 2.2 eV, compared with the total scattering cross sections of Jones et al. (2011). The current DCS presented in this chapter are consistent with the total cross sections of Jones et al. (2011), therefore the DCS from Coleman and McNutt (1979) have been folded and rescaled using these total cross sections to account for the magnitude underestimation.

Other previous measurements of positron scattering from argon relevant to this work include the absolute electronic excitation cross section for the first two states, $3p^5(^2P_{3/2})4s(J = 1)$ and $3p^5(^2P_{1/2}4s)(J = 1)$ (where J is the total angular momentum), at energies of 11.62 and 11.83 eV respectively (Sullivan et al., 2001b) and ionisation cross sections (Marler et al., 2005) have been made using the positron beamline at the University of California, San Diego. Earlier measurements of positron-impact ionisation of argon were made by Jacobsen et al. (1995); Moxom et al. (1996) and Kara et al. (1997) and were in reasonable agreement with each other.

Theoretical calculations for argon DCS have developed significantly since the experimental measurements discussed above, with the inclusion of more and more scattering channels. The present data is compared with theory from the convergent close-coupling approach (CCC) (Jones et al., 2011) and the relativistic optical potential method (ROP) (Chen et al., 2008; McEachran and Stauffer, 2013; Jones et al., 2011).

The CCC model, as presented in Jones et al. (2011), includes 278 target states and incorporates elastic scattering, electronic excitation and ionisation. This model calculates the ionisation threshold for argon to be 14.97 eV, below the actual threshold of 15.76 eV and the static dipole polarisability is found to be $13.7a_0^3$ which is higher than the experimentally determined value of $11.08a_0^3$ (Teachout and Pack, 1971). A higher static dipole polarisability tends to increase the magnitude of forward (low) angle scattering, which in turn would be expected to increase the total elastic and thus the total scattering cross section.

The ROP model (Chen et al., 2008), on the other hand, incorporates 17 bound and 18 continuum states to form non-local absorption potentials, thereby enabling elastic scattering and inelastic (electronic excitation and ionisation) cross

sections to be incorporated. The static dipole polarisability was calculated to be $10.76a_0^3$ which is below the actual value and was thus linearly scaled to reproduce the experimental value of $11.08a_0^3$. Above 8.96 eV a simulation of Ps formation is included (McEachran and Stauffer, 2013) where it is modelled similarly to ionisation, since both Ps formation and direct ionisation leave the argon atom in an ionised state.

The modelling of Ps formation is challenging for both theoretical calculations and is handled differently by each, which impacts upon their ability to model Ps formation and particularly the energy region between the Ps formation threshold and the first electronic excitation. In the case of the CCC model, this energy region is unreliable as the calculations do not converge, this is due to the complexities of modelling the interaction of positrons with a model of a Ps atom. The ROP model, viewing Ps formation as simply another loss of flux, is able to calculate cross sections in this region as it does not require a specific model for the Ps atom.

6.2 Experimental Details

The measurements presented here were taken with the atomic and molecular beamline in the configuration discussed in chapter 3 for a gas target with a 50 mm long scattering cell. The transport energy, as defined by the potential of the final trap electrode, was set to 80 eV for all measurements and the beam's energy spread was ∼55 meV. The V_m determined from the RPA2 cutoff curves was 90 meV. The scattering cell gas pressure ranged from 0.9 to 1.9 mTorr such that a maximum of 10% of positrons scattered inside the cell.

DCS, total elastic and inelastic cross section measurements were taken with different M ratios (as defined in equation 4.1.7) depending upon the energy being investigated, these are summarised in table 6.1 along with the resultant missing angles and example corrections applied to the total elastic cross sections. The corrections were calcuated using DCS generated by the ROP theory (Chen et al., 2008; McEachran and Stauffer, 2013), it is worth nothing that a smaller missing angle does not always correlate to a smaller correction as the correction also depends upon the shape of the DCS.

Energy (eV)	M	θ_{min} (°)
2	1	12.2
5	1	7.7
8	1	6.1
10	1	5.4
15	2	6.3
20	2	5.4
30	6	7.7
50	6	6.0

a) Differential Cross Sections

Energy (eV)	θ_{min} (°)	Correction (%)
2	17.2	22
4	12.2	12
6	9.9	8
8	8.6	7
10	7.7	11
12	7.0	13
15	6.3	7
20	5.4	5

b) Total Elastic and Inelastic Cross Sections

Table 6.1: a) M ratios, defined in equation 4.1.7, and resultant missing angles for DCS measurements with $V_m = 90$ meV. b) Selected missing angles and corrections applied to the total elastic cross sections calculated using DCS from the ROP model (Chen et al., 2008; McEachran and Stauffer, 2013). The M ratio is 2 and V_m is 90 meV for the total elastic and inelastics cross section measurements at all energies

Statistical uncertainties for the total elastic cross sections were 3-4% and higher for the total inelastic cross section ($> 20\%$) and DCS measurements ($> 10\%$) dependent upon the energy or angle respectively. Systematic uncertainties are estimated to be $\sim 3\%$ and are mostly due to uncertainties in the pressure measurements made using a capacitance manometer (model 690 MKS baratron), with the largest contribution coming from its zero drift (see section 4.4 for a more detailed discussion of these uncertainties). Error bars on the data presented include both statistical and systematic uncertainties.

6.3 Elastic Differential Scattering Cross Sections

The elastic differential scattering cross section measurements are presented in figures 6.3.1 to 6.3.4 spanning the energy range from 2 to 50 eV. Previous experimental data from Coleman and McNutt (1979), Floeder et al. (1988) and Smith et al. (1990) and theoretical calculations using the CCC (Jones et al., 2011) and ROP (Chen et al., 2008; McEachran and Stauffer, 2013) approaches are included.

The lowest energy investigated is the 2 eV DCS, well below the Ps formation threshold in a region where only the elastic scattering channel is available (annihilation is several orders of magnitude lower and therefore considered negligible). At this energy, the DCS is strongly forward peaked with large scattering at low

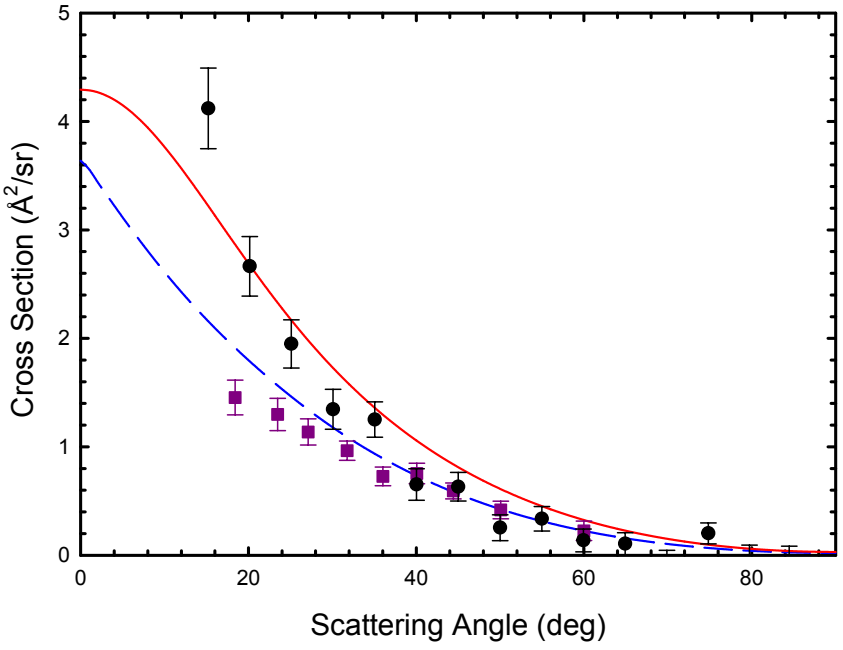

(a) 2eV

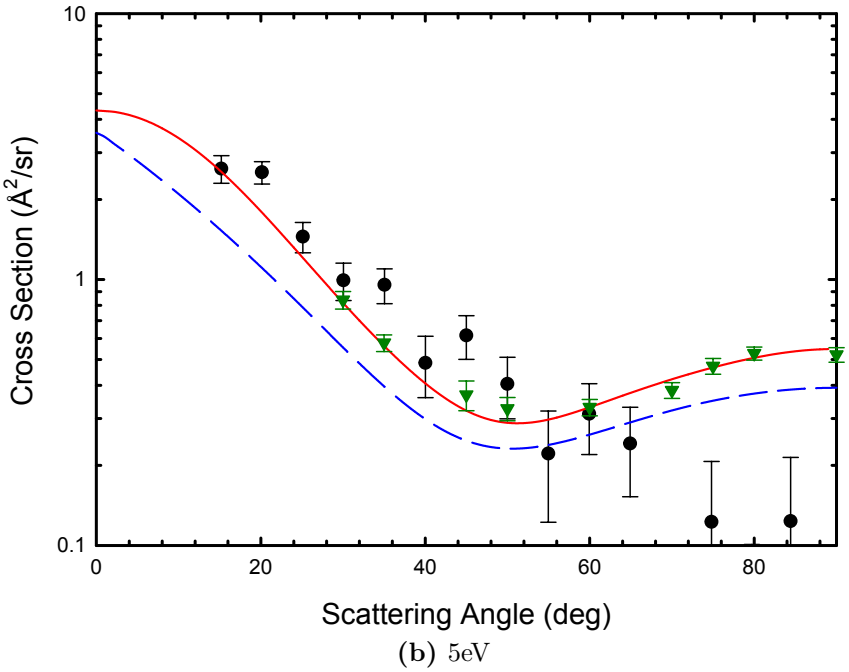

(b) 5eV

Figure 6.3.1: DCS at 2 and 5 eV. •, present data; —, CCC Jones et al. (2011); - - -, ROP Chen et al. (2008); McEachran and Stauffer (2013); ■, Coleman and McNutt (1979) at 2.2 eV in a); ▼, Smith et al. (1990). Note that error bars in b) may appear larger due to the use of a logarithmic scale.

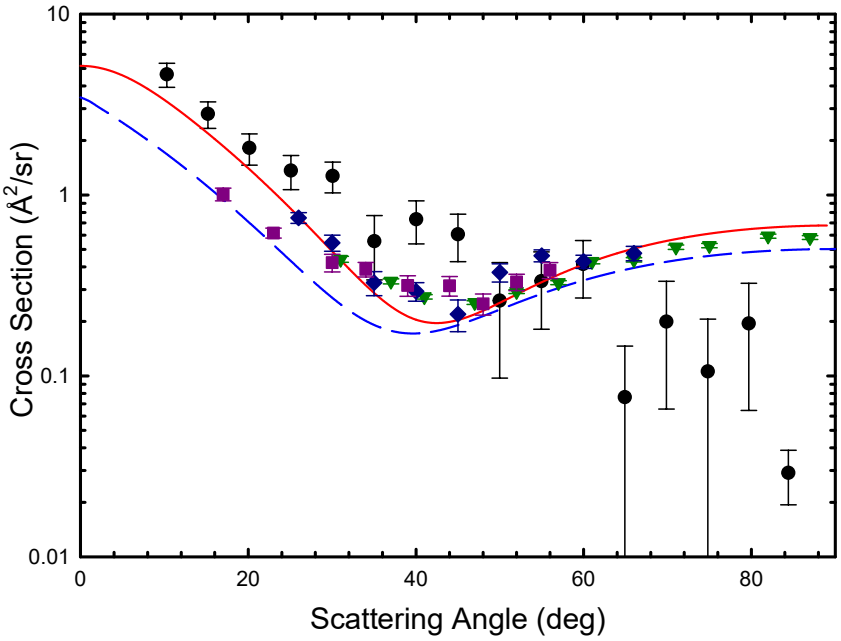

(a) 8eV

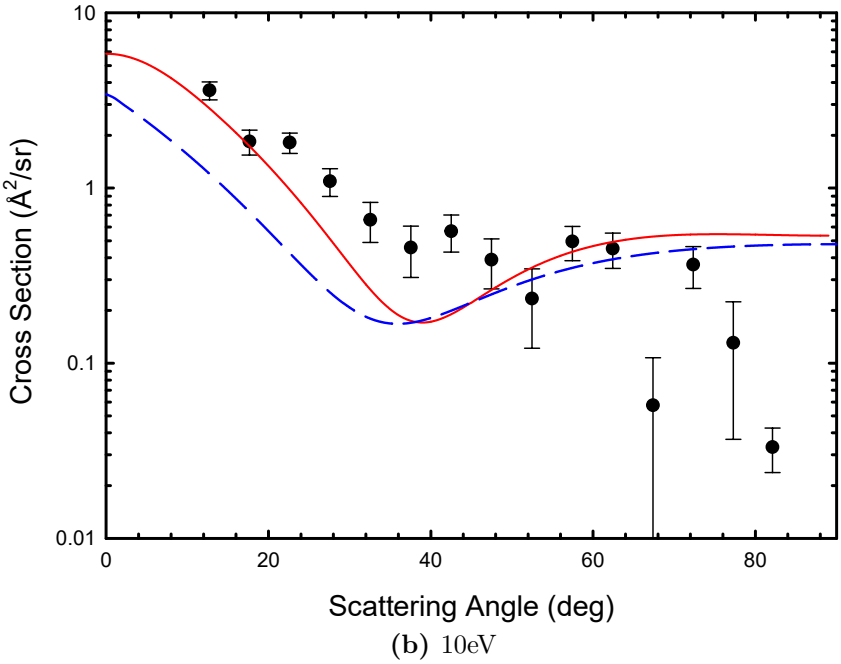

(b) 10eV

Figure 6.3.2: DCS at 8 and 10 eV. •, present data; —, CCC Jones et al. (2011); - - -, ROP Chen et al. (2008); McEachran and Stauffer (2013); ■, Coleman and McNutt (1979) at 8.7 eV in a); ♦, Floeder et al. (1988) at 8.5 eV in a); ▼, Smith et al. (1990) at 8.7 eV in a). Note that error bars may appear larger due to the use of a logarithmic scale.

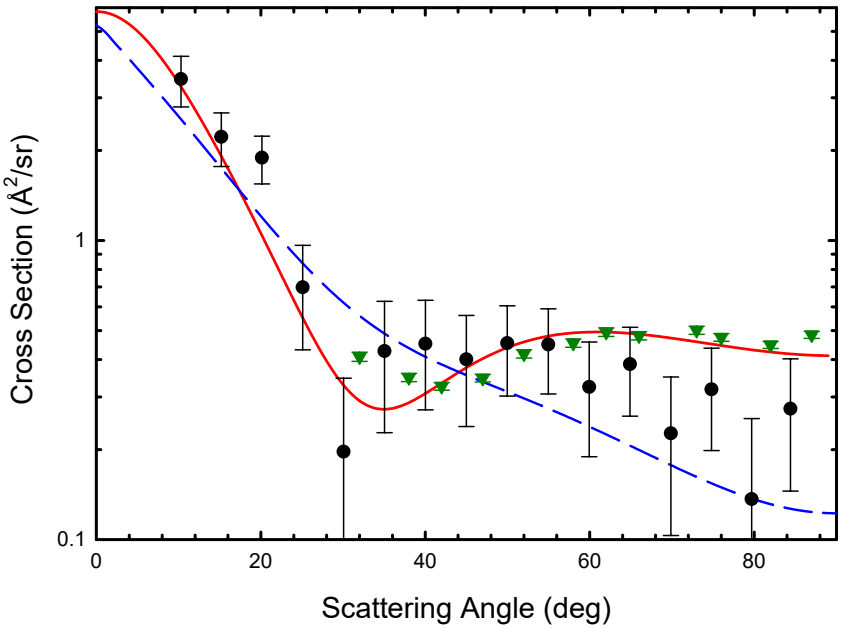

(a) 15eV

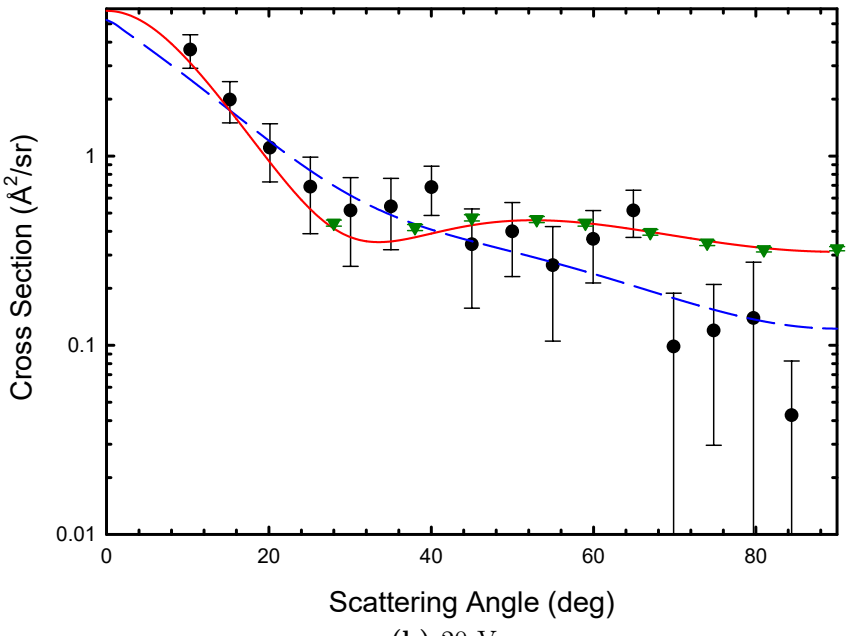

(b) 20eV

Figure 6.3.3: DCS at 15 and 20 eV. •, present data; —, CCC Jones et al. (2011); - - -, ROP Chen et al. (2008); McEachran and Stauffer (2013); ▼, Smith et al. (1990). Note that error bars may appear larger due to the use of a logarithmic scale.

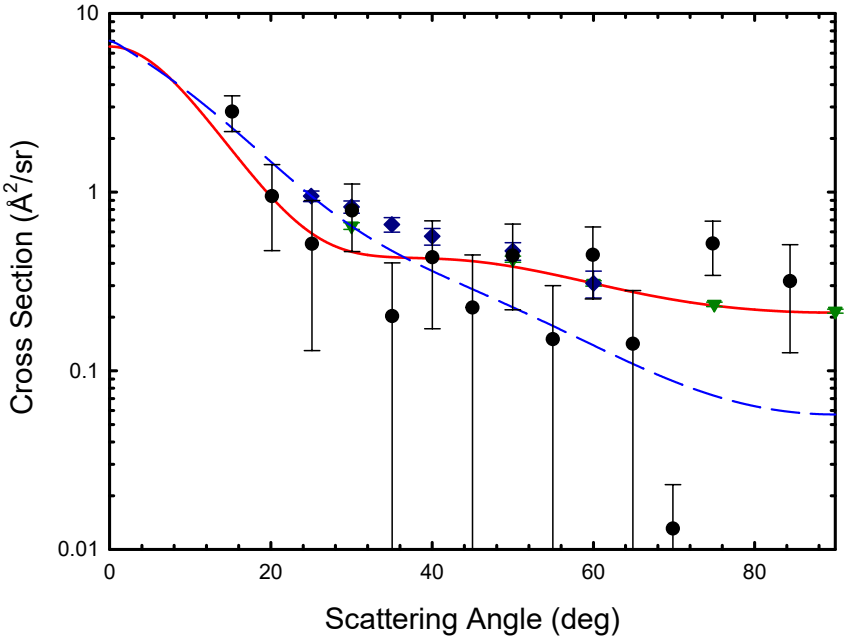

(a) 30eV

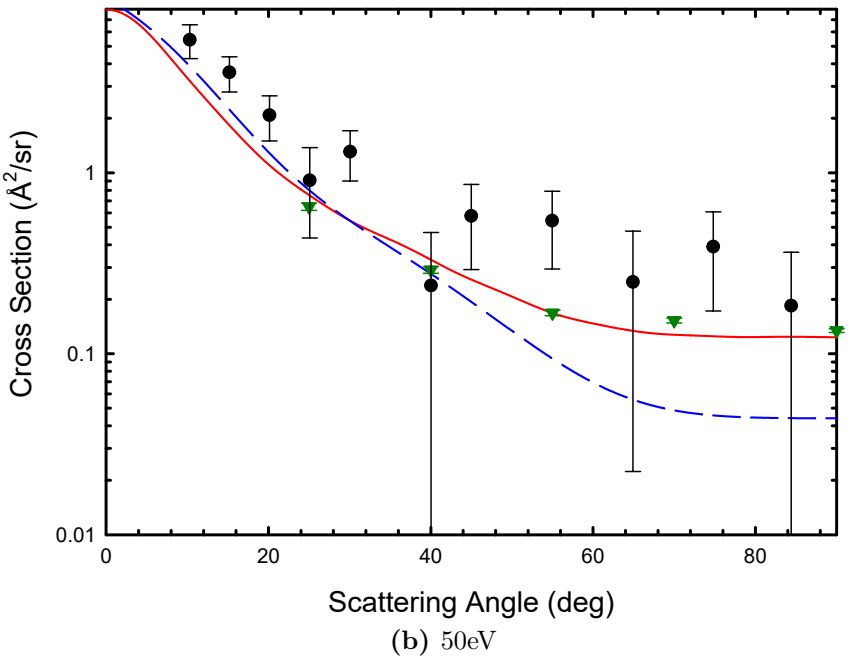

(b) 50eV

Figure 6.3.4: DCS at 30 and 50 eV. •, present data; —, CCC Jones et al. (2011); - - -, ROP Chen et al. (2008); McEachran and Stauffer (2013); ♦, Floeder et al. (1988); ▼, Smith et al. (1990). Note that error bars may appear larger due to the use of a logarithmic scale.

angles. The data from Coleman and McNutt (1979) agrees very well with the ROP model, which both indicate that the forward scattering is not as significant as indicated by the present results. However, the CCC theory agrees very well with the present measurements where forward angle scattering is larger. The effect of the different choices of static dipole polarisabilities on the theoretical calculations discussed above is evident at this energy. The present data is in general agreement with both theories and Coleman and McNutt (1979) until the scattering angle is smaller than $\sim 30^{\circ}$. The discrepancy at lower angles means that if the total elastic cross section were calculated from this DCS, it would be significantly higher for the CCC and present data than for the ROP and Coleman and McNutt (1979) data. In comparison with the measurements by Jones et al. (2011), the total scattering cross section at this energy agress with the CCC theory much better than the ROP theory, which is consistent with the discrepancy observed in the DCS here.

As the energy rises from 5 to 10 eV, below the first electronic excitation and around the 8.96 eV Ps formation threshold, a dip appears in the theoretical models of the DCS and is also present in the measurements of Coleman and McNutt (1979), Floeder et al. (1988) and Smith et al. (1990). The present data is consistent with these measurements, given the statistical errors, although the monotonic decrease in the DCS as the scattering angle increases does not indicate a dip. Again, the present data tends to agree better with the CCC model, which suggests higher cross sections at forward angles than the ROP model. Just above the Ps formation threshold, at 10 eV, the general agreement between the present data and models is poorer which may be indicative of the difficulty in dealing theoretically with the opening of this new channel. Similar issues were also observed in the total cross section comparisons in Jones et al. (2011).

Above the first electronic excitation, figures 6.3.3 and 6.3.4, show that the inclusion of the Ps formation simulation in the ROP model removes the dip which the CCC model continues to predict. Smith et al. (1990) agrees with the dip observed in the CCC model. There is a suggestion of a dip at 15 eV in the present data, but large statistical uncertainties around 25°to 30° make this inconclusive. The ROP model agrees much better at these energies with the present data in the forward direction scattering than at lower energies. The data in figures 6.3.3 and 6.3.4 are in general agreement with both models and the previous data. The CCC and ROP models tend to agree with each other at the

lower scattering angles at these energies, but differ at the higher angles with the ROP model predicting a smaller cross section. In addition, at these higher angles, the current cross sections tend to be smaller than previous measurements. These positrons have been backscattered and therefore reflected by the RPA and made a second pass through the scattering cell. This may lead to some positron flux loss at these energies, reducing the cross section here and increasing the cross section at smaller energies if they re-scatter on the second transit. Generally, this should be a small effect when the target gas pressure is low, or for targets and energies where positrons tend to scatter strongly in the forward direction. Given the uncertainty of the experimental measurements at these high angles, it is not possible to make a conclusive argument for one theory at this point and the data is in reasonable agreement with both models. At the total cross section level, there is convergence at these energies between the present data, CCC model and previous experimental data.

6.4 Total Elastic and Inelastic Cross Sections

The total elastic and total inelastic cross sections are presented in figure 6.4.1. The total elastic cross sections are in good agreement with the CCC theory, consistent with what is observed at the DCS level. The CCC theory is not presented here between the opening of the Ps formation and the ionisation thresholds as the theory has difficulty converging in this region. The ROP model is consistent in shape with the present data, but the magnitude is lower, which is expected given the discrepancies in forward angle scattering between the present measurements and the theory.

The total inelastic cross section is in excellent agreement with the ROP theory, implying that the differences between the ROP theory and the total scattering cross sections noted in Jones et al. (2011) are due to the total elastic portion rather than the inelastic. Experimental data from Sullivan et al. (2001b) and Marler et al. (2005) of electronic excitation and direct ionisation respectively are also included for comparison as at these energies these inelastic processes dominate the inelastic cross section. Below the ionisation threshold the current data and the measurements of the first two electronic excitation ($3p^5(^2P_{3/2,1/2})4s$) states are in reasonable agreement, however by 20 eV the sum of Sullivan et al.

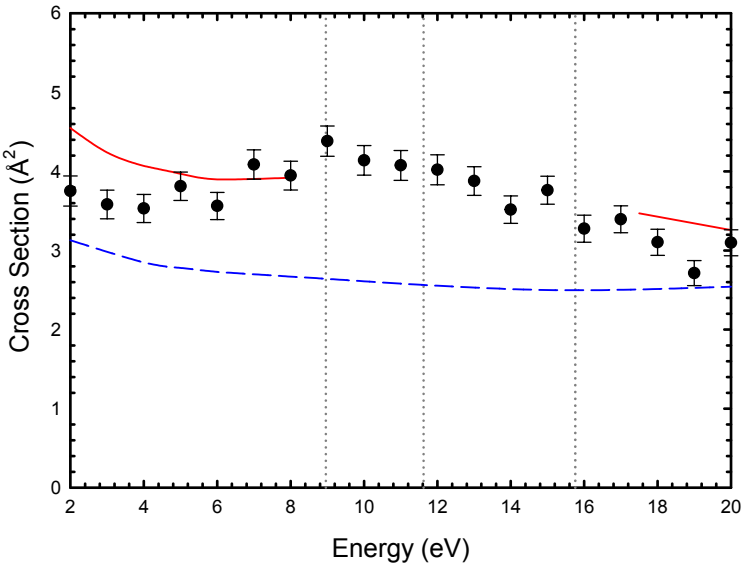

(a) Total Elastic Cross Section

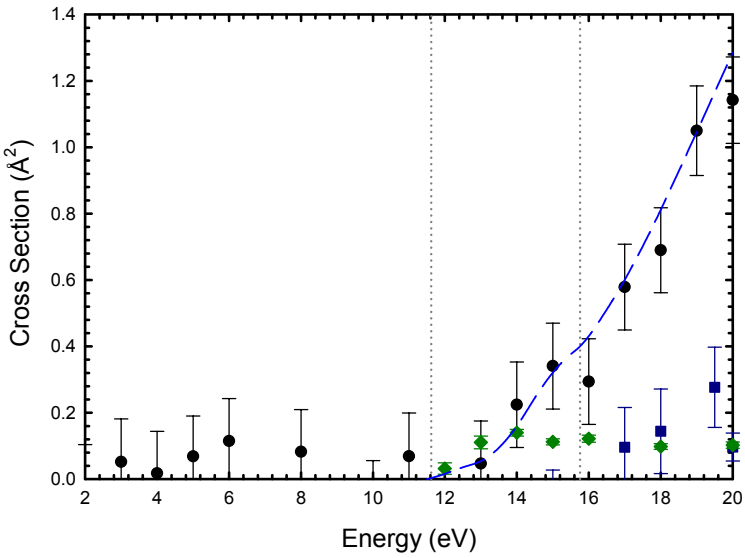

(b) Total Inelastic Cross Section

Figure 6.4.1: Total elastic and total inelastic cross sections from 2-20 eV. Dotted lines in a) indicate the Ps and first electronic excitation thresholds, and the dotted lines in b) indicate the first electronic excitation and ionisation thresholds. •, present data; —, CCC Jones et al. (2011); - - -, ROP Chen et al. (2008); McEachran and Stauffer (2013); ♦, Sullivan et al. (2001b) electronic excitation cross sections for the $3p^5(^2P_{3/2,1/2})4s$ states; ■, Marler et al. (2005) direct ionisation cross sections

(2001b) and Marler et al. (2005) is much lower than the current measurements. At this energy there are many other electronic excitations open, therefore the total inelastic cross section would be expected to be larger than the sum of the two excitation states and ionisation. However, the magnitude of this difference in the present comparison is unexpectedly large. This discrepancy could indicate issues with the present or previous experimental measurements near the electronic excitation threshold. However, it could also suggest that by 20 eV there is a significant amount of excitation to higher energy levels and the agreement with the ROP model indicates that this larger magnitude could be reasonable.

In conclusion, the results presented here are generally in good agreement with previous experimental results and tend to be better described by the CCC model, rather than the ROP model, below the Ps formation threshold. Above this threshold, the agreement between the ROP calculations and the present results improves, as the ROP theory incorporates a model of Ps formation. The CCC and ROP models agrees more at these energies as well, with some discrepancies at higher scattering angles, but are generally in agreement with each other and with the experimental data. Dips in the DCS which were observed in past measurements, and attributed to absorption effects, were not clearly observed in the current data.

Finally, the magnitude of the total elastic cross section agrees well with the predictions of the CCC model, in line with the apparent underestimation of the DCS at small scattering angles in the ROP model. The present total inelastic cross sections also agrees reasonably with past experimental measurements of the first electronic excitation cross sections, but by 20 eV there is a large discrepancy between the current results and past data. Despite this, the ROP model describes the total inelastic cross sections excellently.

Chapter 7

Results II: C_{60}

In this chapter, I present the results of a search I lead for resonances in the total and positronium formation cross sections of positron scattering from C_{60}. I collected and analysed the data using the methods detailed in chapter 4 and present the results here for positron impact energies from 0.4 eV to 50 eV, with more detailed measurements taken below 10 eV in regions where resonant features were predicted by Gianturco and Lucchese (1999).

7.1 Introduction

Positron resonances are formed when a positron becomes transiently associated with a target atom or molecule. It is a temporary state and, unless another process such as annihilation intervenes, will decay into two free states, the positron and the target. Alternatively, the state may decay through emission of a positronium atom. Resonances may appear in energy dependent cross section measurements as features such as 'bumps' or 'dips'.

Positron resonances are analogous to negative ion resonances, where an electron is temporarily associated with the target. These have been observed in almost every atomic and molecular system (for a review, see Buckman and Clark (1994)). However, experimental evidence for positron resonances is much more elusive. Theoretically, positrons can bind to many different targets (Mitroy et al., 2002) and in atomic systems the binding energy can range from 13 meV (e^+Na) to 500 meV (e^+Ca). Positron bound states tend to be short lived, decaying through positron-electron annihilation. Positron bound states with higher binding energies are more accessible to experimental study but unfortunately, many

of the systems for which binding is predicted are difficult to access for gas phase experiments as they are solids at room temperature. Open-shell transition metals, including iron, cobalt and nickel are promising targets for experimental study due to their high dipole polarisabilities and moderate ionisation potentials (Dzuba et al., 2010). Another example of a promising candidate are the large positron resonances expected for magnesium-positron collisions (Mitroy et al., 2002), however, magnesium is a solid at room temperature and requires high temperatures (>700 °C) to reach sufficient vapour pressures.

There is experimental evidence for positron binding to molecules, where large Feshbach resonances were observed in the annihilation cross sections for positron impact on alkanes at energies consistent with theoretical models of binding (Barnes et al., 2003), see also the review paper by Gribakin et al. (2010). In this study, the annihilation cross sections were studied for a range of alkanes, C_nH_{2n+2} for $n = 1-9$ and 12, and for some other molecules including isopentane, partially fluorinated and fluorinated methane, 1-fluorohexane (C_6H_13F) and 1-fluorononane (C_9H_19F). Very large enhancements in the cross sections were observed, corresponding to the excitation of molecular vibrations in larger alkanes. For alkane molecules larger than ethane (C_2H_6), the position of these peaks shifted down in energy by ∼20 meV per carbon atom.

On the other hand, there is no experimental evidence for positron binding to atoms. Investigations so far have searched for positron resonances with H_2, N_2, CO, Ar and He (Sullivan et al., 2001a; Machacek et al., 2012), but no features have been observed to date.

The molecule investigated in this chapter is 'buckminsterfullerene', C_{60}, a soccer ball-shaped molecule consisting of 60 carbon atoms (see figure 7.1.1). Experimental measurements using electron diffraction place the diameter of the icosahedral sphere at 7.113Å with bond lengths of 1.458Å for the five-member rings and 1.401Å for the bonds connecting five-member rings (Hedberg et al., 1991). Theoretical calculations find the bond lengths to be 1.450Å and 1.391Å (Scuseria, 1991). The molecule is therefore huge in comparison to a positron with a large, empty space inside. In electron scattering, C_{60} efficiently captures electrons over a wide range of energies producing fairly stable, negative ions of C_{60} (Matejcik et al., 1995). The prevalence of these states in electron-C_{60} collisions has produced some interest in whether binding or resonances may be formed for positron projectiles.

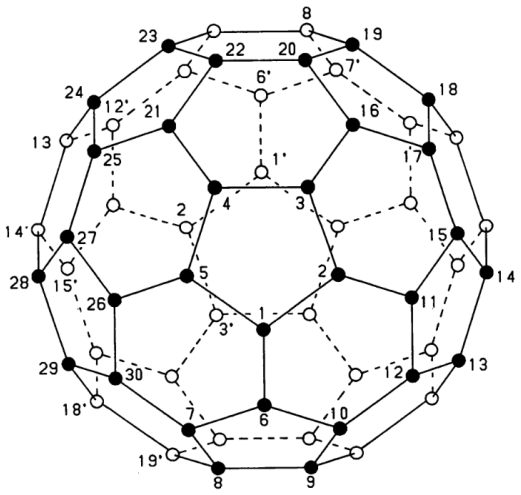

Figure 7.1.1: The C_{60} molecule where • are carbon atoms in the upper hemisphere (unprimed numbers) and ∘ are carbon atoms in the lower hemisphere (primed). Primed atoms and their unprimed counterparts are related by the centre of symmetry of the molecule. Reproduced from Hedberg et al. (1991).

Gianturco and Lucchese (1999) investigated positron-C_{60} scattering theoretically, modelling the potentials in order to determine whether resonances could be formed. The positronium formation threshold for C_{60} is relatively low compared to other targets at ∼0.8 eV (given the ionisation threshold is ∼7.58 eV (de Vries et al., 1992)). Below this threshold, and above it for the elastic partial cross section, the key difficulties in modelling are the treatment of long-range polarisation and short-range correlation effects. Gianturco and Lucchese (1999) approached the model by assuming a fixed-nuclei approximation, such that the positron motion during scattering is not affected by the nuclear motion, and defined their total interaction potential, $V_{tot}(\boldsymbol{r}_p)$ as

$$V_{tot}(\boldsymbol{r}_p) = V_S(\boldsymbol{r}_p) + V_{CP}(\boldsymbol{r}_p) \tag{7.1.1}$$

where $\boldsymbol{r}_p$ is the distance between the positron and the molecular centre of mass, $V_S(\boldsymbol{r}_p)$ is the static potential and $V_{CP}(\boldsymbol{r}_p)$ is the correlation-polarisation potential, defined as

$$V_{CP}(\boldsymbol{r}_p) = \begin{cases} V_{corr}^{DFT}(\boldsymbol{r}_p), & r_p \leq r_p^c \\ V_{pol}(\boldsymbol{r}_p), & r_p > r_p^c \end{cases} \tag{7.1.2}$$

where r_p^c is calculated by locating a position for each carbon atom called the 'polarisable centre' where the dipole polarisability is $1/60^{th}$ the total polarisability of the C_{60} molecule. The polarisation potential, $V_{pol}(\boldsymbol{r}_p)$ is then the sum of 60 equal contributions from different centres. $V_{corr}^{DFT}(\boldsymbol{r}_p)$ is a correlation potential calculated using a density functional theory (DFT) approach in order to describe the short-range potential. Gianturco and Lucchese (1999) calculate two different versions of the correlation potential: V_{ECP}, the electron correlation potential, where scattering is modelled as a homogeneous electron gas without reference to the positron and V_{PCP}, the positron correlation potential, where the homogeneous electron gas model explicitly includes a positron 'impurity'. The model uses the bond-length dimensions of Scuseria (1991) and the calculations were performed using the icosahedral (I_h) symmetry of the target, including the a_g, a_u, t_{1g}, t_{1u}, t_{2g}, t_{2u}, g_g, g_u, h_g and h_u components. The spherical dipole polarisability is $558.0a_0^3$ and the close-coupling (CC) approach is used to calculate total cross sections for positron-C_{60} scattering below 6 eV.

Figures 7.1.2 and 7.1.3 show the results of this model for both V_{ECP} and V_{PCP} where the labelled peaks seen in the calculated cross sections represent the components of the V_{CP} expansion which contribute to the resonances. The V_{ECP} model indicates a generally flat total cross section with a resonance feature at 3.238 eV (figures 7.1.2a-b)). This is due to the a_g component and represents a relatively long lived resonance, where the positron becomes temporarily trapped inside the C_{60} cage structure, lasting $\sim$0.5 ps before decay via positron ejection or annihilation. The feature is narrow with a full width half maximum (FWHM) of 8.8 meV, but has a large magnitude, more than 10% above the background cross section.

The V_{PCP} model turns the a_g resonance into a bound state, e^+C_{60}, and produces additional resonances in a similar energy region (shown in figures 7.1.3a-b) due to the stronger V_{CP} potential. Resonances t_{1u} (0.02 eV) and h_g (3.8 eV) are due to the positron becoming trapped inside the cage, whereas resonances t_{2u} and g_u (0.5 eV) and g_g and h_g (1.5 eV) are resonances where the positron is outside the cage, trapped behind angular-momentum barriers. The h_g resonance at 3.5 eV has an magnitude $\sim$7% above the background total cross section and is $\sim$200 meV FWHM (implying a shorter-lived resonance).

Overall, there is a large discrepancy in the magnitude of the total scattering cross section between the V_{ECP} and V_{PCP} models.

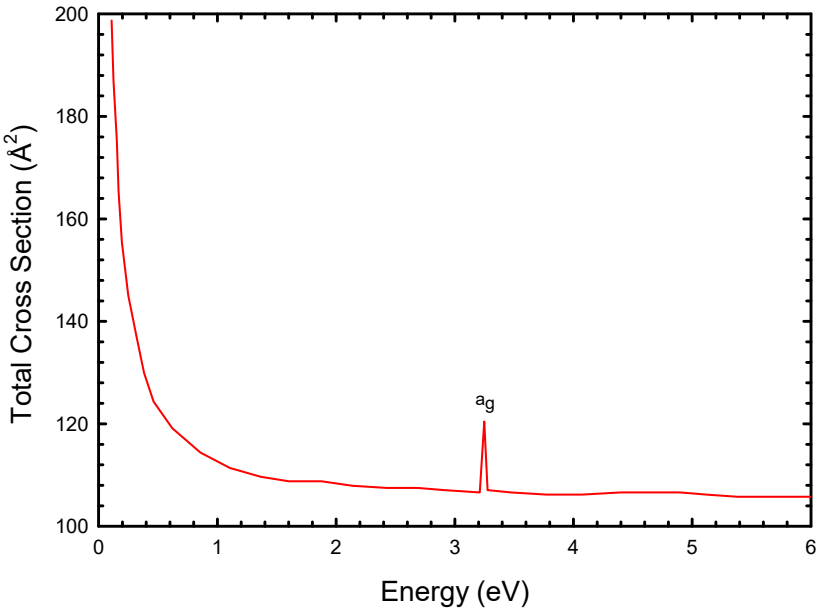

(a)

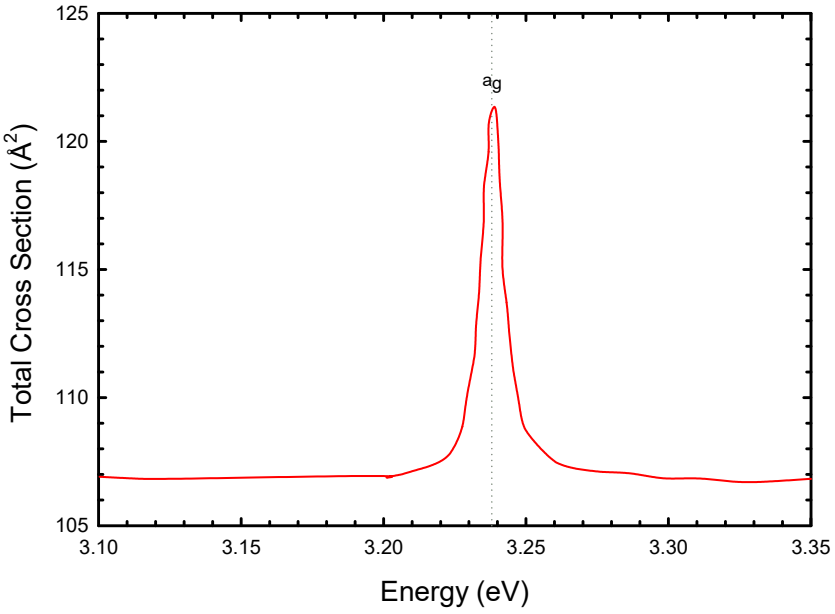

(b)

Figure 7.1.2: Model from Gianturco and Lucchese (1999) using V_{ECP}. Labels indicate the components responsible for the features in the total cross section and the dotted line in b) shows the feature is centred at 3.238 eV.

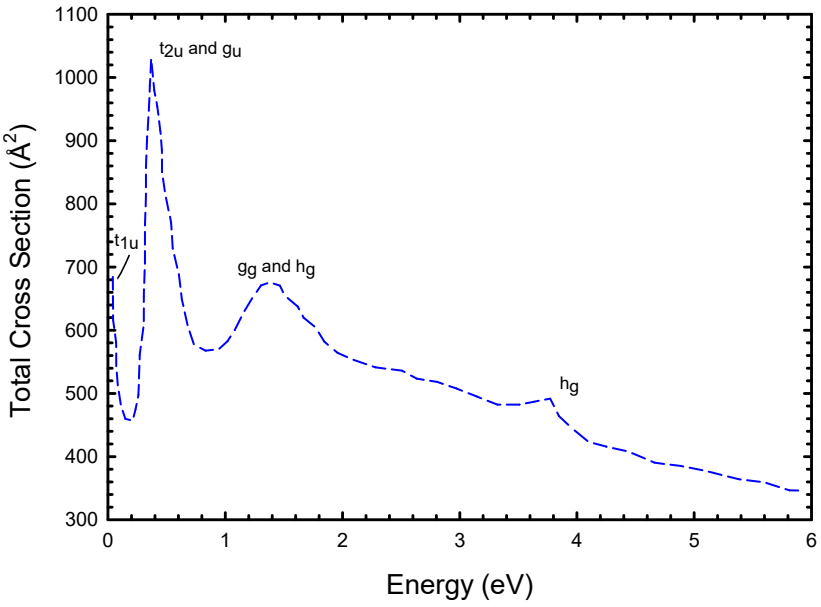

(a)

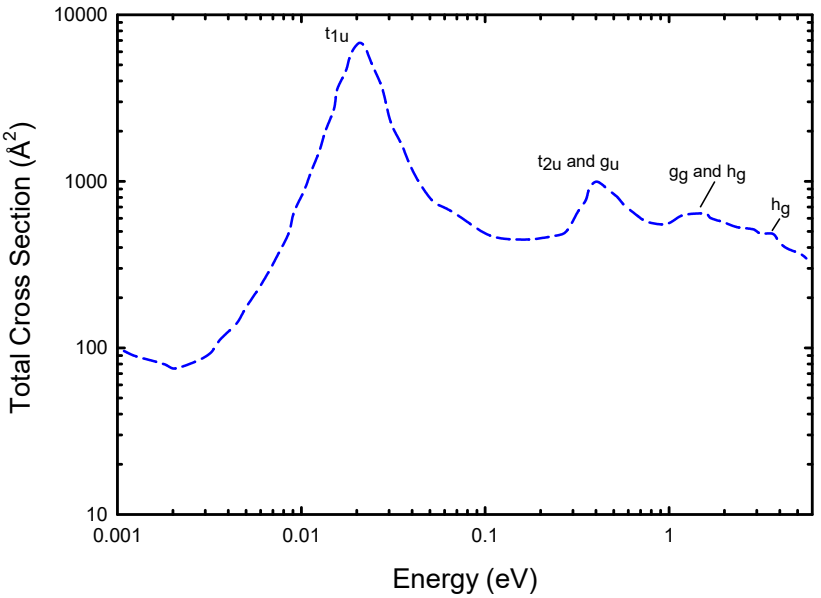

(b)

Figure 7.1.3: Model from Gianturco and Lucchese (1999) using V_{PCP}. Labels indicate the components responsible for the features in the total cross section.

Since the data presented in this chapter was collected, there have been further theoretical calculations conducted by Hervieux et al. (2017), investigating positronium formation from C_{60} molecules. These calculations predicted trains of resonances in the positronium formation cross section. However, since these predictions were not completed before the experiments presented here, they have not been considered further.

Motivated by these predictions, which indicate sufficiently large resonant features at experimentally achievable energies and energy resolutions, a series of experiments were conducted to investigate whether these were observable in the experimental total and Positronium formation cross sections for scattering of positrons from C_{60} molecules. The measurements presented focus on the energy range from 0.5 to 10 eV.

7.2 Experimental Details

The measurements presented in section 7.3 were performed using the oven configuration detailed in section 3.2 at a transport energy of 80 eV. The energy spread was ∼70 meV and V_m was 100 meV. The resulting missing angles at scattering energies from 0.4-50 eV are shown in table 7.1. The temperature of the oven was ∼400°C (∼673 K), ensuring the percentage of positrons scattering from the target is ≤10 %.

Energy (eV)	$\boldsymbol{\theta_{min}}$ (°)
0.4	30.0
1	18.4
2	12.9
5	8.1
10	5.7
20	4.1
30	3.3
50	2.6

Table 7.1: Missing angles at selected scattering energies for $V_m = 100$ meV

7.2.1 Vapour Pressure

In order to extract the pressure of C_{60} inside the scattering cell, measurements of the temperature of the cell were made and vapour pressure curves used for com-

parison. There have been several measurements of the vapour pressure curves for C_{60}, with the most recent performed by Popović et al. (1994) and Piacente et al. (1995). Both papers note that if the sample is impure, there can be significant effects on the specific vapour pressure curves measured.

Popović et al. (1994) measured the vapour pressure curves for C_{60} at temperatures from ∼650 to 780 K using mass spectrometry to analyse the effusing gas from a Knudsen cell. It was noted that as the temperature rose above 700-740 K, the vapour pressure measured was lower than expected and transmission electron microscopy indicated partial decomposition of the C_{60}. This behaviour was attributed to the presence of solvents in the original sample, and it was found that in the absence of any solvents there was no decomposition. The relationship between pressure, p, and temperature, T, was determined to be

$$\log p = 10.49 \pm 0.14 - \frac{8276.4 \pm 120}{T} \tag{7.2.1}$$

where the pressure and temperature are in kPa and K respectively and the numbers after the ± refer to the uncertainties in the constants.

Piacente et al. (1995) used a torsion effusion method to determine the vapour pressure curves for C_{60} at temperatures from 730-990 K. The C_{60} sample was placed in a cell with effusion holes on opposite side walls. The cell was suspended under vacuum from a torsion wire and moved into the isothermal region of the furnace used for heating. As the C_{60} gas exited the cell a torque was produced which was measured directly and is proportional to the C_{60} pressure. A series of different cells with different effusion holes were employed for comparison and to accurately determine the constant of proportionality between the pressure and temperature. Piacente et al. (1995) observed similar behaviour to Popović et al. (1994) and noted that the first data runs performed produced higher vapour pressures than those taken later, using the same samples. Investigation of the samples using scanning electron microscopy indicated that the change in vapour pressure was most likely due to initial impurities in the sample, rather than decomposition of the C_{60} itself. Two equations were determined, the first for initial samples containing impurities and the second for later samples where the impurities have been removed following heating and cooling. These are

$$\text{First Run: } \log p = 8.28 \pm 0.20 - \frac{9154 \pm 150}{T} \tag{7.2.2}$$

$$\text{Second Run: } \log p = 8.73 \pm 0.25 - \frac{9668 \pm 200}{T} \tag{7.2.3}$$

where, as before, the pressure and temperature are in kPa and K respectively.

Figure 7.2.1 shows equations 7.2.2 and 7.2.3 plotted as a function of temperature. In these experiments, a similar phenomenon to those noted in Popović et al. (1994) and Piacente et al. (1995) was observed where later runs produced a lower vapour pressure at equivalent temperatures to earlier runs. The scattering percentage (the percentage of positrons which scatter from a C_{60} molecule), in figure 7.2.1 is estimated assuming the total scattering cross section at 6 eV is 106Å (Gianturco and Lucchese, 1999), note that this is from the V_{ECP} model, if the V_{PCP} model is used the scattering percentages are much higher. Based on these predictions, there could be a difference of $\sim 15°C$ in the temperatures from the two models to achieve the same vapour pressure inside the oven.

The differences between the two vapour pressure curves presented make it more challenging to ascertain an absolute magnitude for cross section measurements, as the target pressure is part of these calculations. In order to select one of the vapour pressure curves, a number of preliminary measurements were made by altering the oven temperature and measuring the positron scattering percentages (the percentage of positrons which interact with the target). For example, using the vapour pressure curve shown in equation 7.2.1 indicates that the required temperature to produce 1 to 10% scattering is $\sim 200 - 220°C$, using the lower magnitude V_{ECP} model. Preliminary measurements observing the intensity of the positron beam at different oven temperatures indicated no decrease in beam intensity at these temperatures, corresponding to no target pressure in the oven. However, when the oven temperature was increased to the temperatures predicted by Piacente et al. (1995) a decrease in beam intensity and thus scattering was observed suggesting that in this experiment, the vapour pressures predicted by Piacente et al. (1995) were more applicable. Thus, the model provided by Piacente et al. (1995) was chosen for analysis over that of Popović et al. (1994) as it corresponded better to preliminary measurements. All data presented in section 7.3 was analysed using equation 7.2.3, corresponding to later data runs where the relationship between the temperature and pressure was constant.

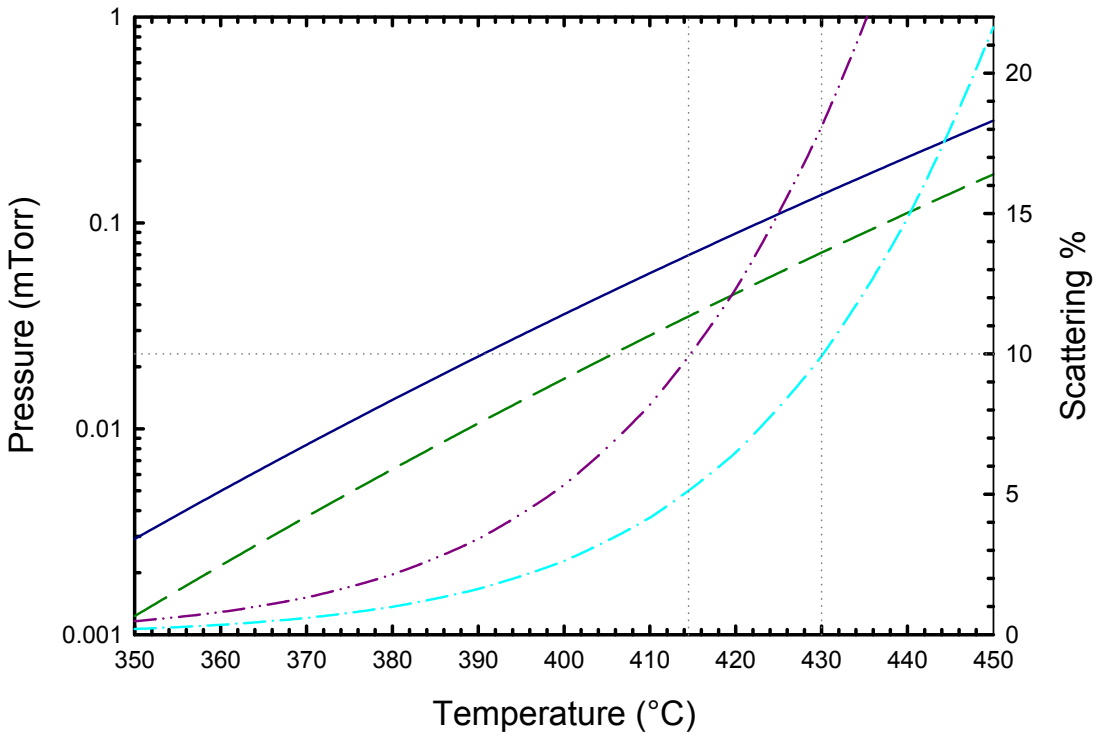

Figure 7.2.1: Relationship between the temperature and vapour pressure using equations 7.2.2 and 7.2.3 (Piacente et al., 1995) and estimation of the scattering percentages at 6 eV, assuming the total scattering cross section is 106Å consistent with Gianturco and Lucchese (1999) and the V_{ECP} model. Dotted lines indicate the temperature required for 10% scattering for the two pressure curves, — equation 7.2.2; - - - equation 7.2.3; – ·· – percentage scattering for equation 7.2.2; – · – percentage scattering for equation 7.2.3

Figure 7.2.1 also highlights the effect that a small change in temperature can have upon the scattering percentage and thus the cross section. The uncertainties in equation 7.2.3 lead to large uncertainties in the pressure measurement, even if the temperature uncertainty is very low. For an equation with the general form

$$\log p = A - \frac{B}{T} \tag{7.2.4}$$

where A and B are constants with errors δ_A and δ_B, and T is the temperature with error δ_T. The error in the pressure is given by

$$\delta_p = p \ln(10) \delta_{\log p} \tag{7.2.5}$$

where

$$\delta_{\log p} = \sqrt{\delta_A^2 + \left(\frac{B}{T}\right)^2 \left(\left(\frac{\delta_B}{B}\right)^2 + \left(\frac{\delta_T}{T}\right)^2\right)} \tag{7.2.6}$$

In the case of equation 7.2.3, this equates to δ_p ∼87-95% in the temperature range 350-430°C when $\delta_T = 0$. The errors in the determination of the constants δ_A and δ_B are the predominant sources of error in this experiment. Therefore, the systematic error in the total cross section for the results presented was ∼90%, although it should be noted that this is the systematic error for equation 7.2.3 and if the vapour pressure of Popović et al. (1994) were used the cross section magnitudes would be significantly different. The statistical error bars range from ∼1-10% for the total cross sections and from ∼6-50% for Ps formation cross sections, although most are closer to ∼25%. Given these large, unavoidable systematic errors due to our uncertainty in the pressure, the absolute magnitude of the cross sections cannot be confidently determined. However, resonant features should appear as a change in the relative cross sections and therefore should still be visible regardless of the absolute magnitude of the cross section.

7.3 Results

The total cross sections for scattering energies of 0.4-6 eV are presented in figure 7.3.1, this covers the energy range investigated in Gianturco and Lucchese

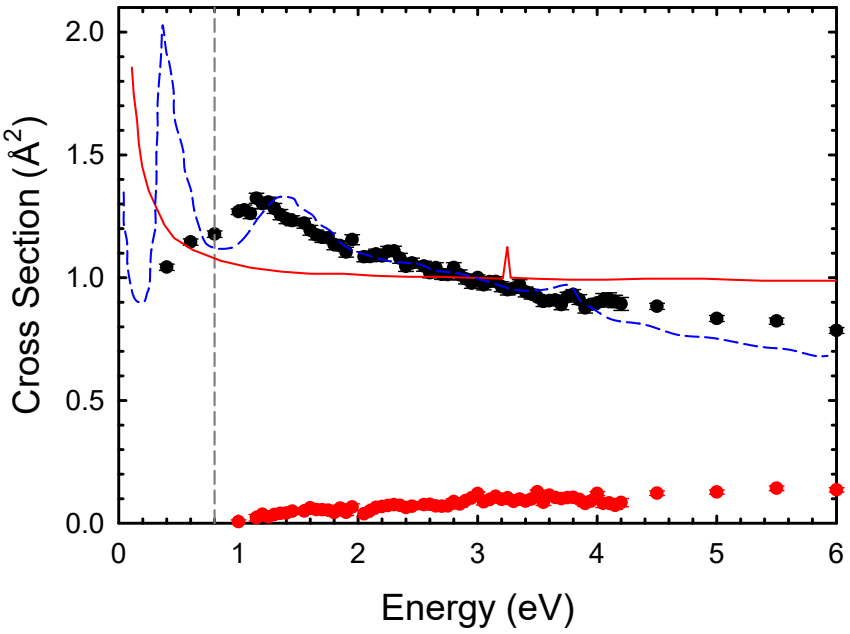

(a) 0.4 to 6 eV

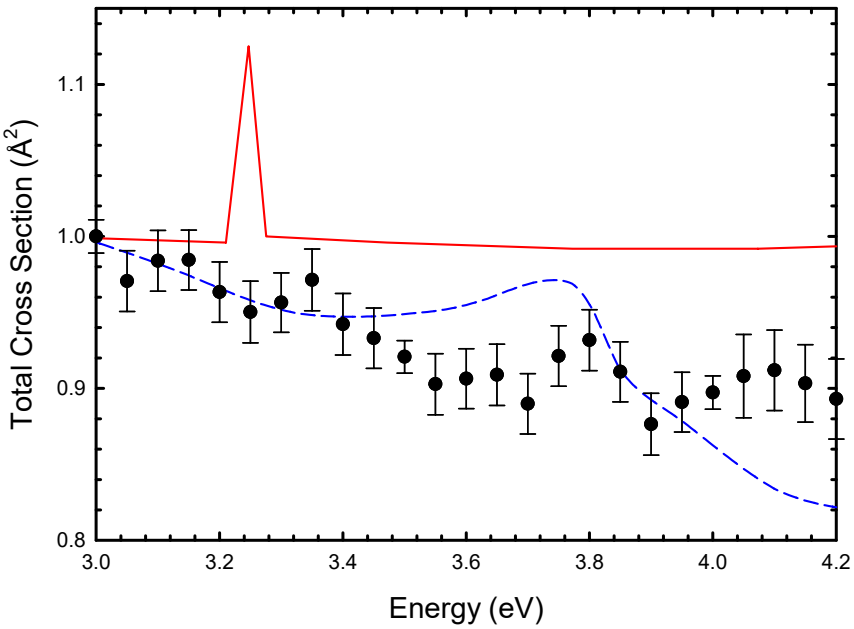

(b) 3 to 4.2 eV

Figure 7.3.1: a) Total scattering cross sections from 0.4 to 6 eV. b) Total scattering cross sections from 3-4.2 eV. • Present total; — V_{ECP}, - - - V_{PCP} scaled to match present total cross section at 3 eV (Gianturco and Lucchese, 1999).

(1999). Due to the large systematic uncertainty in the pressure measurement, it is not possible to determine which of the two models proposed by Gianturco and Lucchese (1999) describe the magnitude of the total cross section best, therefore the measured total cross sections and theoretical calculations have been normalised to 1 at 3 eV for comparison purposes. It is clear that the V_{PCP} model, which explicitly incorporates the positron in the calculation of the potential, generally agrees well with the energy dependence of the total cross section, although there is some discrepancy above 4 eV. However, agreement with the energy dependence of the V_{ECP} model is very poor.

Below ∼1.2 eV, the measured total cross section appears to decrease. Positron scattering from large molecules tends to display a rapid increase in the total cross section at low energies due to a strong dipole polarisability. This also leads to a very forward peaked DCS, meaning that the 'missing' part of the total cross section becomes very large as well. For comparison, the dipole polarisabilities for tetrahydrofuran (THF) and pyrimidine are 47.08 a.u. and 59.3 a.u. respectively and exhibit large increases in the total cross section at energies below a few eV (Chiari et al., 2013; Palihawadana et al., 2013). Both of these large molecules also have strong forward peaked DCSs, such that for THF at an incident positron energy of 1 eV and with a missing angle of 20°the total cross section was underestimated by 40% (Chiari et al., 2013). Therefore, if the total cross sections for these molecules is uncorrected, the cross section can appear to decrease at low energies due to the angular resolution of the experiment.

C_{60} has a very high spherical dipole polarisability of 558.0 $a.u.$[3] (Pederson and Quong, 1992), thus it is reasonable to expect the DCS to be strongly forward peaked at a few eV. The missing angles, shown in table 7.1, also increase as the energy is reduced. Therefore, the decrease observed in the measured total cross section could be due to the angular resolution of the experiment, in the absence of theoretical or experimental DCSs it is not possible to account for the underestimation of the total cross section. Alternatively, the drop could be due to the large g_g and h_g resonance as predicted by the V_{PCP} model, or a combination of missing angles and a resonance.

Figure 7.3.2 shows the total and Ps formation cross sections up to 50 eV. The total cross section continues to decrease as the energy rises from 6 to ∼10 eV, before levelling off. The Ps formation cross section increases quickly above threshold, shown in figure 7.3.2b, and is effectively constant above ∼5 eV, contributing

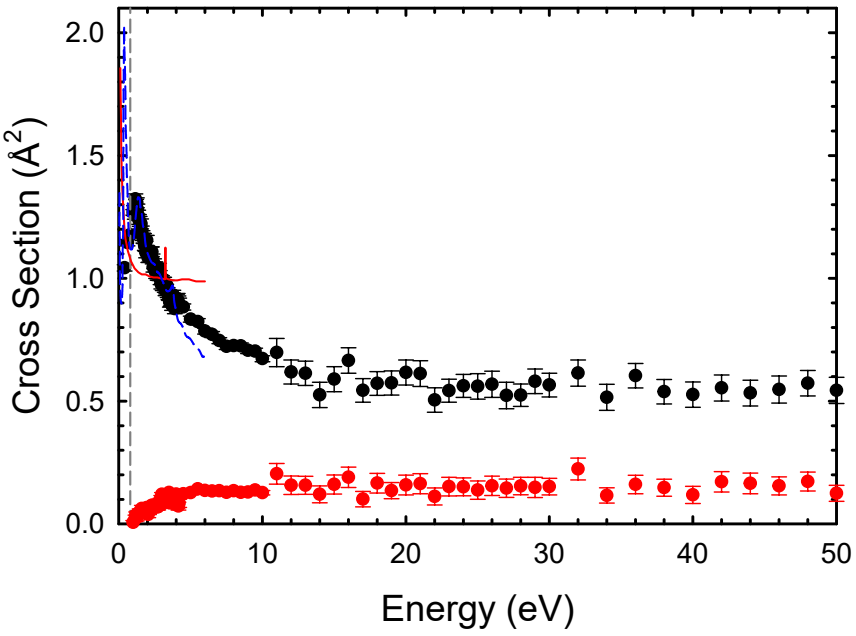

(a) Total

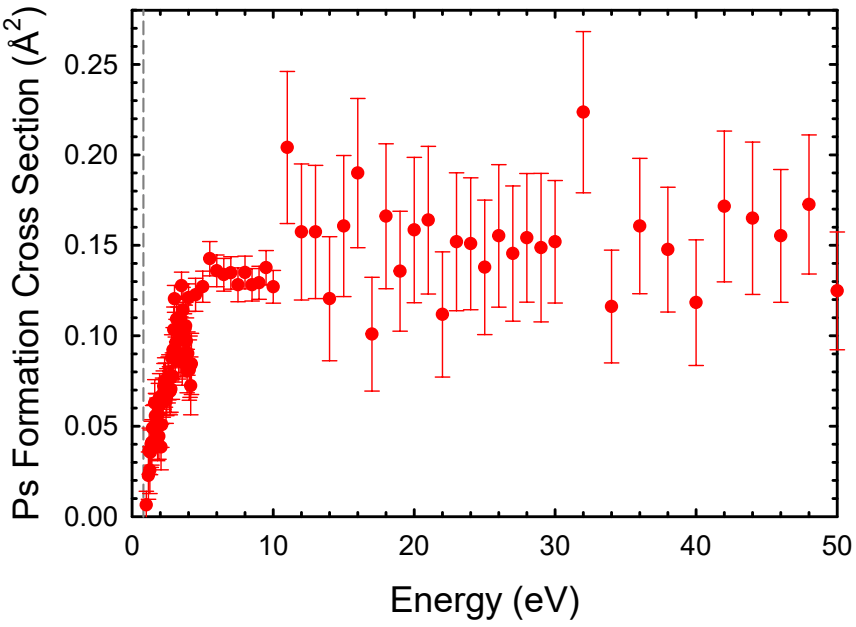

(b) Positronium

Figure 7.3.2: Long range total and Ps formation scattering cross sections. • Present total cross section; • Present Ps formation cross section; — V_{ECP}, - - - V_{PCP}, from Gianturco and Lucchese (1999). The total cross sections are scaled to 1 at 3 eV. Dotted line indicates Ps formation threshold at 0.8 eV.

approximately 16% of the total scattering at 50 eV. The error bars are larger for incident energies greater than 10 eV due to fewer scans made in this region. This was due to technical issues, limiting the amount of time available to collect data.

Finally, figure 7.3.1b shows the total cross section in the energy range 3-4.2 eV, in the region of the predicted resonances at 3.238 eV (a_g, model V_{ECP}) and 3.5 eV (h_g, model V_{ECP}). As noted before, the model produced using V_{ECP} is a very poor description of the experimental data and the resonance at 3.238 eV is not visible. There is also no clear indication of a resonance at 3.8 eV.

In conclusion, the current results do not provide any conclusive evidence of resonant features in the total or Positronium formation cross sections at the predicted energies. The V_{PCP} model, which describes the relative shape of the experimental data better than the V_{ECP} model, predicts smaller resonant features than the V_{ECP} model. Given the size of the statistical error bars in the current data, and the size of these predicted resonances, it is not possible to completely disregard the predictions. Additional data would need to be collected to reduce the statistical error bars and future experiments should initially focus on the energy region from 3-4.2 eV as this region was less affected by concerns with the missing angles. If the energy spread of the beam can be improved, it may be possible to access the energy region below 2 eV where the magnitudes of the predicted resonances are very large.

Chapter 8

Results III: Positron Impact Ionisation of argon

In this chapter, I will present the first results from the positron reaction microscope at the Australian National University, which focused on single ionisation of argon atoms by positron impact, collected over 2013 and 2014. I operated the experiment in 2013 with support from Simon Armitage and Dennis Mueller of the University of North Texas, and lead the data collection in 2014. I analysed data from both years using the analysis code I developed as discussed in chapter 5. Here, alongside presenting the results, I will also discuss the reliability of the fitting routines employed.

8.1 Introduction

Single ionisation of atoms by electron impact has been studied both theoretically and experimentally over several decades with triply differential cross sections (TDCS) provided by (e, 2e) experiments. These involve detection of the scattered and ejected (emitted) electrons following ionisation and were first conducted in the 60s by Ehrhardt et al. (1969), who investigated electron impact single ionisation of helium. Over the next few decades, other (e, 2e) experiments were conducted, enhancing our understanding of the dynamics of the three-body Coulomb problem. However, these techniques were limited due to their small acceptance angle, making them poorly suited for the study of other multiple coincidence systems such as double ionisation, excitation-ionisation and molecular fragmentation. These small acceptance angles also made it challenging to develop

a 'benchmark' set of data for single-ionisation events over a range of electron ejection energies and angles. When applied to ion-impact ionisation events, it was only in 1994 that the first fully differential data was collected (Moshammer et al., 1994), and only a few measurements have been made for electron impact double ionisation (e, 3e) of helium (Taouil et al., 1998; Kheifets et al., 1999; Lahmam-Bennani et al., 2003).

The development of the reaction microscope overcame many of the limitations of the more 'conventional' methods (Ullrich et al., 2003), giving access to almost all final-state momentum space for multiple events. In some cases, the application of these methods threw previously accepted theoretical treatments into question, for example, the work of Schulz et al. (2003) into fast ion induced single ionisation of helium were in substantial disagreement with the theory of the time, including in scattering geometries that had been previously inaccessible. On the other hand, not all reaction microscope experiments have yielded such disagreements between theory and experiment. For example, the first use of Recoil Ion Momentum Spectroscopy (RIMS), a pre-cursor to the modern reaction microscope, for electron impact single and double ionisation of helium (Jagutzki et al., 1996) was in good agreement with previous experimental measurements and current theoretical predictions. Reaction microscope techniques have the ability to extend our knowledge of complex scattering systems, providing potential challenge to theory and expanding experimental data into scattering geometries previously unattainable.

The application of reaction microscope techniques to positron impact ionisation is a much more recent development. The results in this chapter are the first TDCS produced by the reaction microscope at the Australian National University and are focussed on single ionisation of argon atoms by positron impact.

At projectile energies of a few tens of electron volts, above the single ionisation threshold, 15.76 eV, the direct ionisation cross sections for positrons and electrons are markedly different (figure 8.1.1). However, by $\sim$190 eV the cross sections are within 10% of each other. At this projectile energy, Ps formation, which is a substantial part of the total cross section at lower energies, is negligible. Despite the similarity in cross section magnitude, the dynamics of single ionisation of the target atom by positron or electron collision is expected to be significantly different.

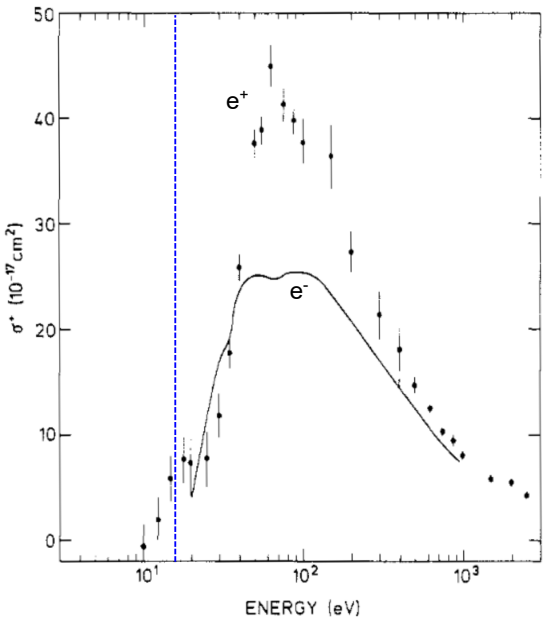

Figure 8.1.1: Comparison of positron (•) and electron (− − −) single ionisation of argon. - - - indicates the ionisation threshold. Adapted from Knudsen et al. (1990).

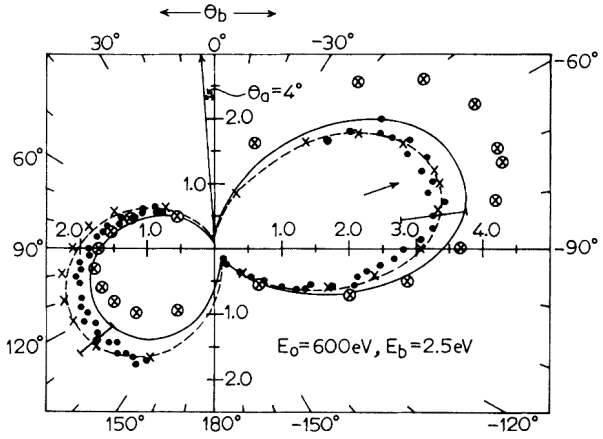

Figure 8.1.2: Example of theoretical TDCS in units of $10^{-22}m^2sr^{-2}eV^{-1}$ for ionisation of helium by electrons (x) and positrons (⊗) for 600 eV projectiles, 2.5 eV ejected electrons and a projectile scattering angle of 4°. The ejected electron angle is θ_b, and the arrow indicates the momentum transfer direction. −− − and − − − are theoretical results using different models for electron scattering and • are experimental results for electron scattering. Reproduced from Sharma and Srivastava (1988).

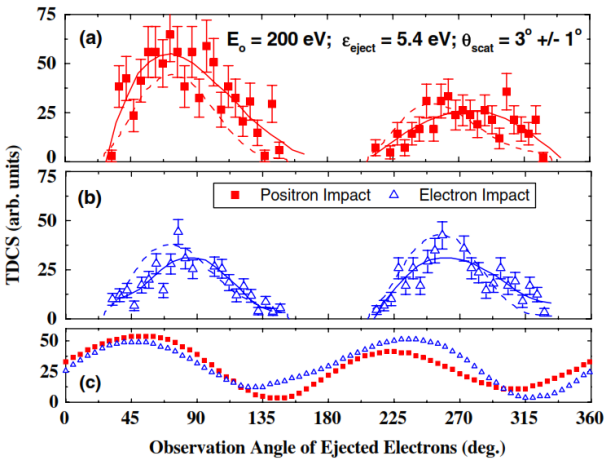

Figure 8.1.3: TDCS for single ionisation of argon by 200 eV positrons (a) and electrons (b), 5.4 eV ejected electron energy and 3° positron scattering angle. ■ Positron impact; △ Electron impact; —, — polynomial fits to the positron and electron data respectively; - - -, - - - CDW-EIS theory from c) convoluted with experimental parameters for positron and electron data respectively. c) CDW-EIS theory. Reproduced from De Lucio et al. (2010).

Theoretical models (Sharma and Srivastava, 1988; Brauner and Briggs, 1993; Berakdar et al., 1993) show differences in the dynamics of the ionisation event between positron and electron scattering. This is most apparent when considering the binary peak, where the ejected electron does not interact with the recoil ion, and the recoil peak, where the ejected electron scatters in the potential of the recoil ion. As shown in the examples in figures 8.1.2 and 8.1.3, the binary peak is enhanced for positron scattering and there is some shift in the direction of the binary and recoil peaks with respect to the momentum transfer direction.

8.2 Experimental Details

The results from two different data runs are presented in the following sections, these were collected in 2013 and 2014. In order to ensure that they were comparable, certain key elements were kept the same during both runs. The positron beam energy was 190 eV, selected as the single ionisation cross section is high at this impact energy and the Ps formation cross section is negligible (see figure 8.2.1). The magnetic field in the reaction microscope was 10 G and the

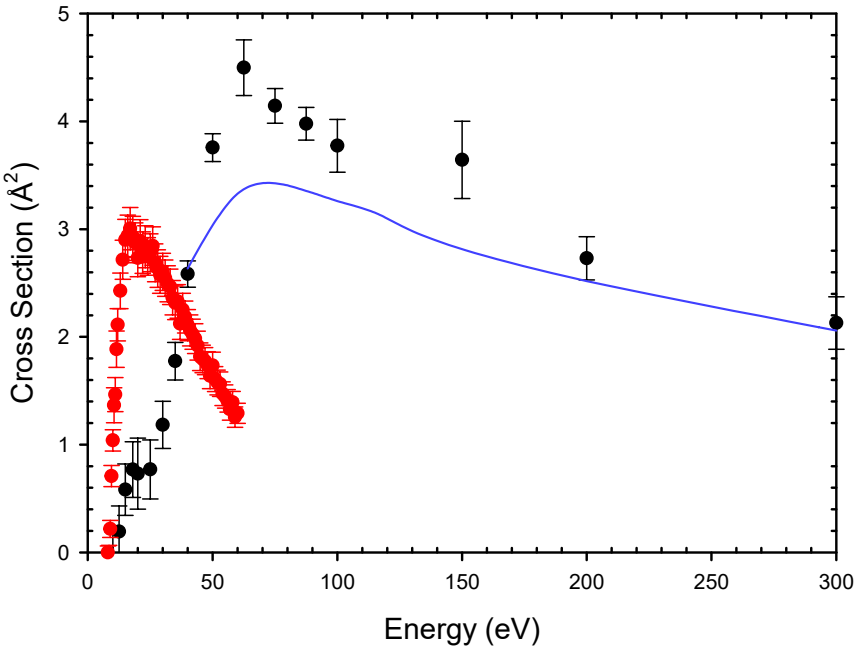

Figure 8.2.1: Positron impact single ionisation of argon as a function of impact energy, compared with the Ps formation cross section. • Experimental single ionisation data of Knudsen et al. (1990); — Theoretical single ionisation calculation of Campeanu et al. (1996); • Experimental Ps formation cross sections of Jones et al. (2011)

extraction field, U_{ex} was 6.262 V/cm. The moderated beam was used in both cases without the trap to improve the beam intensity.

One difference between the two runs was the focus upon the alignment of the magnetic field in the reaction microscope. It proved to be significantly challenging in the 2013 run to guide the positron beam along the beamline and through the 2 mm aperture into the reaction microscope. In order to direct the beam through the aperture, the Helmholtz coils near the aperture were tilted to guide the beam into reaction microscope. As these coils sit only at the entrance to the reaction microscope, the impact of their field on the interaction region was considered to be negligible. Alignment of the Helmholtz coils in 2013 ensured that the unscattered beam passed through the centre of the positron/ion detector, but in order to achieve this the coils were no longer geometrically aligned with the chamber.

In 2014, beam intensity was sacrificed to keep the Helmholtz coils aligned with the chamber. This should provide the most homogenous magnetic field inside the reaction microscope. Without moving the Helmholtz coils, the unscattered positron beam impacted the positron/ion detector resulting in more data collected, but also more data which was discounted as it did not include the necessary ion and ejected electron information. As the beam intensity was relatively low, there were no concerns about damage to the detector MCPs from the unscattered positron beam.

It was noted during initial analysis of the 2014 data that the small difference in location of the Helmholtz coils had little effect on the observed relationships between the scattered positrons and ejected electrons. The key difference between the data sets was that there was a smaller acceptance angle for the scattered positrons in 2014 as there was no longer a limitation posed by the hole in the positron/ion detector.

Improvements made to the electronic selection of events meant that the 2014 data set contains more counts than the 2013 set, despite running with a lower initial beam intensity.

8.3 Analysis of Results

As the data runs from 2013 and 2014 were run with different configurations of the beam, it is important to discuss the results from each year individually. Time

spectra are useful for comparison as they have not been processed by the fitting program (see section 5.4.6), yet contain important information especially relating to the longitudinal momentum of the particles. The relative positron-ion time, t_{e^+ion}, is used in this analysis only as a selection criterion for potential candidates relating to single ionisation. Therefore, only the relative positron-electron time, $t_{e^+e^-}$, is of interest here. Figure 8.3.1 shows a comparison of $t_{e^+e^-}$ for the 2013 and 2014 data sets, prior to momentum reconstruction. Both data sets include a peak at around 75 ns, where this peak includes fewer counts for the 2013 data as there were fewer events in the 2013 data set. The two data sets exhibit a large peak around 30 or 40 ns for 2013 and 2014 data respectively. The shift cannot be explained by time delays in the experimental setup as, in both cases, the time delays were identical.

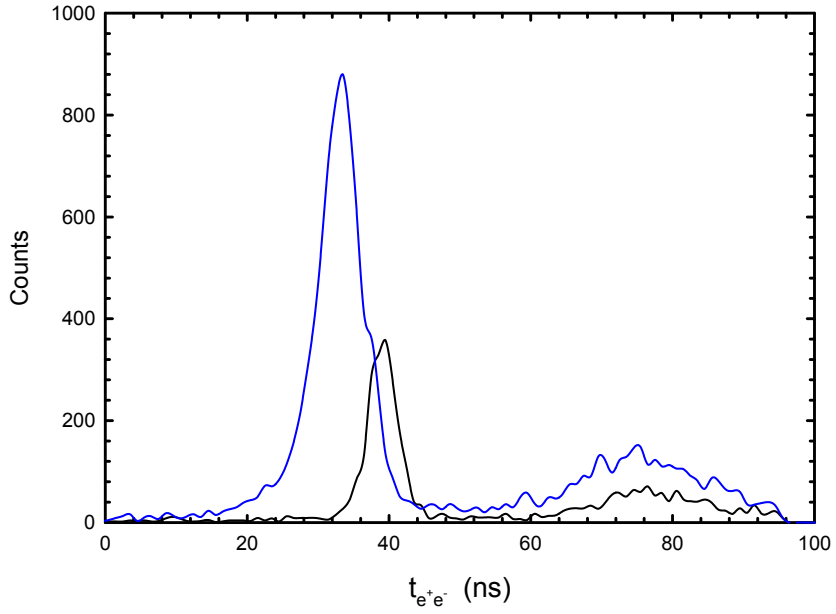

Figure 8.3.1: $t_{e^+e^-}$ for 2013 and 2014, — all 2013 data; — all 2014 data

8.3.1 Model Reliability

It is physically possible for there to be events where $t_{e^+e^-}$ is around 30-40 ns, therefore, it is not valid to simply remove these events from the data sets without further consideration as this may also remove 'real' events associated with an ionisation event. However, if these events are not due to ionisation, it is unlikely

that the specific combination of times and detection positions will result in an event with a low fitting error, as defined by equation 5.4.8.

Events are selected to form a final data set if there is a single solution and the fitting error is low. Figure 8.3.2 demonstrates that the majority of events with both a unique fit and low error have $t_{e^+e^-}$ around 75 ns, whereas the events with multiple fits or those with unique fits, but high error, almost exclusively have $t_{e^+e^-}$ around 30 ns. This suggests that there is an experimental artefact producing a large number of events with $t_{e^+e^-}$ ∼30 ns. Here, it may be due to secondary electrons and is further discussed in section 8.3.2.

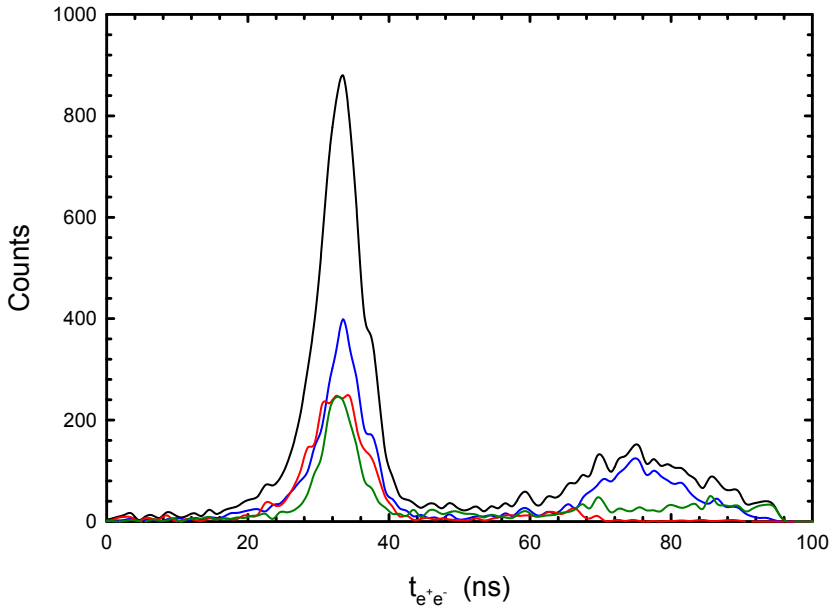

Figure 8.3.2: Comparison of unique and non-unique fits for $t_{e^+e^-}$ using data from 2014, — all data; — data with a unique fit and low error; — data with a non-unique fit; — data with a unique fit and high error

Figures 8.3.3 and 8.3.4 shows the effect of selecting only events with a unique fit and low error on the momenta. In particular, figure 8.3.3a indicates that the peak around 3 a.u. is predominantly due to 'good' fits with unique fits and low errors, whereas the peaks around 0.5 a.u. and -1 a.u. are a mixture of good and poor fits. Figure 8.3.3b shows that the peak around -0.6 a.u. may well contain a significant number of backscattered electrons and the sharp spike around 2.2 a.u. is most likely to be due to events with poor fits. Likewise, the sharp spike at ∼3.4 a.u. in figure 8.3.4b is also mostly due to events with poor fits. In both

figures 8.3.4a and 8.3.4b, selection of only well fitted events shifts the transverse momenta higher compared to the large, low momenta peaks for events with unique fits but high error.

It is clear that the well fitted events tend to describe behaviour more in line with expectations as discussed in section 8.1. The positron generally scatters at a low angle and keeps most of the longitudinal momentum, contributing only a small portion to the ejected electrons which are ejected in both forwards and backwards directions, but generally with a low momentum.

8.3.2 Secondary Electrons

One likely source of the $t_{e^+e^-}$ peak around 30 ns is the production of secondary electrons at grids in the reaction microscope. Secondary electrons can be produced by an electron, positron or ion impacting on a mesh grid and due to the extraction field this secondary electron may be accelerated towards the electron detector and produce a valid hit. These electrons may pass the selection criteria prior to momentum reconstruction as they are real particles, rather than noise, and appear at a reasonable time relative to the ion or positron. The shift in the $t_{e^+e^-}$ peaks in figure 8.3.1 from 40 to 30 ns between 2013 and 2014 could be caused by the movement of the unscattered positron beam between the years, resulting in a slightly different interaction region and a slightly different position of the secondary electron source. This should be investigated in future work (see section 10.2).

Figures 8.3.5 and 8.3.6 shows the momenta with good fits, where the data with $15 \leq t_{e^+e^-} \leq 45$ ns is included or excluded. Given the results of previous experimental and theoretical work (e.g. Sharma and Srivastava (1988); De Lucio et al. (2010)), it would be surprising if there is a strong electron ejection in the backwards direction. Figure 8.3.5b indicates that the backscattered electrons are almost exclusively due to the peak for $15 \leq t_{e^+e^-} \leq 45$ ns, which we tentatively refer to as a 'secondary electron' peak. The removal of the secondary electron peak also reduces the importance of the peaks at $\sim$0.6 and -1 a.u. in figure 8.3.5a and generally results in positrons and electrons scattered with lower transverse momenta in figures 8.3.6a and 8.3.6b.

Removing the secondary electron peak may remove real events with this relative time, but given the current experimental limitations it is not possible to

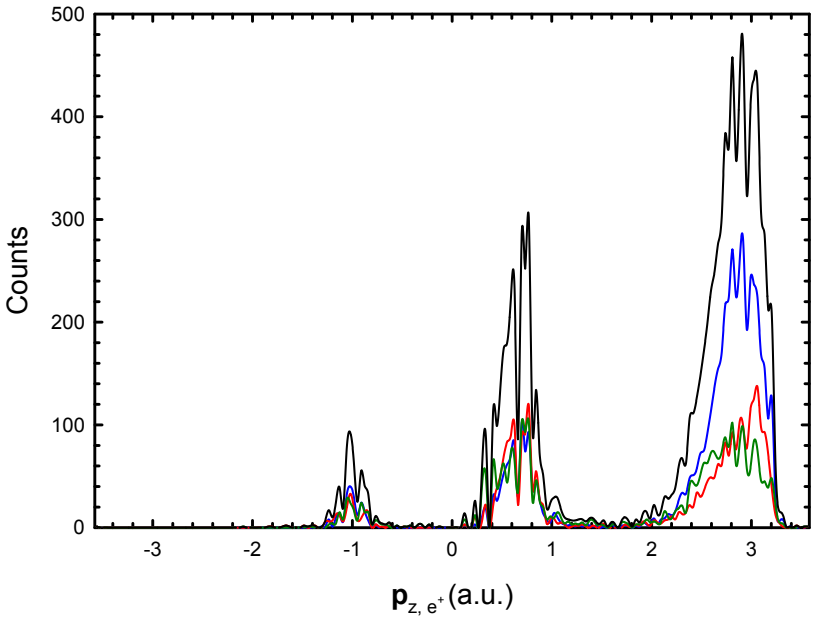

(a) p_{z,e^+}

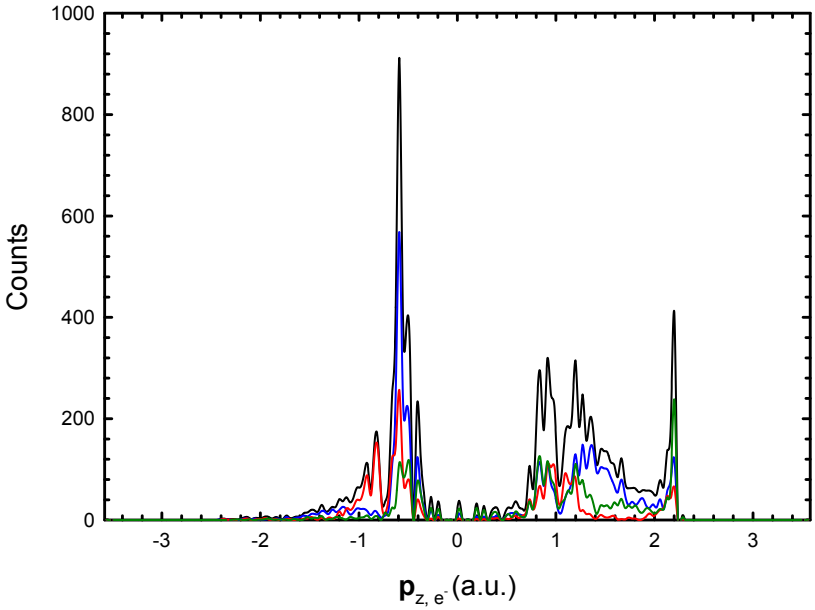

(b) p_{z,e^-}

Figure 8.3.3: Comparison of unique and non-unique fits for the longitudinal momenta using data from 2014. — all data; — data with a unique fit and low error; — data with a non-unique fit; — data with a unique fit and high error

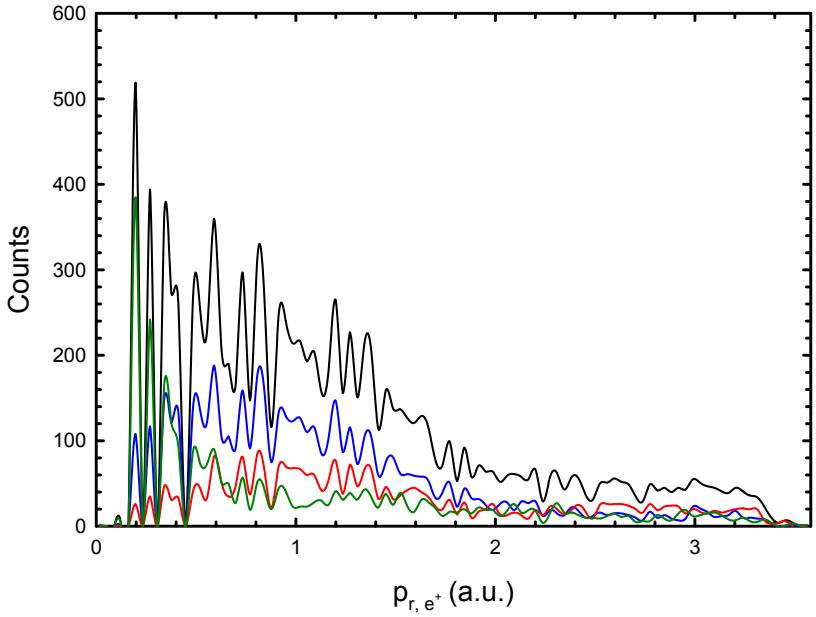

(a) p_{r,e^+}

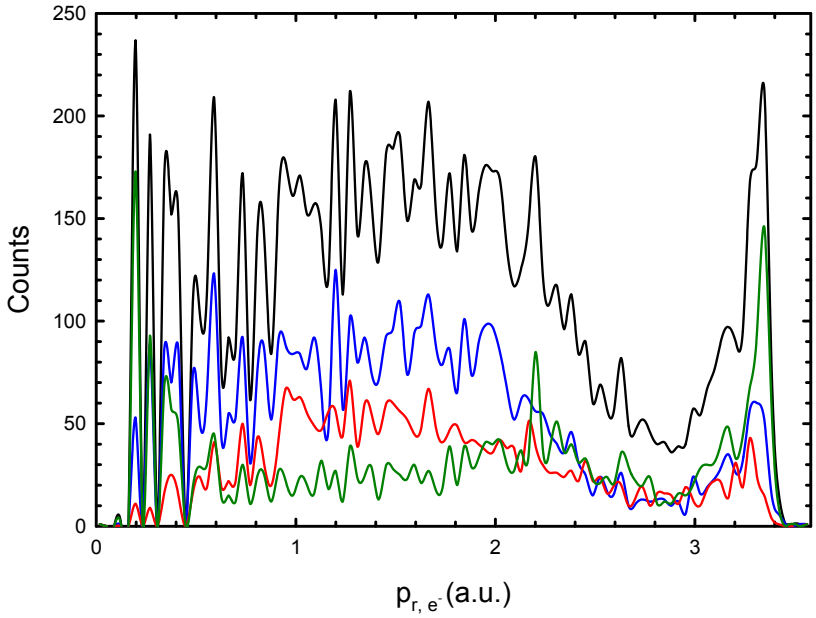

(b) p_{r,e^-}

Figure 8.3.4: Comparison of unique and non-unique fits for the transverse momenta using data from 2014. — all data; — data with a unique fit and low error; — data with a non-unique fit; — data with a unique fit and high error

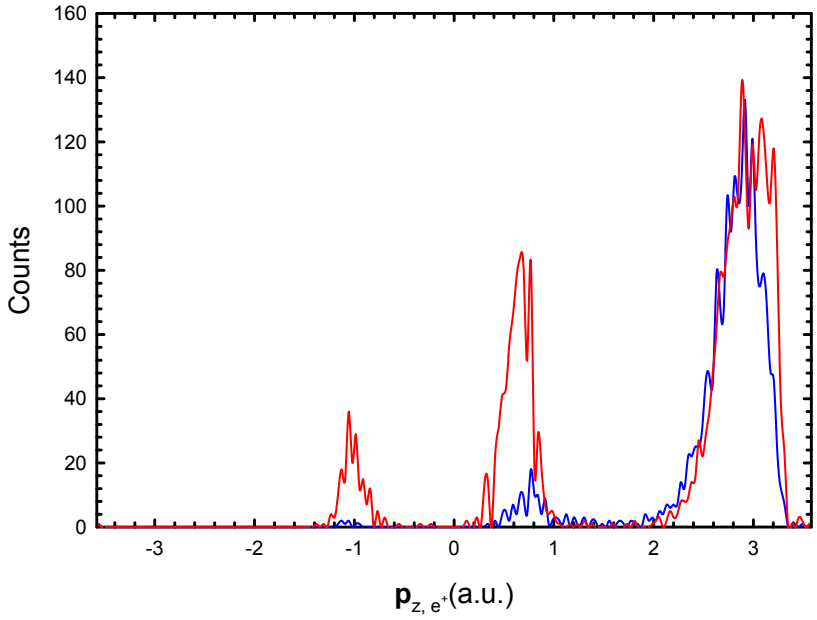

(a) p_{z,e^+}

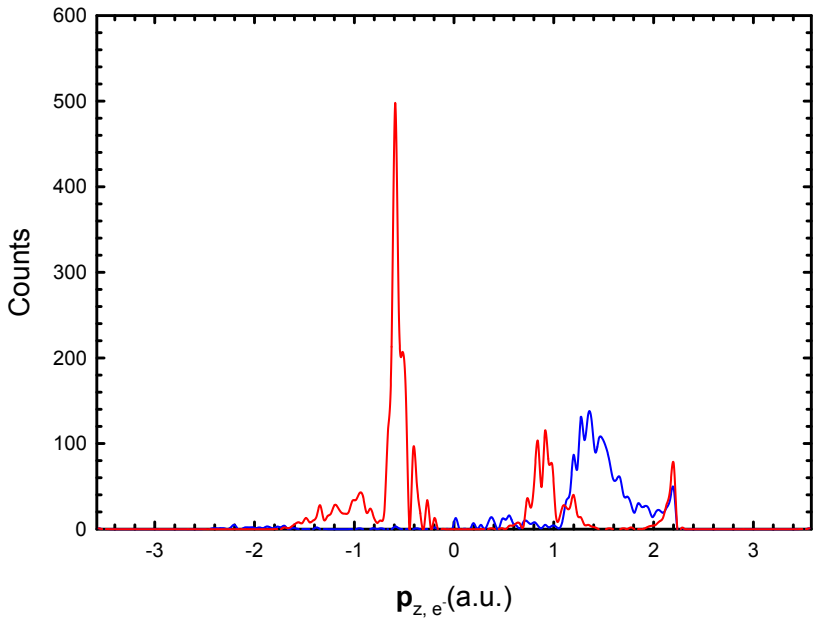

(b) p_{z,e^-}

Figure 8.3.5: Comparison of the longitudinal momenta using data from 2014 including or removing the apparent secondary electron peak. — data where $t_{e^+e^-}$<15 ns or $t_{e^+e^-}$>45 ns; — data where 15 ns$\leq t_{e^+e^-} \leq$45 ns

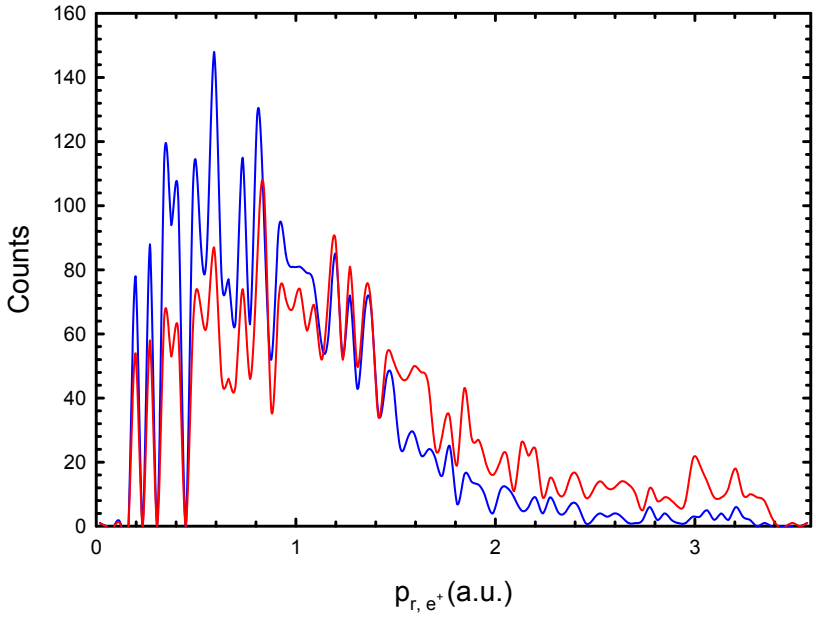

(a) p_{r,e^+}

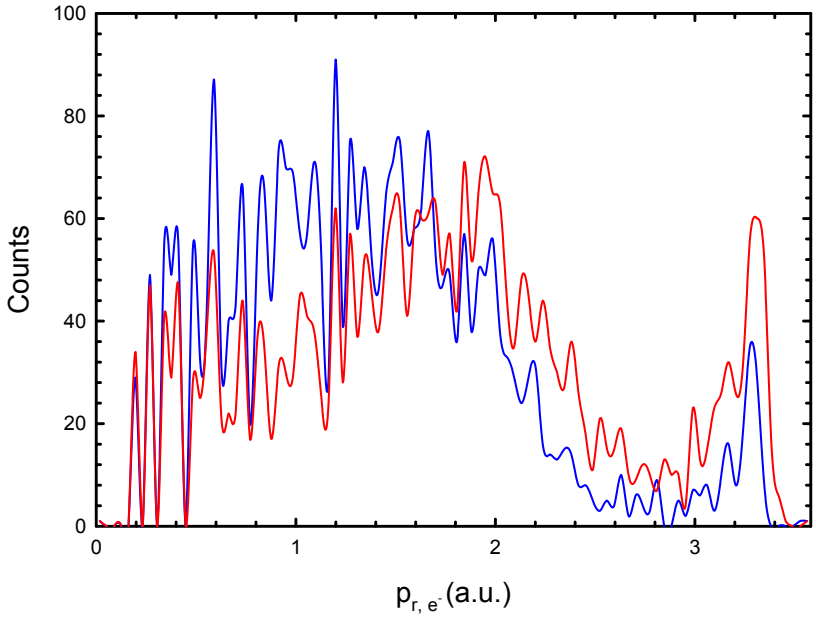

(b) p_{r,e^-}

Figure 8.3.6: Comparison of the transverse momenta using data from 2014 including or removing the apparent secondary electron peak. — data where $t_{e^+e^-}$<15 ns or $t_{e^+e^-}$>45 ns; — data where 15 ns$\leq t_{e^+e^-} \leq$45 ns

distinguish between secondary electrons and ejected electrons due to target ionisation. These real events could reveal interesting features in the TDCS and therefore, in the future, a focus would be to remove the secondary electron effects.

8.4 Results

The final results contain data where there is a unique fit with a low error and where the secondary electron peak has been removed. Figure 8.4.1 summarises the longitudinal and transverse momenta for both the positrons and electrons and data from 2013 and 2014. The longitudinal momenta (figure 8.4.1a) are very similar between the two data sets and indicate that the positron scatters with the majority of the initial momentum. The electron has a smaller momentum (approximately 50% that of the positron, see figure 8.4.2a) but is also predominately forward scattered. This is consistent with the expected enhancement of the binary lobe of the TDCS for positron scattering (Sharma and Srivastava, 1988).

The transverse momenta (figure 8.4.1b) of the positrons and electrons are lower than their longitudinal momenta and are more similar in magnitude. Figure 8.4.2b indicates that, overall, the electron has slightly less transverse momentum than the positron, as the peak in the ratio is <1. However, there are still a significant number of events where the electron has more transverse momentum than the positron. Figure 8.4.1b also shows that, compared to the 2013 data, the 2014 data shows a positron transverse momentum with a peak at a lower momentum. This is likely due to the change in the accepted scattering angle θ, in the $y-z$ plane. The 2014 experiment was conducted with the unscattered positron beam directed onto the positron/ion MCP plates, rather than through the aperture as in 2013. Therefore, more positrons scattered at a lower angle, and thus a lower transverse momentum, could be detected in 2014 than in 2013.

Figure 8.4.3 shows the θ dependence for positrons and electrons across the 2013 and 2014 data. In both data sets, there is a strong, well-defined peak in positrons $\sim 13^{\circ}$(2013) and $\sim 20^{\circ}$(2014) which extends up to $\sim 40^{\circ}$. This indicates that the majority of scattering for positrons is in the forward direction. The slight shift between the 2013 and 2014 data in the positron peak could be due to

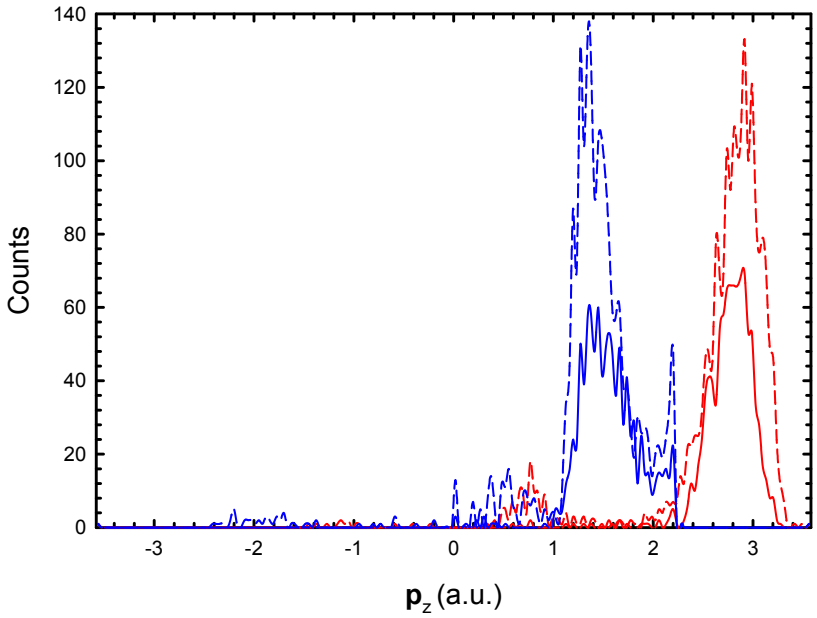

(a) Longitudinal Momentum

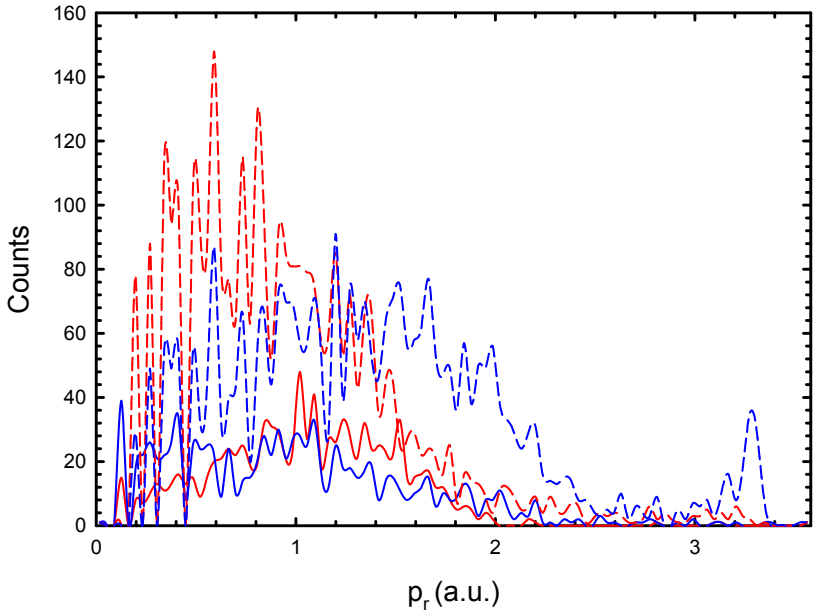

(b) Transverse Momentum

Figure 8.4.1: Longitudinal and transverse momenta for the positron and electron. — and — are the positron and electron momenta respectively for the 2013 data; - - - and - - - are the positron and electron momenta respectively for the 2014 data

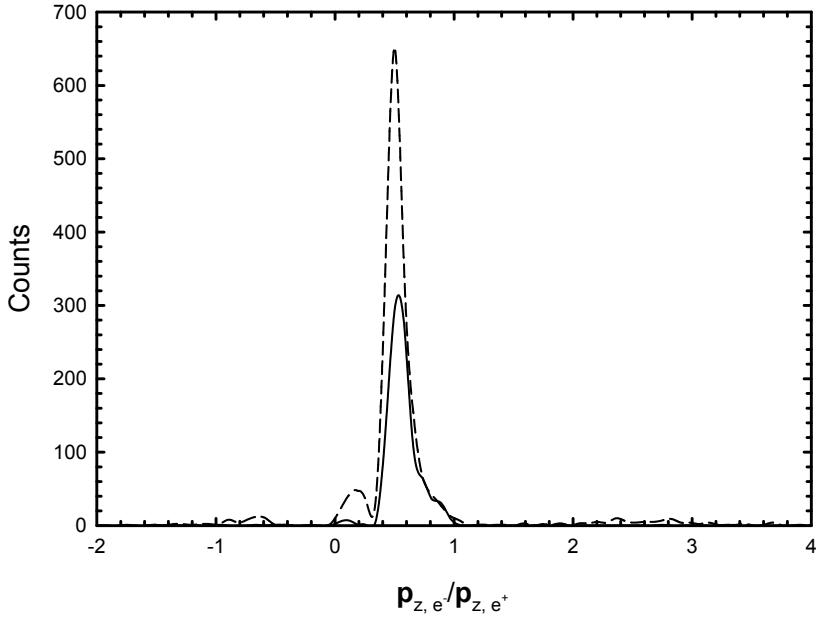

(a) Ratio of Longitudinal Momenta

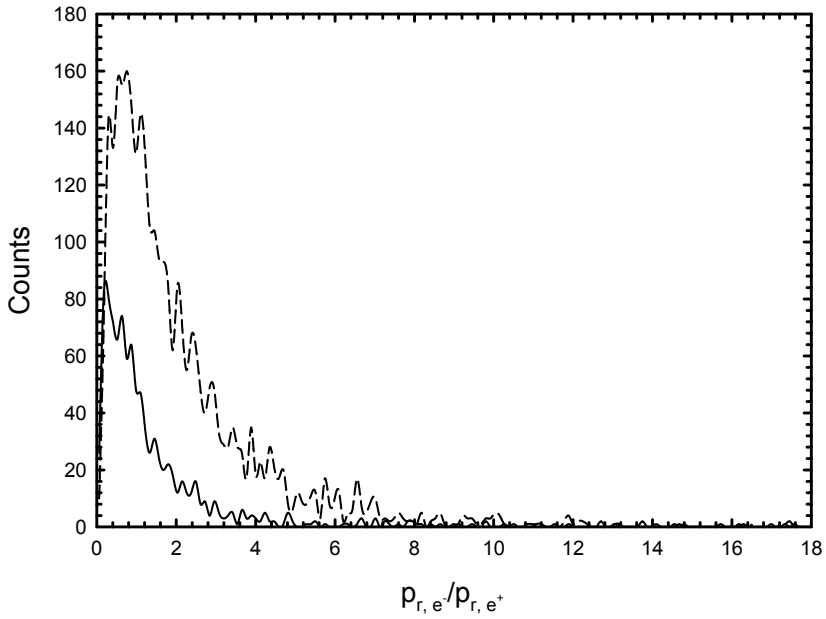

(b) Ratio of Transverse Momentum

Figure 8.4.2: Ratio of electron to positron momenta vectors. — 2013 data; - - - 2014 data

location of the unscattered beam in 2014, which represents an improvement in the low-angle limit of measurement.

Electrons, on the other hand, have a broader spread with a less defined peak with scattering angles of up to ∼80°. This wide spread of electron scattering angles is not dissimilar to the theory presented by Brauner and Briggs (1993) for positron-impact ionisation of Hydrogen atoms. Brauner and Briggs (1993) shows that for positrons scattered at small angles (4°), electrons are ejected in a forward direction. As the energy of the positron beam is increased to 150 eV, the electrons are ejected across a range from -40°to 100°, peaking at 20°. When the positron beam energy is increased further, the peak becomes more defined and shifts towards 0°. While this theory is not exactly representative of the experiment presented here, the general trend where electrons are ejected in an forward direction appears to be replicated in argon.

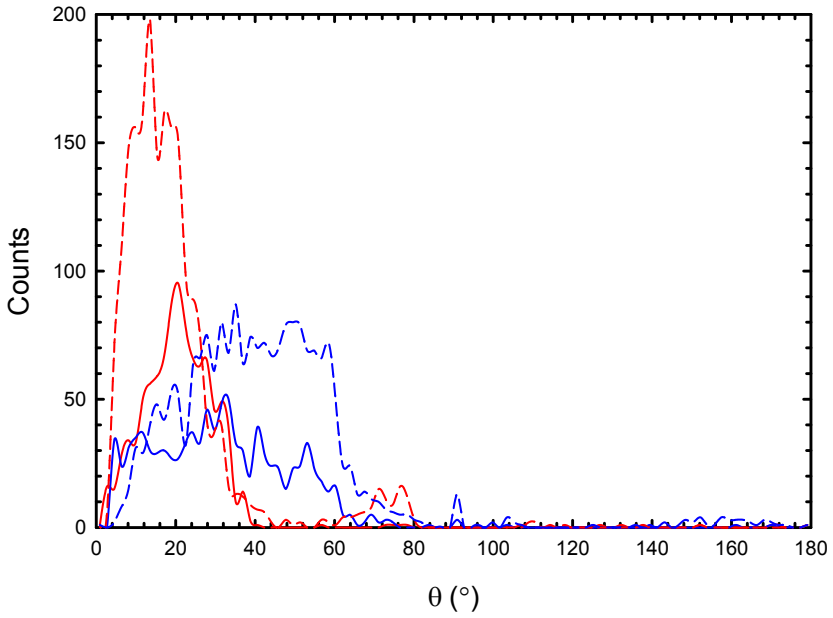

Figure 8.4.3: θ dependence for the positron and electron, with the apparent secondary electron peak removed, — and — are θ_{e^+} and θ_{e^-} respectively for the 2013 data; - - - and - - - are θ_{e^+} and θ_{e^-} respectively for the 2014 data

The angle $\phi_{e^+e^-}$ represents the angle between ϕ_{e^+} and ϕ_{e^-} and the results are shown in figure 8.4.4. The data from 2013 and 2014 has been combined to account for the low count rate, but the trends were confirmed to be identical for each data set before combining. It is apparent that, mostly, the electrons are ejected in a

similar direction to the scattered positrons as indicated by the peaks around 0 and 360°. There is a dip around 180°showing that fewer electrons are ejected in the opposite direction to the scattered positron. The low number of counts means that it is not possible to extract the relationships between positrons scattered at specific angles and the ejected electrons, therefore direct comparison with literature data is difficult. However, data from De Lucio et al. (2010) suggests that for 200 eV positrons impacting argon there should be a dip around 180°as observed here.

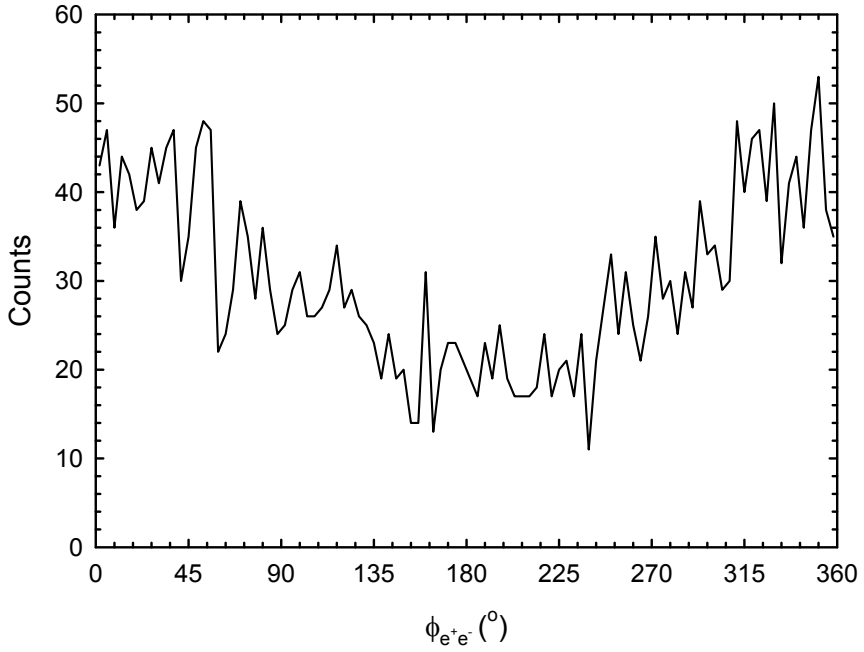

Figure 8.4.4: Electron emission angle, $\phi_{e^+e^-}$, dependence for all E_{e^-} and θ_{e^+}, with the apparent secondary electron peak removed, 2013 and 2014 data combined

In conclusion, the results presented in this chapter are the first from a positron reaction microscope ionisation experiment. They show relationships in-line with expectations based upon theoretical and other experimental data. Generally, positrons are scattered in a forward direction and retain the majority of the initial longitudinal momentum. Electrons are ejected with less longitudinal momentum and at a higher angle relative to the initial beam, but still in the forward direction. Given the current experimental limitations it is not yet possible to ascertain full TDCS for positron-impact ionisation of argon, but the present results are

encouraging. Further study is required, with improvements to the equipment which will allow for more nuanced data analysis (see section 10.2 for more details).

Chapter 9

Conclusion

The goal of this thesis was to experimentally investigate positron interactions with atoms and molecules. In achieving this, the work presented focuses on two different systems, argon and C_{60}, which were studied through the lens of two pieces of experimental apparatus.

The single scattering experiment was used to study positron scattering from argon and C_{60}. Argon has been studied in depth before, using this same experiment (Jones et al., 2011), when high-resolution measurements were made of total scattering and Positronium (Ps) formation cross sections. The experimental study of simple targets such as the noble gases is important as the theoretical handling of these targets is usually achievable. Comparison between high-quality experimental data and theoretical models in regions where experiments are manageable allows for calculations to be improved, meaning that they can be extended to targets that are not so experimentally friendly.

In this thesis, the first absolute elastic differential cross sections (DCS) from 2-50 eV, and total elastic and inelastic cross sections up to 20 eV, are presented. They were compared with calculations from the convergent close-coupling (CCC) method (Fursa and Bray, 2012) and the relativistic optical potential (ROP) method (Chen et al., 2008). Generally, the present DCS results agree more closely with the CCC method than the ROP method at all energies, although above the Ps formation threshold the agreement between the current results and the ROP method improves. The total elastic cross section is again much better modelled by the CCC method below the Ps formation cross section, consistent with the discrepancies observed in the DCS between the small angle scattering predicted by the CCC method in comparison to the ROP method. On the other hand,

the ROP method describes the total inelastic cross section almost perfectly up to 20 eV.

Experimental evidence for the existence of temporary positron binding to atoms and molecules has proven to be an elusive goal over the years, despite many theoretical predictions of their existence. This temporary binding may result in the appearance of resonant features in scattering cross sections. Multiple studies have been conducted over the years, with many finding no trace of resonances in positron-atom scattering

Finally, this thesis is concerned with the development of a positron reaction microscope. Reaction microscopes in their current incarnation evolved from Recoil Ion, and Cold Target Recoil Ion, Momentum Spectroscopy and were developed by Moshammer et al. (1994) (and Moshammer et al. (1996)) and Ullrich et al. (2003). They provide many benefits in the study of scattering events, including:

- 4π acceptance
- high momentum resolution and
- an ability to detect all post-collision particles in coincidence

These features mean that they are able to measure total differential cross sections (TDCS) which provide significantly more information about the dynamics of scattering events, such as ionisation, than single scattering experiments. Reaction microscopes have been used to study scattering due to photon, electron and ion impact (Ullrich et al., 2003), but positron scattering has been largely neglected (with the exception of preliminary results from Holzwarth (2010)).

In this thesis, experimental techniques have been outlined for the operation of a new positron reaction microscope. Analysis techniques have been developed, as shown in chapter 5, and applied to the first experimental results from the apparatus, concerning single ionisation of argon by 190 eV positron impact. While experimental equipment limitations and count rates prevents the measurement of full TDCS at present, the present results show similar results to expectations based upon available theory and experiment. Positrons scattered during an ionisation event tend to keep the majority of the longitudinal momentum, while electrons are ejected with more transverse momentum. Positrons and electrons

are mostly forward scattered (angles $<90°$) and, as indicated by their azimuthal scattering angles, travel in approximately the same direction with relatively few electrons ejected back-to-back with the scattered positron. These results provide initial evidence of the feasibility of these experiments and the techniques developed will, hopefully, allow for more detailed experimental study of the kinematics of positron-induced single ionisation events.

There are many directions for future work with the two experimental apparatus discussed in this thesis, detailed information about this is provided in chapter 10. On the single scattering experiment, this should involve a return to C_{60}, collecting more data to provide better statistical information. Continuation of studies on positron scattering from noble gases could include measurement of absolute DCS for positron-neon scattering as there is currently very little available experimental DCS for neon and no absolute measurements. For the positron reaction microscope, the future involves improvements to the experimental apparatus, methods and analysis to provide more detailed results and extension to other targets.

Publications

The work presented in chapter 6 has been published in Physical Review A:

- R.A. Boadle, T.J. Babij, J.R. Machacek, R.P. McEachran, S.J. Buckman and J.P. Sullivan. (2016). Low-energy elastic and inelastic scattering of positrons from argon. *Physical Review A* 93:022712.

The author has also contributed to additional publications:

- J.R. Machacek, R.A. Boadle, S.J. Buckman and J.P. Sullivan. (2012). Search for quasibound states in the doubly excited region of the helium atom. *Physical Review A* 86:064702.
- P. Palihawadana, R.A. Boadle, L. Chiari, E.K. Anderson, J.R. Machacek, M.J. Brunger, S.J. Buckman and J.P. Sullivan. (2013). Positron scattering from pyrimidine. *Physical Review A* 88:012717.
- E.K. Anderson, R.A. Boadle, J.R. Machacek, L. Chiari, C. Makochekanwa, S.J. Buckman, M.J. Brunger, G. Garcia, F. Blanco, O. Ingolfsson and J.P. Sullivan. (2014). Low energy positron interactions with uracil- total scattering, Positronium formation, and differential elastic scattering cross sections. *The Journal of Chemical Physics* 141(3):034306

Chapter 10

Future Work

This chapter outlines future work to be conducted on the single scattering and positron reaction microscope experiments. The ideas documented include continuation of work presented in this thesis, as well as necessary improvements and changes to the data analysis which would, hopefully, enhance the capabilities of the positron reaction microscope.

10.1 Single Scattering Experiment

10.1.1 C_{60}

The results for positron scattering from C_{60} presented in chapter 7 are incomplete as experimental difficulties restricted data collection times significantly. The target proved to be relatively simple to handle and temperatures of $\sim$400°C were sufficient to produce a viable vapour pressure. Therefore, future work on this target is certainly feasible and should incorporate a thorough investigation of the resonances identified by Gianturco and Lucchese (1999). This should begin with the g_g and h_g resonance at 1.5 eV and the h_g resonance at 3.8 eV produced from the V_{PCP} model, which appears to describe the shape of the total cross section much better than the V_{ECP} model.

Gianturco and Lucchese (1999) calculates DCS around the t_{2u} and g_u at 0.4 eV using the V_{PCP} model and demonstrates significant differences in the shape of the DCS compared to the DCS at 3 eV, where there are no predicted resonances. Given the current experimental setup, it is difficult to investigate the resonances

below 1 eV with much confidence, although it would be possible to measure DCS at the higher resonances. Therefore, if resonances were observed in the total cross sections, DCS at these energies should also be measured. Additional theoretical support would also assist in guiding the experiments. Accurate theoretical treatment of large molecules is very difficult but are possible using some models.

10.1.2 Neon

Neon is a noble gas which, like argon, is relatively simple to model theoretically. In addition, it is easily accessible for experimental measurements with high purity gases available. Over the years, the total cross sections for neon have been studied significantly and good agreement now exists between theory and experiment (Jones et al. (2011)). However, unlike argon, there is very little prior experimental work on DCS, which provide a much more stringent test of theory. At low energies ($\leq$200 eV) relative experimental DCS are available only at 13.6, 20, 50 and 200 eV (Kauppila, W.E.; Kwan, C.K.; Przybyla, D.; Smith, S.J.; Stein (1996)). These DCS cover the angular range between 30 and 135°and are restricted by the physical positioning of the detectors. As with argon, the theoretical DCS are scaled to match the magnitude of the experimental DCS

If the positron beam energy spread is $\sim$60 meV, the single scattering experiment should be able to measure angles of 10° at 13.6 eV, an improvement on the angular acceptance of previous experiments. The first electronic excitation threshold for neon is 16.6 eV, therefore an M ratio of $\sim$3 would give access to DCS up to 50 eV as well as total elastic and total inelastic cross sections. Future work with neon should focus on the measurement of absolute DCS at low energies around the Ps formation threshold.

10.2 Reaction Microscope

10.2.1 Supersonic Gas Jet

The reaction microscope experiments discussed in this thesis used an effusive target gas jet as this provides a larger intersection between gas jet and positron beam, increasing the overall count rate and simplifying these initial experiments.

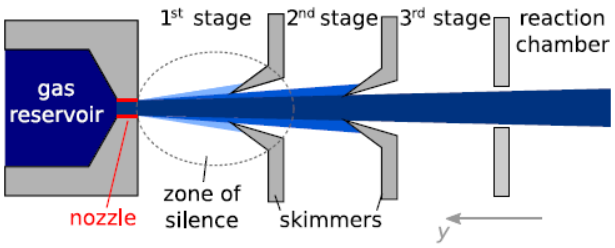

Figure 10.2.1: Supersonic gas jet with two skimmers and a third differential pumping region separating the jet system from the main chamber. Reproduced from Senftleben (2009)

However, the large momentum spread of the target atoms meant that momentum reconstruction was only possible through a fitting routine (see section 5.4.6). This has some significant flaws, including the inability to determine the recoil ion momentum and difficulty in distinguishing between electrons from an ionisation event and secondary electrons appearing at a similar relative time of flight. A better momentum reconstruction method exploits momentum conservation in order to extract the time of flight of the positron, the framework for this is discussed in section 10.2.2. For this to be possible, a supersonic gas jet must be used so that the initial momentum of the target atoms can be reduced.

A supersonic gas jet reduces the temperature of the target gas through adiabatic expansion. The target gas, at temperature T_i and pressure p_i, expands through a nozzle of diameter d into a region with a much lower pressure, p_b. In the nozzle the target gas accelerates through supersonic expansion until the particles' velocity exceeds the local speed of sound. This region is called the 'zone of silence' as the gas cannot sense downstream boundary conditions, thus the final pressure of the gas p_f is independent of p_b. Skimmers in the 'zone of silence' and further downstream allow for collimation of the gas beam and the removal of particles with high transverse momentum (see figure 10.2.1).

The cool target beam produced by a supersonic gas jet has a terminal speed ratio, S_∞, given by

$$S_\infty = \frac{v_{jet}}{v_{therm}} \tag{10.2.1}$$

where v_{jet} is the particle velocity in the gas jet and v_{therm} is the particles' thermal velocity. S_∞ is the velocity ratio long after the expansion and is largely dependent

upon p_i, d and the properties of the gas. The final temperature, $T_{f,\parallel}$, of the gas jet in the experiment's longitudinal, z, direction (perpendicular to the direction of propagation of the gas jet) is given by

$$T_{f,\parallel} = T_i \frac{\gamma}{\gamma - 1} \frac{1}{S_\infty^2} \tag{10.2.2}$$

where γ is the heat capacity ratio, which is 1.670 for Argon at room temperature, but varies with temperature. v_{jet} can be measured using calibration techniques detailed in Senftleben (2009) and used to find the 'effective' γ given by the relationship

$$v_{jet} = \sqrt{\frac{2k}{m} \cdot \frac{\gamma}{\gamma - 1} \cdot T_i} \tag{10.2.3}$$

Depending upon the parameters of the experiment, $T_{f,\parallel}$ can be much smaller than T_i, often a few degrees Kelvin. A final temperature of 2 K would correspond to a momentum spread of 1.27 a.u. for Argon atoms, much less than the ∼14.5 a.u. for the effusive gas jet, and less than the projectile momentum.

10.2.2 Newton-Raphson Method

If the momentum spread of the target atoms can be constrained such that it is close to 0 a.u. the momentum reconstruction may be performed in a more rigorous manner. The current momentum reconstruction analysis can only be reasonably used for triple coincidences where there is only one electron present, if there are multiple electrons it can be difficult to distinguish the ejected electron from the specific ionisation event and the event must be removed from the data set. If the momentum spread of the target atoms is very small the sum of the final state (post-collision) momentum vectors, $\boldsymbol{p}_{sum}$, is equal to the initial momentum of the projectile, $\boldsymbol{p}_{proj} = (0, 0, p_{proj})$ and the momentum conservation equation is given by

$$\boldsymbol{p}_{sum} = \boldsymbol{p}_{e^+} + \boldsymbol{p}_{e^-} + \boldsymbol{p}_{ion} \equiv \boldsymbol{p}_{proj} \tag{10.2.4}$$

where $\boldsymbol{p}_{e^+}, \boldsymbol{p}_{e^-}, \boldsymbol{p}_{ion}$ are the momenta vectors for the positron, electron and ion respectively. Considering only the longitudinal momentum, equation 10.2.4 can be rewritten as

$$p_{sum,z} = p_{e^+,z}(t_{e^+}) + p_{e^-,z}(t_{e^+} + t_{e^+e^-}) + p_{ion,z}(t_{e^+} + t_{e^+ion}) \equiv p_{proj,z} \tag{10.2.5}$$

where t_{e^+} is the time of flight of the positron and $t_{e^+e^-}$, t_{e^+ion} are the relative times of flight for the electron and ion respectively. Thus, equation 10.2.5 is a function of one unknown, t_{e^+}. The Newton-Raphson method can be used to find the root of

$$f(t_{e^+}) = p_{proj,z} - p_{sum,z}(t_{e^+}) \tag{10.2.6}$$

implemented as

$$t_{e^+}^{n+1} = t_{e^+}^{n} - \frac{f(t_{e^+}^{n})}{f'(t_{e^+}^{n})} \tag{10.2.7}$$

In order to solve these equations, expressions for $p_{e^+,z}$, $p_{e^-,z}$ and $p_{ion,z}$ must be determined. The relationship between particle time of flight and longitudinal momentum is given by equation 5.1.9, but cannot be rearranged to give $p_z(t)$. Therefore, some approximations must be made. For the ion, if we assume that the amount of momentum gained from the electric field is much greater than the initial longitudinal momentum, it is reasonable to approximate equation 5.1.9 with a taylor expansion near the point $p_0 = 0$. The Taylor expansion for $p_{ion,z}$ is given by

$$t_{ion}(p_{ion,z}) = t_{ion}(p_{ion,z} = 0) + (p_{ion,z} - 0)t'_{ion}(p_{ion,z} = 0) + \cdots \tag{10.2.8}$$

which, using equation 5.1.9, and rearranging for $p_{ion,z}$ can be written as

$$\begin{aligned} p_{ion,z}(t_{ion}) = &\frac{qU_A}{L_A}\left(m \cdot \left(\frac{2L_A}{2qmU_A} + \frac{L_B}{2qmU_A}\right.\right. \\ &\left.\left. + \frac{2L_C}{\sqrt{2qmU_A + 2qmU_{MCP}} + \sqrt{2qmU_A}}\right) - (t_{e^+} + t_{e^+ion})\right) \end{aligned} \tag{10.2.9}$$

where t_{ion} is the time of flight of the ion. The differential of $p_{ion,z}$ is

$$\frac{dp_{ion,z}}{dt_{e^+}} = -\frac{qU_A}{L_A} \tag{10.2.10}$$

The situation for the positrons and electrons is more complex as it is no longer valid to assume that they gain little momentum from the extraction field compared to their initial momentum after the ionisation event. In order to find expressions for $p_{e^+,z}$, $p_{e^-,z}$ and their respective differentials with respect to t_{e^+}, equation 5.1.9 can be simplified, assuming that the contribution due to the accelerated across L_A is small, to give

$$t = \frac{2mL_A}{\sqrt{p_z^2 + 2qmU_A} \pm p_z} + \frac{mL_BC}{\sqrt{p_z^2 + 2qmU_A}} \tag{10.2.11}$$

where $L_BC = L_B + L_C$. In the reaction microscope setup here, L_BC/L_A =1.92, therefore equation 10.2.11 can be written as

$$t = mL_A \cdot \left(\frac{2}{\sqrt{p_z^2 + 2qmU_A} \pm p_z} + \frac{1.92}{\sqrt{p_z^2 + 2qmU_A}} \right) \tag{10.2.12}$$

Substituting $X_e^2 = p_z^2/2mqU_A$ and $T_e = \sqrt{qU_At^2/2mL_A^2}$ into equation 10.2.12 gives

$$T_e = \frac{1}{\sqrt{X_e^2 + 1} + X_e} + \frac{0.96}{\sqrt{X_e^2 + 1}} \tag{10.2.13}$$

Plotting this equation for a reasonable range of X_e, a fit can be found with the form

$$X_e = A_e + \frac{B_e}{T_e} + C_eT_e + D_e \sin(T_e) \tag{10.2.14}$$

where A_e, B_e, C_e, D_e are constants to be determined from the graph. As $p_z = X_e\sqrt{2mqU_A}$, the momentum is given by

$$p_z = 2m\kappa \left(A_e + \frac{L_AB_e}{\kappa t} + \frac{C_e\kappa t}{L_A} + D_e \sin(\frac{\kappa t}{L_A}) \right) \tag{10.2.15}$$

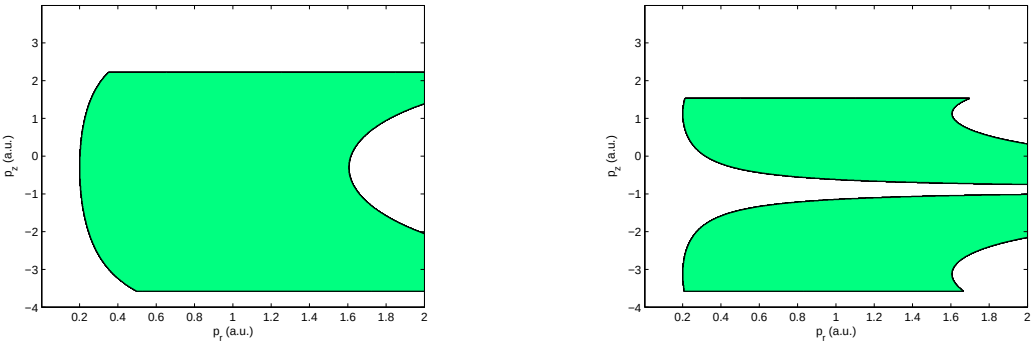

(a) 6.262V/cm **(b)** 3V/cm

Figure 10.2.2: Simulated electron acceptance for 6.262V/cm and 3V/cm extraction field

where $\kappa = \sqrt{qU_A/2m}$ and $t = t_{e^+}$ for positrons, $t = t_{e^+} + t_{e^+e^-}$ for electrons. The differential is

$$\frac{dp_z}{dt} = 2m\kappa \left(-\frac{L_A B_e}{\kappa t^2} + \frac{C_e \kappa}{L_A} + \frac{\kappa D_e}{L_A} \cos(\frac{\kappa t}{L_A}) \right) \tag{10.2.16}$$

Therefore, equations 10.2.8, 10.2.10, 10.2.15 and 10.2.16 can be substituted into 10.2.6 and solved to give t_{e^+} using the Newton-Raphson method. The solution to this will be unique and can be used to exclude spurious particle hits, unassociated with ionisation events, as the momentum for these events will not be conserved.

10.2.3 Additional Measurements for Single Ionisation of Argon

In order to cover the full momentum space, experiments should be conducted with multiple extraction fields and combined. The momentum acceptance for positrons, electrons and ions was outlined in section 5.3 and figure 10.2.2 demonstrates the effect on the electron acceptance of changing the extraction field. For example, figure 10.2.2a shows that when the longitudinal momentum of the electron is close to -3.57 a.u., small transverse momenta cannot be detected, whereas in figure 10.2.2b this combination of longitudinal and transverse momenta are detectable. However, the higher extraction field of 6.262 V/cm can detect particles with longitudinal momenta ∼-1 a.u. which is not possible at the lower extraction field.

Reducing the extraction field can also provide a better momentum resolution, although, it can complicate detection of the ion. In this example, reducing the extraction field to 3 V/cm increases the ion time of flight to >32 μs. The maximum relative time of flight between the positron and ion that a single 3377 TDC can detect is 32 μs, therefore at an extraction field of 3 V/cm a second TDC would need to be included in the detection electronics.

10.2.4 Further Targets

The reaction microscope can be used to investigate a large range of targets. Single ionisation of helium by positron impact would be a natural progression from the measurements presented here as helium is a simpler system for theoretical treatment and would provide a better system for experimental-theoretical comparison. As helium is significantly lighter than argon, the ion may be extracted using low extraction fields- for example, the time of flight for a singly ionised helium atom in an extraction field of 0.5 V/cm is only 25 μs, easily achievable with a single TDC setup. However, helium has a single ionisation cross section almost ten times smaller than for positron-argon single ionisation (Knudsen et al. (1990)). Therefore, in order to collect an equivalent number of counts the experiment would need to be run for much longer. Improving the intensity of the incident positron beam would significantly help these measurements.

Another system which could be relatively easily investigated, is double ionisation of argon by positron impact, Ar^{2+}. The current experiment has detected many Ar^{2+} events. However, as a full measurement for these events requires detection of two electrons, unless a supersonic gas jet is used it is not possible to reconstruct the momenta using the method detailed in section 10.2.2.

Bibliography

Aharonov, Y., Avignone, F., Brodzinski, R., Collar, J., García, E., Miley, H., Morales, a., Morales, J., Nussinov, S., Ortiz de Solórzano, a., Puimedón, J., Reeves, J., Sáenz, C., Salinas, a., Sarsa, M., and Villar, J. (1995). New experimental limits for the electron stability. *Physics Letters B*, 353(2-3):168–172.

Ahmadi, M., Alves, B. X. R., Baker, C. J., Bertsche, W., Butler, E., Capra, A., Carruth, C., Cesar, C. L., Charlton, M., Cohen, S., Collister, R., Eriksson, S., Evans, A., Evetts, N., Fajans, J., Friesen, T., Fujiwara, M. C., Gill, D. R., Gutierrez, A., Hangst, J. S., Hardy, W. N., Hayden, M. E., Isaac, C. A., Ishida, A., Johnson, M. A., Jones, S. A., Jonsell, S., Kurchaninov, L., Madsen, N., Mathers, M., Maxwell, D., McKenna, J. T. K., Menary, S., Michan, J. M., Momose, T., Munich, J. J., Nolan, P., Olchanski, K., Olin, A., Pusa, P., Rasmussen, C. Ø., Robicheaux, F., Sacramento, R. L., Sameed, M., Sarid, E., Silveira, D. M., Stracka, S., Stutter, G., So, C., Tharp, T. D., Thompson, J. E., Thompson, R. I., van der Werf, D. P., and Wurtele, J. S. (2017). Observation of the 1S - 2S transition in trapped antihydrogen. *Nature*, 541:506–510.

Allen, R. A., Burcham, W. E., Chackett, K. F., Munday, G. L., and Reasbeck, P. (1955). Electron Capture in the Decay of Sodium 22. *Proceedings of the Physical Society. Section A*, 68(8):681–685.

Anderson, C. D. (1933). The positive electron. *Physical Review*, 43(6):491–494.

Anderson, E. K., Boadle, R. A., Machacek, J. R., Chiari, L., Makochekanwa, C., Buckman, S. J., Brunger, M. J., Garcia, G., Blanco, F., Ingolfsson, O., and Sullivan, J. P. (2014). Low energy positron interactions with uracil–total scattering, positronium formation, and differential elastic scattering cross sections. *The Journal of chemical physics*, 141(3):034306.

Andresen, G. B., Ashkezari, M. D., Baquero-Ruiz, M., Bertsche, W., Bowe, P. D., Butler, E., Cesar, C. L., Charlton, M., Deller, A., Eriksson, S., Fajans, J., Friesen, T., Fujiwara, M. C., Gill, D. R., Gutierrez, A., Hangst, J. S., Hardy, W. N., Hayano, R. S., Hayden, M. E., Humphries, A. J., Hydomako, R., Jonsell, S., Kemp, S. L., Kurchaninov, L., Madsen, N., Menary, S., Nolan, P., Olchanski, K., Olin, A., Pusa, P., Rasmussen, C. Ø., Robicheaux, F., Sarid, E., Silveira, D. M., So, C., Storey, J. W., Thompson, R. I., van der Werf, D. P., Wurtele, J. S., and Yamazaki, Y. (2011). Confinement of antihydrogen for 1,000 seconds. *Nature Physics*, 7(7):558–564.

Barnes, L. D., Gilbert, S. J., and Surko, C. M. (2003). Energy-resolved positron annihilation for molecules. *Physical Review A*, 67(3):032706.

Bartschat, K., McEachran, R. P., and Stauffer, A. D. (1988). Optical potential approach to electron and positron scattering from noble gases. I. Argon. *Journal of Physics B: Atomic, Molecular and Optical Physics*, 21(15):2789–2800.

Beer, A. (1852). Bestimmung der Absorption des rothen Lichts in farbigen Flussigkeiten. *Annalen der Physik und Chimie*, 86:78–88.

Bell, R. E. and Graham, R. L. (1953). Time distribution of positron annihilation in liquids and solids. *Physical Review*, 90(4):644–654.

Berakdar, J., Briggs, J. S., and Klar, H. (1993). Scaling behaviour of the triply differential cross section for the ionization of atomic hydrogen. *Journal of Physics B: Atomic, Molecular and Optical Physics*, 26(2):285–296.

Berko, S. and Plaskett, J. S. (1958). Correlation of Annihilation Radiation in Oriented Single Metal Crystals. *Physical Review*, 112:1877.

Blackett, P. and Occhialini, G. (1933). Some Photographs of the Tracks of Penetrating Radiation. *Proceedings of the Royal Society of London A*, 139(839):699–720.

Boadle, R. A., Babij, T. J., Machacek, J. R., McEachran, R. P., Sullivan, J. P., and Buckman, S. J. (2016). Low-energy elastic and inelastic scattering of positrons from argon. *Physical Review A*, 93(022712).

Brauner, M. and Briggs, J. S. (1993). Structure in differential cross sections for positron and electron impact ionization of hydrogen. *Journal of Physics B: Atomic, Molecular and Optical Physics*, 26(15):2451–2461.

Buckman, S. J. and Clark, C. W. (1994). Atomic negative-ion resonances. *Reviews of Modern Physics*, 66(2):539–655.

Campeanu, R. I., McEachran, R. P., and Stauffer, a. D. (1996). Positron impact ionization of He, Ne, and Ar. *Canadian Journal of Physics*, 74(7-8):544–547.

Canter, K. F., Brandes, G. R., Horsky, T. N., Lippel, P. H., and Mills, A. P. (1987). -. In *Atomic Physics with Positrons*, page 153. Plenum, New York.

Canter, K. F., Coleman, P. G., Griffith, T. C., and Heyland, G. R. (1972). Measurement of total cross sections for low energy positron-helium collisions. (Positron backscattering from metal surface). *Journal of Physics B: Atomic and Molecular Physics*, 5(8):L167–L169.

Charlton, M. (1985). Experimental studies of positrons scattering in gases. *Reports on Progress in Physics*, 48(6):737–793.

Charlton, M. and Humberston, J. W. (2000). *Positron Physics*. Cambridge University Press, Cambridge.

Chen, S., McEachran, R. P., and Stauffer, A. D. (2008). Ab initio optical potentials for elastic electron and positron scattering from the heavy noble gases. *Journal of Physics B: Atomic, Molecular and Optical Physics*, 41(2).

Cherry, W. H. (1958). *Secondary Electron Emission Produced from Surfaces by Positron Bombardment.* PhD thesis, Princeton University.

Chiari, L., Anderson, E. K., Tattersall, W., Machacek, J. R., Palihawadana, P., Makochekanwa, C., Sullivan, J. P., García, G., Blanco, F., McEachran, R. P., Brunger, M. J., and Buckman, S. J. (2013). Total, elastic, and inelastic cross sections for positron and electron collisions with tetrahydrofuran. *Journal of Chemical Physics*, 138(7).

Coleman, P. G. and McNutt, J. D. (1979). Measurement of differential cross sections for the elastic scattering of positrons by argon atoms. *Physical Review Letters*, 42(17):1130–1133.

Coleman, P. G., McNutt, J. D., Diana, L., and Hutton, J. (1980). Measurement of total cross sections for the scattering of positrons by argon and xenon atoms. *Physical Review A*, 22(5):2290–2292.

Costello, D. G., Groce, D. E., Herring, D. F., and McGowan, J. W. (1972a). (e + , He) Total Scattering. *Canadian Journal of Physics*, 50(1):23–33.

Costello, D. G., Groce, D. E., Herring, D. F., and McGowan, J. W. (1972b). Evidence for the Negative Work Function Associated with Positrons in Gold. *Physical Review B*, 5(4):1433–1436.

Danielson, J. R. and Dubin, D. H. E. (2015). Plasma and trap-based techniques for science with positrons. *Reviews of Modern Physics*, 87(January-March):247–306.

De Lucio, O. G., Otranto, S., Olson, R. E., and Dubois, R. D. (2010). Triply differential single ionization of argon: Charge effects for positron and electron impact. *Physical Review Letters*, 104(16):1–4.

de Vries, J., Steger, H., Kamke, B., Menzel, C., Weisser, W., Kamke, W., and Hertel, I. V. (1992). Single-photon ionization of C60- and C70-fullerene with synchrotron radiation: determination of the ionization potential of C60. *Chemical Physics Letters*, 188(3-4):159–162.

DeBenedetti, S., Cowan, C. E., and Konneker, W. R. (1949). Angular Distribution of Annihilation Radiation. *Physical Review*, 76(3):440.

Dehmelt, H. G., Schwinberg, P. B., and Van Dyck, R. S. J. (1978). Proposed scheme to catch positrons in a Penning trap. *International Journal of Mass Spectrometry and Ion Physics*, 26(1):107–108.

Dine, M. and Kusenko, A. (2004). Origin of the matter-antimatter asymmetry. *Reviews of Modern Physics*, 76(1):1–30.

Dirac, P. (1928). The quantum theory of the electron. *Proceedings of the Royal Society of London A: Mathematical, Physical and Engineering Sciences*, 117(778):610–624.

Dirac, P. (1931). Quantised Singularities in the Electromagnetic Field. *Proceedings of the Royal Society of London A: Mathematical, Physical and Engineering Sciences*, 133(821):60–72.

Dorn, A., Moshammer, R., Schröter, C. D., Zouros, T. J. M., Schmitt, W., Kollmus, H., Mann, R., and Ullrich, J. (1999). Double Ionization of Helium by Fast Electron Impact. *Physical Review Letters*, 82(12):2496–2499.

Dürr, M. (2006). *Electron Induced Break-up of Helium: Benchmark Experiments on a Dynamical Four-Body Coulomb System*. PhD thesis, University of Heidelberg.

Dzuba, V. A., Flambaum, V. V., and Gribakin, G. F. (2010). Detecting Positron-Atom Bound States through Resonant Annihilation. *Physical Review Letters*, 105(20):203401.

Ehrhardt, H., Schulz, M., Tekaat, T., and Willmann, K. (1969). Ionization of Helium: Angular Correlation of the Scattered and Ejected Electrons. *Physical review letters*, 22(3):89.

Floeder, K., Honer, P., Raith, W., Schwab, A., Sinapius, G., and Spicher, G. (1988). Differential Elastic Scattering of Positrons from Argon Atoms at Low Energies. *Physical Review Letters*, 60(23):2363–2366.

Fromme, D., Kruse, G., Raith, W., and Sinapius, G. (1986). Partial-cross-section measurements for ionization of helium by positron impact. *Physical Review Letters*, 57(24):3031.

Fursa, D. V. and Bray, I. (2012). Convergent close-coupling method for positron scattering from noble gases. *New Journal of Physics*, 14.

Gianturco, F. and Lucchese, R. (1999). Computational investigation of positron scattering from C_{60}. *Physical Review A*, 60(6):4567–4576.

Gianturco, F. A. and Mukherjee, T. (1997). Dynamical coupling effects in the vibrational excitation of H2 and N2 colliding with positrons. *Physical Review A*, 55(2):1044–1055.

Gilbert, S., Greaves, R., and Surko, C. (1999). Positron Scattering from Atoms and Molecules at Low Energies. *Physical Review Letters*, 82(25):5032–5035.

Gilbert, S., Sullivan, J., Greaves, R., and Surko, C. (2000). Low-energy positron scattering from atoms and molecules using positron accumulation techniques.

Nuclear Instruments and Methods in Physics Research Section B: Beam Interactions with Materials and Atoms, 171(1-2):81–95.

Greaves, R. G. and Moxom, J. M. (2008). Compression of trapped positrons in a single particle regime by a rotating electric field. *Physics of Plasmas*, 15(7):072304.

Gribakin, G. F., Young, J. A., and Surko, C. M. (2010). Positron-molecule interactions: Resonant attachment, annihilation, and bound states. *Reviews of Modern Physics*, 82(3):2557.

Hedberg, K., Hedberg, L., Bethune, D. S., Brown, C. a., Dorn, H. C., Johnson, R. D., and DE Vries, M. (1991). Bond lengths in free molecules of buckminsterfullerene, C60, from gas-phase electron diffraction. *Science (New York, N.Y.)*, 254(5030):410–412.

Hervieux, P. A., Chakraborty, A. R., and Chakraborty, H. S. (2017). Ubiquitous diffraction resonances in positronium formation from fullerenes. *Physical Review A*, 95(2):1–6.

Holzwarth, M. (2010). *Kinematically Complete Study of Positron Impact Ionisation of Helium*. PhD thesis, University of Heidelberg.

Humberston, J. W. (1973). The scattering of low energy positrons by helium. *Journal of Physics B: Atomic and Molecular Physics*, 6(11):L305.

Hyder, G. M. A., Dababneh, M., Hsieh, Y.-F., Kauppila, W., Kwan, C., Mahdavi-Hezaveh, M., and Stein, T. (1986). Positron Differential Elastic-Scattering Cross-Section Measurements for Argon. *Physical review letters*, 57(18):1–4.

Idziaszek, Z. and Karwasz, G. (2006). Applicability of modified effective-range theory to positron-atom and positron-molecule scattering. *Physical Review A*, 73(6:064701).

Ingle, J. D. J. and Crouch, S. R. (1988). *Spectrochemical Analysis*. Prentice Hall, New Jersey.

Jacobsen, F. M., Frandsen, N. P., Knudsen, H., Mikkelsen, U., and Schrader, D. M. (1995). Single ionization of He, Ne and Ar by positron impact. *Journal of Physics B: Atomic and Molecular Physics*, 28:4691–4695.

Jagutzki, O., Spielberger, L., Dörner, R., Nüttgens, S., Mergel, V., Schmidt-Böcking, H., Ullrich, J., and Buck, U. (1996). Recoil-ion momentum distribution for He(e,2e)He+ and He(e,3e)He++ reactions. *Z Phys D - Atoms, Molecules and Clusters*, 36(5).

Jones, A. (2010). *Low Energy Positron Interactions with the Rare Gases*. PhD thesis, Australian National University.

Jones, A. C. L., Caradonna, P., Makochekanwa, C., Slaughter, D. S., McEachran, R. P., Machacek, J. R., Sullivan, J. P., and Buckman, S. J. (2010). Observation of Threshold Effects in Positron Scattering from the Noble Gases. *Physical Review Letters*, 105(7):073201.

Jones, A. C. L., Makochekanwa, C., Caradonna, P., Slaughter, D. S., Machacek, J. R., McEachran, R. P., Sullivan, J. P., Buckman, S. J., Stauffer, A. D., Bray, I., and Fursa, D. V. (2011). Positron scattering from neon and argon. *Physical Review A*, 83(3):032701.

Kadyrov, A. S. and Bray, I. (2002). Two-center convergent close-coupling approach to positron-hydrogen collisions. *Physical Review A*, 66(1):012710.

Kara, V., Paludan, K., Moxom, J., Ashley, P., and Laricchia, G. (1997). Single and double ionization of neon, krypton and xenon by positron impact. *Journal of Physics B: Atomic, Molecular and Optical Physics*, 30:3933–3949.

Kauppila, W.E.; Kwan, C.K.; Przybyla, D.; Smith, S.J.; Stein, T. (1996). Positron-inert-gas-atom elastic DCS measurements. *Can. J. Phys.*, 74:474–482.

Kernoghan, A. A., Robinson, D. J. R., McAlinden, M. T., and Walters, H. R. J. (1996). Positron scattering by atomic hydrogen. *Journal of Physics B: Atomic, Molecular and Optical Physics*, 29(10):2089–2102.

Kheifets, A. S., Bray, I., Lahmam-Bennani, A., Duguet, A., and Taouil, I. (1999). A comparative experimental and theoretical investigation of the electron-impact double ionization of He in the keV regime. *Journal of Physics B: Atomic, Molecular and Optical Physics*, 32(21):5047–5065.

Knudsen, H., Brun-Nielsen, L., Charlton, M., and Poulsen, M. R. (1990). Single Ionization of H2, He, Ne and Ar by positron impact. *Journal of Physics B: Atomic, Molecular and Optical Physics*, 23:3955–3976.

Knudsen, M. (1910). Thermischer Molekulardruck der Gase in Röhren. *Annalen der Physik*, 338(16):1435–1448.

Kwan, C. K., Kauppila, W. E., Lukaszew, R. A., Parikh, S. P., Stein, T. S., Wan, Y. J., and Dababneh, M. S. (1991). Total cross-section measurements for positrons and electrons scattered by sodium and potassium atoms. *Physical Review A*, 44(3):1620–1635.

Lahmam-Bennani, A., Duguet, A., Dal Capello, C., Nebdi, H., and Piraux, B. (2003). Effect of non-first-order effected in the (e, 3e) double ionization of helium. *Journal of Physics B*, 67:010701.

Lambert, J. H. (1760). *Photometria sive de mensura et gradibus luminis, colorum et umbrae*. Eberhardt Klett, Augsburg, Germany.

Lang, L. G. and Hien, N. C. (1958). Electron Momentum Distributions in Single-Crystal Cd. *Physical Review*, 110:1062.

Lapington, J. and Edgar, M. (1989). The Size and Spatial Distribution of Microchannel Plate Output Electron Clouds. *SPIE*, 1159:565–575.

Liang, S. C. (1953). On the Calculation of Thermal Transpiration. *The Journal of Physical Chemistry*, 57(9):910–911.

Lynn, K. G., MacDonald, J. R., Boie, R. A., Feldman, L. C., Gabbe, J. D., Robbins, M. F., Bonderup, E., and Golovchenko, J. (1977). Positron-annihilation momentum profiles in aluminium: Core contribution and the independent particle model. *Physical review letters*, 38(5):241–244.

Machacek, J. R., Anderson, E. K., Makochekanwa, C., Buckman, S. J., and Sullivan, J. P. (2013). Positron scattering from molecular hydrogen. *Physical Review A*, 88(4):042715.

Machacek, J. R., Boadle, R., Buckman, S. J., and Sullivan, J. P. (2012). Search for positron quasibound states in the doubly excited region of the helium atom. *Physical Review A*, 86(6):064702.

Malmberg, J. H. and Driscoll, C. F. (1980). Long-Time Containment of a Pure Electron Plasma. *Physical review letters*, 44(10):654–657.

Manuel, A. A., Ambigapathy, R., Hautojarvi, P., Saarinen, K., and Corbel, C. (1995). Study of defects in gas by 2D-ACAR positron annihilation. *Journal of Physics IV France*, 5:73–80.

Marler, J. P., Sullivan, J. P., and Surko, C. M. (2005). Ionization and positronium formation in noble gases. *Physical Review A - Atomic, Molecular, and Optical Physics*, 71(2):1–10.

Marler, J. P. and Surko, C. M. (2005a). Positron-impact ionization, positronium formation, and electronic excitation cross sections for diatomic molecules. *Physical Review A - Atomic, Molecular, and Optical Physics*, 72(6):1–10.

Marler, J. P. and Surko, C. M. (2005b). Systematic comparison of positron- and electron-impact excitation of the v3 vibrational mode of CF4. *Physical Review A - Atomic, Molecular, and Optical Physics*, 72(6):1–6.

Matejcik, S., Mark, T. D., Spanel, P., Smith, D., Jaffke, T., and Illenberger, E. (1995). Formation and decay of C-60 following free electron capture by C60. *The Journal of Chemical Physics*, 102(6):2516.

McEachran, R. P. and Stauffer, A. D. (2013). Positronium formation in the noble gases. *Journal of Physics B: Atomic, Molecular and Optical Physics*, 46(7):075203.

Mehra, J. and Rechenberg, H. (2001). *The Completion of Quantum Mechanics 1926 - 1941. The Historical Development of Quantum Theory.* Springer, New York.

Mills, A. and Gullikson, E. (1986). Solid neon moderator for producing slow positrons. *Applied Physics Letters*, 49:1121–1123.

Mills, A. P. (1981). Observation of the Positronium Negative Ion. *Physical Review Letters*, 46(11):717–720.

Mitroy, J., Bromley, M. W. J., and Ryzhikh, G. G. (2002). Positron and positronium binding to atoms. *Journal of Physics B: Atomic, Molecular and Optical Physics*, 35:81–116.

Mondal, N. N., Hamatsu, R., Hirose, T., Iijima, H., Irako, M., Kumita, T., Igura, Y., and Omori, T. (1999). Construction of a time-of-flight measurement system to study low energy positronium production. *Applied Surface Science*, 149(1-4):269–275.

Moshammer, R., Ullrich, J., Schmidt, W., Jardin, P., Olson, R., Mann, R., Dorner, R., Mergel, V., Buck, U., and Schmidt-Bocking, H. (1994). Low-energy electrons and their dynamical correlation with recoil ions for single ionization of helium by fast, heavy-ion impact. *Physical review letters*, 73(25):3372–3374.

Moshammer, R., Unverzagt, M., Schmitt, W., Ullrich, J., and Schmidt-Böcking, H. (1996). A 4π recoil-ion electron momentum analyzer: a high-resolution microscope for the investigation of the dynamics of atomic, molecular and nuclear reactions. *Nuclear Instruments and Methods in Physics Research Section B: Beam Interactions with Materials and Atoms*, 108(4):425–445.

Moxom, J., Ashley, P., and Laricchia, G. (1996). Single ionization by positron impact. *Canadian Journal of Physics*, 74:367–372.

Murphy, T. and Surko, C. (1992). Positron trapping in an electrostatic well by inelastic collisions with nitrogen molecules. *Physical Review A*, 46:5696–5705.

Natisin, M. R., Danielson, J. R., Gribakin, G. F., Swann, A. R., and Surko, C. M. (2017). Vibrational Feshbach Resonances Mediated by Nondipole Positron-Molecule Interactions. *Physical Review Letters*.

NIST (2018). National Institute of Standards and Technology Reference Database.

Palihawadana, P., Boadle, R., Chiari, L., Anderson, E. K., Machacek, J. R., Brunger, M. J., Buckman, S. J., and Sullivan, J. P. (2013). Positron scattering from pyrimidine. *Physical Review A - Atomic, Molecular, and Optical Physics*, 88(1):1–7.

Pederson, M. R. and Quong, A. A. (1992). Polarizabilities, charge states, and vibrational modes of isolated fullerene molecules. *Physical Review B*, 46(20):13584–13591.

Petkov, M. P., Weber, M. H., Lynn, K. G., and Rodbell, K. P. (2001). Porosity characterisation by beam-based three-photon positron annihilation spectroscopy. *Applied Physics Letters*, 79(23):3884–3886.

Piacente, V., Gigli, G., Scardala, P., Giustini, A., and Ferro, D. (1995). Vapor Pressure of C60 Buckminsterfullerene. *Journal of Physical Chemistry*, 99(38):14052–14057.

Popović, A., Dražič, G., and Marsel, J. (1994). Mass spectrometric investigations of fullerenes. I. Vapour pressure over the C60/C70 binary system. *Rapid Communications in Mass Spectrometry*, 8(12):985–990.

Ramsauer, C. (1921). Über den Wirkungsquerschnitt der Gasmoleküle gegenüber langsamen Elektronen. *Annalen der Physik*, 369(6):513–540.

Rescigno, T. N., Baertschy, M., Isaacs, W. A., and McCurdy, C. W. (1999). Collisional Breakup in a Quantum System of Three Charged Particles. *Science*, 286(5449).

Schulz, M., Moshammer, R., Fischer, D., Kollmus, H., Madison, D. H., Jones, S., and Ullrich, J. (2003). Three-dimensional imaging of atomic four-body processes. *Nature (London)*, 422(48).

Scuseria, G. E. (1991). Ab initio theoretical predictions of the equilibrium geometries of C60, C60H60 and C60F60. *Chemical Physics Letters*, 176(5):423–427.

Senftleben, A. (2009). *Kinematically complete study on electron impact ionisation of aligned hydrogen molecules*. PhD thesis, University of Heidelberg.

Sharma, S. and Srivastava, M. K. (1988). Triple-differential cross sections for the electron- and positron-impact ionization of helium in an improved second Born approximation. *Physical Review*, 38(2):1083–1086.

Shimizu, S., Mukoyama, T., and Nakayama, Y. (1968). Radiationless Annihilation of Positrons in Lead. *Physical Review*, 173(2):405–416.

Smith, S. J., Hyder, G. M. A., Kauppila, W. E., Kwan, C. K., and Stein, T. S. (1990). Evidence for Absorption Effects in Positron Elastic Scattering by Argon. *Physical Review Letters*, 64(11):1227–1230.

Stump, R. and Talley, H. E. (1954). Lifetimes of positrons in superconducting lead and tin. *Physical Review*, 96:904–907.

Sullivan, J. P., Gilbert, S., Marler, J., Greaves, R., Buckman, S., and Surko, C. (2002). Positron scattering from atoms and molecules using a magnetized beam. *Physical Review A*, 66:042708.

Sullivan, J. P., Gilbert, S. J., Buckman, S. J., and Surko, C. M. (2001a). Search for resonances in the scattering of low-energy positrons from atoms and molecules. *Journal of Physics B: Atomic, Molecular and Optical Physics*, 34:L467–L474.

Sullivan, J. P., Jones, A., Caradonna, P., Makochekanwa, C., and Buckman, S. J. (2008). A positron trap and beam apparatus for atomic and molecular scattering experiments. *The Review of Scientific Instruments*, 79(11):113105.

Sullivan, J. P., Makochekanwa, C., Jones, a., Caradonna, P., Slaughter, D. S., Machacek, J., McEachran, R. P., Mueller, D. W., and Buckman, S. J. (2011). Forward angle scattering effects in the measurement of total cross sections for positron scattering. *Journal of Physics B: Atomic, Molecular and Optical Physics*, 44(3):035201.

Sullivan, J. P., Marler, J. P., Gilbert, S. J., Buckman, S. J., and Surko, C. M. (2001b). Excitation of electronic states of Ar, H(2), and N(2) by positron impact. *Physical Review Letters*, 87(7):073201.

Surdutovich, E., Setzler, G., Kauppila, W. E., Rehse, S. J., and Stein, T. S. (2008). Measurements of total cross sections for positron scattering by uracil molecules. *Physical Review A*, 77(5):054701.

Surko, C. M., Leventhal, M., and Passner, A. (1989). Positron Plasma in the Laboratory. *Physical review letters*, 62(8):901–904.

Takaishi, T. and Sensui, Y. (1963). Thermal Transpiration Effect of Hydrogen, Rare Gases and Methane. *Transactions of the Faraday Society*, 59:2898.

Taouil, I., Lahmam-Bennani, A., Duguet, A., and Avaldi, L. (1998). Fully Determined (e, 3e) Experiments for the Double Ionization of Helium. *Physical review letters*, 81:4600.

Teachout, R. R. and Pack, R. T. (1971). The static dipole polarizabilities of all the neutral atoms in their ground states. *Atomic Data and Nuclear Data Tables*, 3:195–214.

Townsend, M. A. and Bailey, M. A. (1921). The motion of electrons in gases. *The London, Edinburgh, and Dublin Philosophical Magazine and Journal of Science*, 42(252):873–891.

Ullrich, J., Moshammer, R., Dorn, A., Dorner, R., Schmidt, L. H., and Schmidt-B cking, H. (2003). Recoil-ion and electron momentum spectroscopy: reaction-microscopes. *Reports on Progress in Physics*, 66(9):1463–1545.

Utamuratov, R., Kadyrov, A. S., Fursa, D. V., and Bray, I. (2010). A two-centre convergent close-coupling approach to positronâĂŞhelium collisions. *Journal of Physics B: Atomic, Molecular and Optical Physics*, 43(3):031001.

Wigner, E. (1948). On the Behaviour of Cross Sections Near Thresholds. *Physical Review*, 73(9):1002–1009.

Wolfenstein, L. and Ravenhall, D. G. (1952). Some consequences of invariance under charge conjugation. *Physical Review*, 88(2):279–282.

Yang, C. (1950). Selection Rules for the Dematerialization of a Particle into Two Photons. *Physical Review*, 77(2):242–245.